TECHNISCHE UNIVERSITÄT WIEN
Vienna | Austria

ILSB

Vienna University of Technology

DIPLOMA THESIS

Structural and Mechanical Evaluation of Cortical Bone from Bovine and Equine Femora

carried out for the purpose of obtaining the degree of Dipl.-Ing submitted at TU Wien, Faculty of Mechanical and Industrial Engineering, by

Amirreza *Heshmat*
Student.Nr: 1225217

Under the supervision of:
Univ.Prof. Dipl.-Ing. Dr.sc.nat.Philipp J. Thurner
Dipl.-Ing. Dr. Caitlyn J. Collins

Institute of Lightweight Design and Structural Biomechanics

Vienna, October, 2018

Affidavit

I declare in lieu of oath, that I wrote this thesis and performed the associated research myself, using only literature cited in this volume. If text passages from sources are used literally, they are marked as such.
I confirm that this work is original and has not been submitted elsewhere for any examination, nor is it currently under consideration for a thesis elsewhere.

Signature:_____

Date:_____

Acknowledgements

I would like to express my sincere gratitude to Prof. Philipp J. Thurner, my thesis supervisor, for his continuous support, patient guidance, and useful comments through my thesis research. I would also like to thank Dr. Caitlyn J. Collins for her support, advice and help at different stages of this work.

Last but not least, I would like to appreciate my family: my parents whose love and guidance are with me in whatever I pursue. Most importantly, I am grateful to my loving wife, Sogand, for her support and care during this work.

Abstract

Bone is a stiff, porous, hierarchical structure living tissue that provides structural support to the body via the skeletal system. Bone structural integrity is crucial for the quality of life. However, bones can only bear a load until a certain limit, without experiencing permanent deformation or failure.

Therefore, investigation of fracture behaviour of weight-bearing bones of the lower limbs such as femur is of great interest. Additionally, due to the anatomical location and geometry of femur neck, it is the most common fractured location of femur bone particularly in the older adults and patients who have musculoskeletal disorders that often cause to permanent disability or mortality.

On the other hand, the mechanical and microstructural properties of cortical bone of femur neck are not adequately understood. This originates from limitations in specimen size for mechanical testing. Therefore, the size of the specimen is an essential matter in mechanical bone behaviour studies. Hence, this thesis aim to investigate the size limitation for maintaining the material continuum assumption. This aim can be accomplished by examining the structural and mechanical properties of cortical bone such as fracture toughness which explains the resistance of bone to crack beginning and propagation.

In this thesis, fracture behaviour of cortical bone was studied under three-point bending test which was conducted on single-edge-notch bending (SENB) specimens with different size, 1 mm $\times$ 1 mm, 1.7 mm $\times$ 1.7 mm, and 3 mm $\times$ 3 mm, by the transverse notched direction from different cortex positions, called anterior, lateral, medial, and posterior, from mid-shaft of two equine femurs with different ages. Due to anisotropic behaviour and hierarchical structure of cortical bone, in this thesis, elastic plastic fracture mechanics approach is the best method to evaluate the fracture toughness and fracture energy of cortical bone that was conducted using J-integral approach.

Fracture toughness of both equine cortical bone was found to be sensitive to beam size particularly in the young femur. However, most of the significant differences of fracture energy in the largest beam size still present in the smallest beam size with the lower detectability differences except for one case. Therefore, it should be feasible to use fracture energy for smaller samples where it is not possible to obtain larger samples.

Considering the anatomical locations the most significant differences in fracture toughness and fracture energy were observed in the anterior cortex of the young equine femur, which was almost twice in value compared to the other compartments. In contrast, almost no difference was found in the other cortices. Thus due to physiological loading applied by animal's weight and muscle forces, the long bone is exposed to combined loading conditions that are non-uniform. Hence, these differences in results between anatomical locations of the young femur likely occur because of structural and material property heterogeneity across the bone cross-section.

Finally, from the obtained results in this thesis, it is reasonable to use fracture energy in small samples to investigate the mechanical and structural properties of bone where it exists size limitation issue and is not feasible to obtain a larger sample. However, reducing beam sizes to allow bone testing at particular anatomical locations with reduced cortical bone thickness remains an important topic for investigation.

Contents

Chapter 1

Introduction

1.1 Motivation

Bone is a stiff, porous, and living tissue that provides structural support to the body via the skeletal system. Bones have unique roles in the body: helping to maintain its shape, protecting internal organs, and enabling movement through the transmission of forces. Structural integrity of bone is crucial for the quality of life. However, a bone can only sustain loads until it reaches a certain limit, without experiencing permanent deformation or failure[1,2].

Prominent goals of bone research include the investigation of fracture behaviour of bone, determining the risk of bone fracture, and developing tools or interventions to prevent fracture incidence. Fracture will occur when the physical force applied to the bone exceeds bone strength. Additionally, bones become more weak and brittle with age and are more likely to suffer fractures from falls that would not fracture young healthy bone[2,3,4].

Fracture events include the initiation and growth of cracks as well as the resulting complete fracture of the tissue. Fracture toughness, a measure of the resistance to fracture, is a critical aspect of bone's mechanical properties. Intrinsic and extrinsic mechanisms impact fracture toughness. Intrinsic mechanisms act at small length scales and typically involve plastic deformation, while extrinsic mechanisms act at larger length scales and contribute to crack growth inhibition via crack shielding. Due to the presence of multiscale toughening mechanisms, a thorough understanding of the mechanical behaviour of bone at the different length scales as well as anatomical locations may help to predict bone fracture risk.

In healthy tissue, bone's complex structure has developed to resist physiological loads and can

adapt its mechanical resistance through remodelling. However, bone tissue is vulnerable to some crucial factors such as environmental conditions, various genetic or metabolic bone diseases, and ageing; all of these can cause disadvantageous changes to the quantity and quality of the bone resulting in an elevated risk of fracture.

A loss in bone mass or bone mineral density, especially in the case of ageing, is considered to have a considerable influence on bone fracture risk. Research based on documents from the UK General Practice Research Database (GPRD) reported the lifetime risk of experiencing any fracture at age 50 to be 53% for women and 21% for men[5]. Thus, less than one-half of women will be fracture-free for life. The same study estimated lifetime risks of experiencing specific fractures by gender at age 50 as:

- Women: Hip 11.4% , Wrist 16.6% , Vertebra 3.1%
- Men: Hip 3.1% , Wrist 2.9% , Vertebra 1.2%

Traditionally, bone quantity has been assumed to be a predictor of bone fracture risk; specifically, an increased rate of fracture in aged and diseased bones has been primarily associated with low bone mass or low bone mineral density (BMD). BMD is defined by the amount of bone mineral per unit of cross-sectional area. Although low bone mass can explain some of the increases in fracture rates, there is increasing evidence that bone mass alone is not the only factor responsible for ageing or disease-induced fracture risks[6,7,8]. For this purpose, there has been a renewed concern in factors controlling bone quality like structure, porosity, composition, strength and, in particular, bone fracture toughness. Encouraged by the idea that a precise evaluation of bone quality could potentially be a predictor of bone fracture risk, some studies on the fracture properties of bone have focused on understanding the origin of bone toughness and the resistance of bone to crack propagation[9,10,11].

The hierarchical structure of cortical bone evolves over various length scales leading to a complex mechanical response, with contributions from each level of the structure. Due to bone's hierarchical, multiple-length scale structure, cortical bone has a combination of strength and toughness. Another characteristic of cortical bone is its heterogeneous distribution of pore density and pore geometry (e.g. Haversian canals, Volkmann canals, lacunae) that varies with anatomical location. The impact of these pores on cortical bone behaviour depends on the specimen size, the length scale under investigation, and the measurement technique[12].

Investigation of fracture mechanics of femur is of great interest since ageing, and some musculoskeletal disorders will affect bone structure by increasing porosity and decreasing cortical thickness which may result in a change in strength, toughness and stiffness properties of bone. More importantly, it is not always possible to obtain the sufficient cortical thickness in some location such as radius and femur neck to meet the requirements of a continuum assumption.
The femur neck includes a substantial amount of cancellous bone and is also a site for congenital disabilities, cysts, and osteoporosis. Additionally, the femur neck has a small cross-sectional area and a crucial part of the weight-bearing axis, which indicates that the weight of the whole body moves through it. Consequently, the femur neck is the most common fractured location of the femur bone. Nevertheless, due to the anatomical location and geometry of the femur neck, the mechanical and microstructural properties of cortical bone of femur neck are not adequately understood. This originates from limitations in specimen size for mechanical testing. Therefore, the size of the specimen is an important matter in mechanical bone behaviour studies. Hence, the aim of this study is to investigate the size limitation for maintaining the material continuum assumption for cortical bone specimens[3,13,14].
Three-point bending tests are frequently used to determine tissue level fracture toughness as relatively easy to conduct and, with the addition of a pre-notch[15-18]. Therefore, in this thesis, a three-point bending configuration was chosen to investigate cortical bone fracture toughness due to the simplicity and accuracy of the experimental setup as well as concerns for specimen geometry.
Animal models are a crucial component of biomedical and biomechanical research. Understanding how human bone is formed and develops is essential when choosing a suitable model species. The non-human mammalian species such as dog, pig, goat, sheep, cow, and horse are often selected, because they can represent certain aspects of human bone. Additionally, both qualitative information and quantitative data have been published for these species[19]. In this thesis, bovine and equine species were used. These animal models are suitable to study many aspects of the mechanical behaviour of the bone structure. In addition to that, they are easier to access, and researchers can obtain larger sample numbers compared to human bone. Furthermore, the microstructure of equine bone (e.g. osteon size/shape) is the closest to human bone. Hence, a more detailed investigation was done on the equine bone in this thesis.

1.2 Thesis Objective

Investigating the fracture toughness of bone will give insights into the relationship between mechanical properties and bone fragility in addition to the involvement of fracture mechanics in clinical types of failure of cortical bone, (e.g. vertebral and hip fractures). Nowadays, hip fracture is a common and crucial matter. Nevertheless, due to the anatomical location and geometry of the femur neck, the mechanical and microstructural properties of cortical bone of femur neck are not adequately understood. This originates from limitations in specimen size for mechanical testing. Therefore, in this thesis, the fracture toughness of cortical bone tissue was studied as a function of beam size, age, and cortex position to further our understanding of the origins of its fracture resistance.
The three principle aims of this thesis were:

1. Determine an appropriate specimen size in order to maintain the continuum assumption for cortical bone.

2. Investigate the effect of ageing on the fracture behaviour of cortical bone as dependence on specimen size.

3. Examine the mechanical behaviour of cortical bone excised from different anatomical locations of the femur and evaluate the influence of anatomical position on fracture behaviour.

In order to achieve these goals, bovine bone was first used to determine the effect of beam size on the fracture mechanical behaviour of cortical bone. Equine bone was then used to determine the effects of beam size, age, and cortex location on the fracture mechanical behaviour of cortical bone.

1.3 Structure of Thesis

In chapter 2, a general background of bone is given, and anatomical basics are described. Specifically, the differences between the two bone tissue types, characteristics of bone cells, and bone composition are given. Then, the mechanical properties of bone are described and bone fracture behaviour and fracture mechanisms are explained. Additionally, a brief overview of three-point bending mechanical testing methods and the fundamental measurement principle of fracture behaviour are given. Lastly, a brief summary on the use of large animal models in biomedical research is included.

Chapter 3 includes the materials and methods which describe the sample preparation procedures, how the experiments on the bone samples were performed and all statistical methods used to process the data.

In chapter 4 all results are presented. The bovine experimental results are presented first, followed by the equine experimental results.

In chapter 5, the results of the experiments are summarised and discussed. Additionally, the conclusions of this thesis as well as future work beyond this thesis are given.

In the Appendix, some tables and figures are given to improve understanding of the bovine and equine study results. All statistical information of the bovine bone and the equine bone are shown in appendix A and B, respectively. The descriptions of the old and young equine femurs are given in appendix B.1 and B.2, respectively.

Chapter 2

Background

2.1 Introduction

The skeletal system, vital to the body both biomechanically and metabolically, is composed of individual bones and the connective tissue that joins them. Bone is the main element of the system and differs from the connective tissues in rigidity and hardness. Bone tissue has a sophisticated arrangement of material structures at various length scales, which work to provide a variety of mechanical, biological and chemical functions[2]. Bone is one of the body's hardest and metabolically active tissues. Moreover, it remains active throughout life. Bone structure can adapt to external mechanical and chemical stimuli. Additionally, in the case of fractures and microcracks bone has the potential to heal, repair, and regenerate itself. Bone is an anisotropic, heterogeneous, nonlinear, and viscoelastic material with complicated structure-function relationships.

The human adult skeleton is made up of 206 bones, which are divided into five categories based on their shapes, as shown in Figure 2.1. Their shapes and their functions are related such that each defined shape of bone has an individual function. For example, long bones are located in the limbs, have a nearly cylindrical shape and have their long axis closely aligned with the limb axis. They provide stability of the limb and support for the limb's muscles, which are responsible for the mobility of the limb. Long bones can be divided into two kinds: weight-bearing bones of the lower limbs, i.e. femur and tibia, which carry the body weight when standing; and non-weight bearing bones in the upper limbs, i.e. radius, which does not continuously support body weight[20].

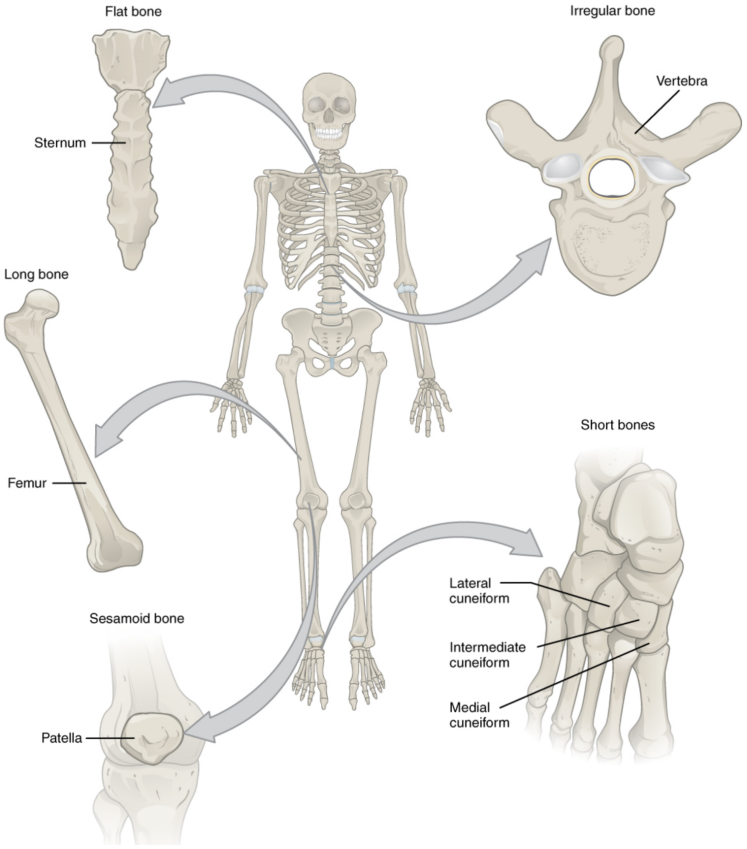

Figure 2.1: Classification of Bones[21]

2.2 Bone Structure

Bone is a complex, hierarchically structured, heterogeneous, and anisotropic material. Thus an understanding of the structure of mammalian bone is essential to comprehend the related mechanical and material properties. In order to investigate the mechanical properties of the bone tissue, it is essential to focus on both the mechanical properties of its component phases and the structural relationship between them at the various levels of a hierarchical structural organisation[22,23,24].

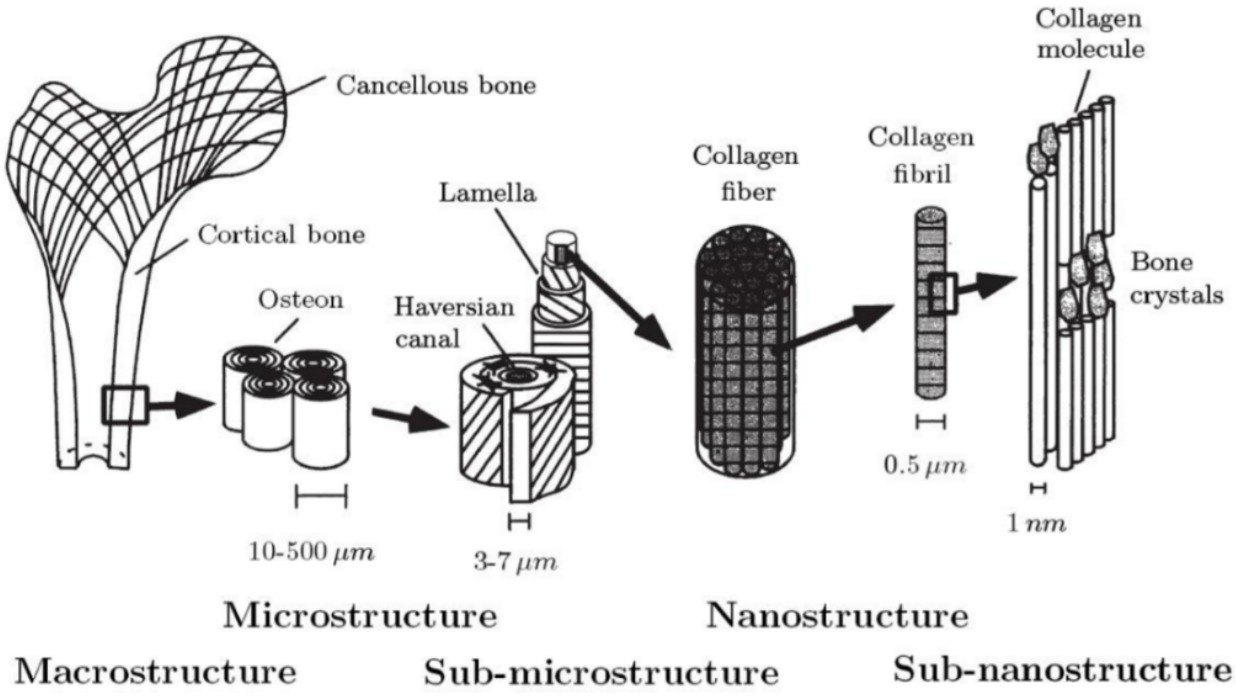

Figure 2.2: The hierarchical structure organization of bone tissue[24]

In Figure 2.2, these levels and the corresponding structures are shown[24]:

1. The macrostructure: cortical and trabecular bone.
2. The microstructure (from 10 to 500 μm): Haversian systems (osteons), lamellar bone, fibro-lamellar bone, woven bone, single trabeculae.
3. The sub-microstructure (1-10 μm): lamellae.
4. The nanostructure: mineralised collagen fibrils.
5. The sub-nanostructure (below a few hundred nanometers): collagen, hydroxyapatite and non-collagenous proteins.

At the lowest level, sub-nanostructure, exists the molecular structure of component elements, such as mineral, collagen and non-collagenous organic proteins(NCPs). At the smallest length scales, mineralised collagen fibril formed by collagen molecule arrays with a 67-nm offset, where calcium phosphate (hydroxyapatite) nanocrystals are embedded into the collagen fibrils and around each fibril[25,26].

At the next level, nanostructure, bone is composite of mineralised collagen fibrils which are the basic building block of bone, at a length scale from hundreds of nanometers to 1 μm. At the third level, sub-microstructure, these fibrils are arranged in two forms, woven bone and lamellar bone, as shown in Figure 2.3. Both cortical and trabecular bone may contain woven and lamellar bone. However, woven bone, immature bone, is replaced during skeletal maturity by lamellar bone. Woven bone is characterised by poorly organised mineralised collagen fibres where no different pattern can be observed. Woven bone is found typically in both cortical and trabecular bone of young growing animals and during the initial stages of bone fracture healing in an adult. Woven bone is mechanically weak, but forms quickly[2]. Lamellar bone is more precisely arranged. The collagen fibrils and their associated mineral are stacked in thin sheets called lamellae, about 3-7 μm wide, that contain unidirectional fibrils in alternate angles between layers. Lamellar bone is most common and can take various forms at the microstructure level.

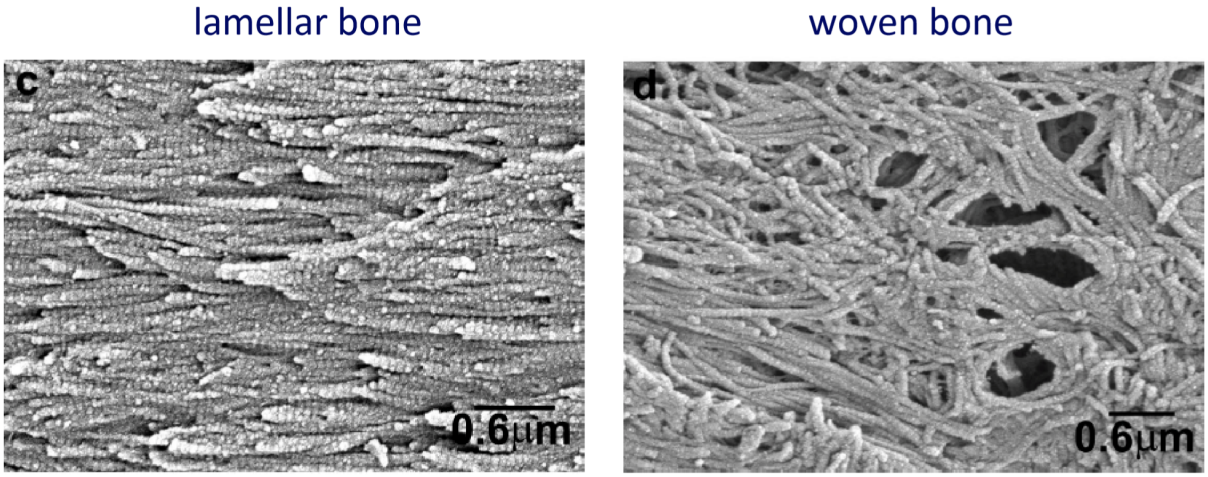

Figure 2.3: Lamellar and Woven bone[27]

Ascenzi and Bonucci introduced the parallel collagen fibre orientation theory[28,29]. This theory states that collagen fibres within the same lamella are mainly parallel to one another and have a preferred orientation within the lamellae. The direction of collagen fibres between lamellae may change up to 90 degree in neighbouring lamellae. As shown in Figure 2.4, based on this theory, three types of osteons were introduced: type L: longitudinal, type A: alternate and type T: transversal.

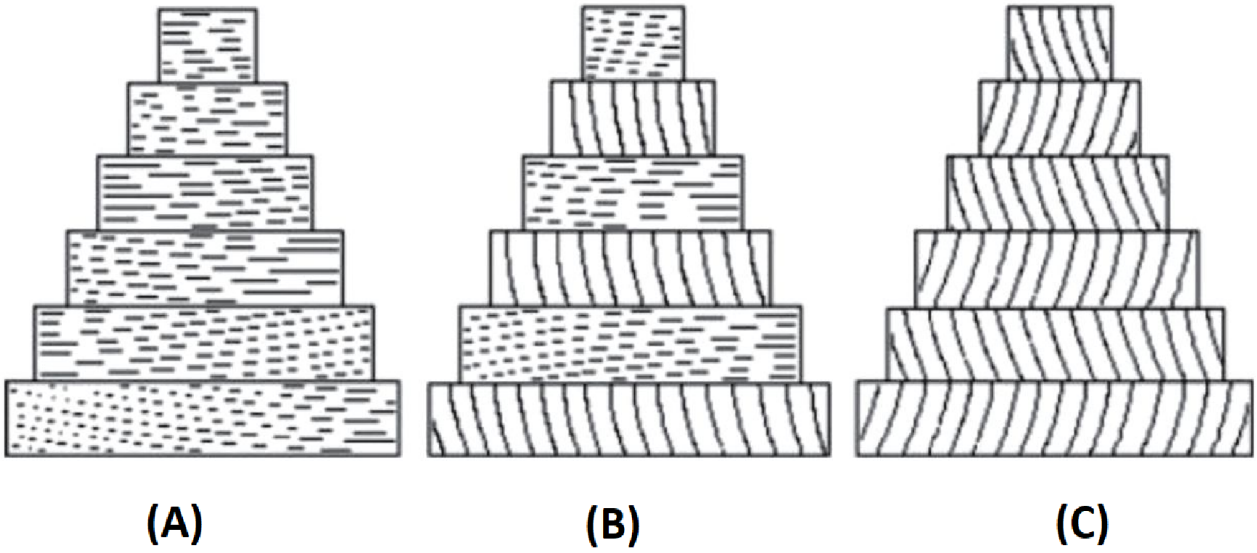

Figure 2.4: (A) type T: transversal (B) type A: alternate (C)type L: longitudinal [30]

Another theory was presented by Giraud-Guille which introduced two model of collagen fibrils arrangements: the orthogonal plywood model and the twisted plywood model[31], as seen in Figure 2.5. The orthogonal plywood model consists of collagen fibrils which are parallel in a given plane, but fibrils do not rotate continuously from plane to plane while in the twisted plywood model fibrils have more a rotational bundle orientations by an angle from 0 to 45 degrees within each lamella. Giraud-Guille believed that the orthogonal plywood model most similarly matches the type L and type T osteons from Ascenzi's model while the twisted plywood model would most likely describe the type A osteons from Ascenzi's model.

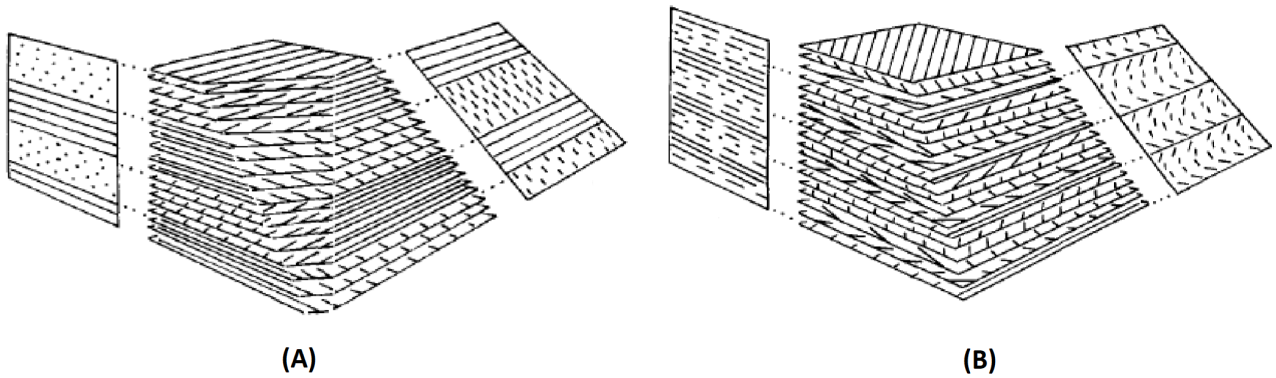

Figure 2.5: (A) Orthogonal model (B) Twisted plywood model [31]

At the next level, microstructure, primary lamellar bone consists of large concentric rings of lamellae. When lamellae of mineralised collagen fibres wrap in concentric layers around a central canal, an osteon or a Haversian system is formed. These osteons are surrounded by interstitial bone. Osteons look like cylinders of about 200-250 μm in diameter and lengths of 1-3 mm aligned to the longitudinal axis of the bone[32]. At the outer layer of the osteon is a thin border called the cement line, which has a similar thickness as lamellae. The cement line is assumed to be high in mineral and NCPs whereas low in collagen[33]. The cells within bone are located in spaces, called lacunae, between the lamellae. The cell processes connect through small channels known as canaliculi, which are used for an exchange of communication, oxygen, nutrients, and waste. The Haversian canals contain blood vessels and nerves running parallel to the long axis of the bone. Other channels, called Volkmann's canals, about the same diameter as Haversian canals, run perpendicular to the Haversian canals, providing radial paths for blood vessels on the bone surface, as shown in Figure 2.6. Two kinds of osteons can be distinguished: primary and secondary. Primary osteons are structures formed around blood vessels in the initial growth phase of bone. Secondary osteons form after remodelling. During this process, bone cells first excavate a tubular path through the hard tissue, then deposit the osteon layer by layer[2,34,35].

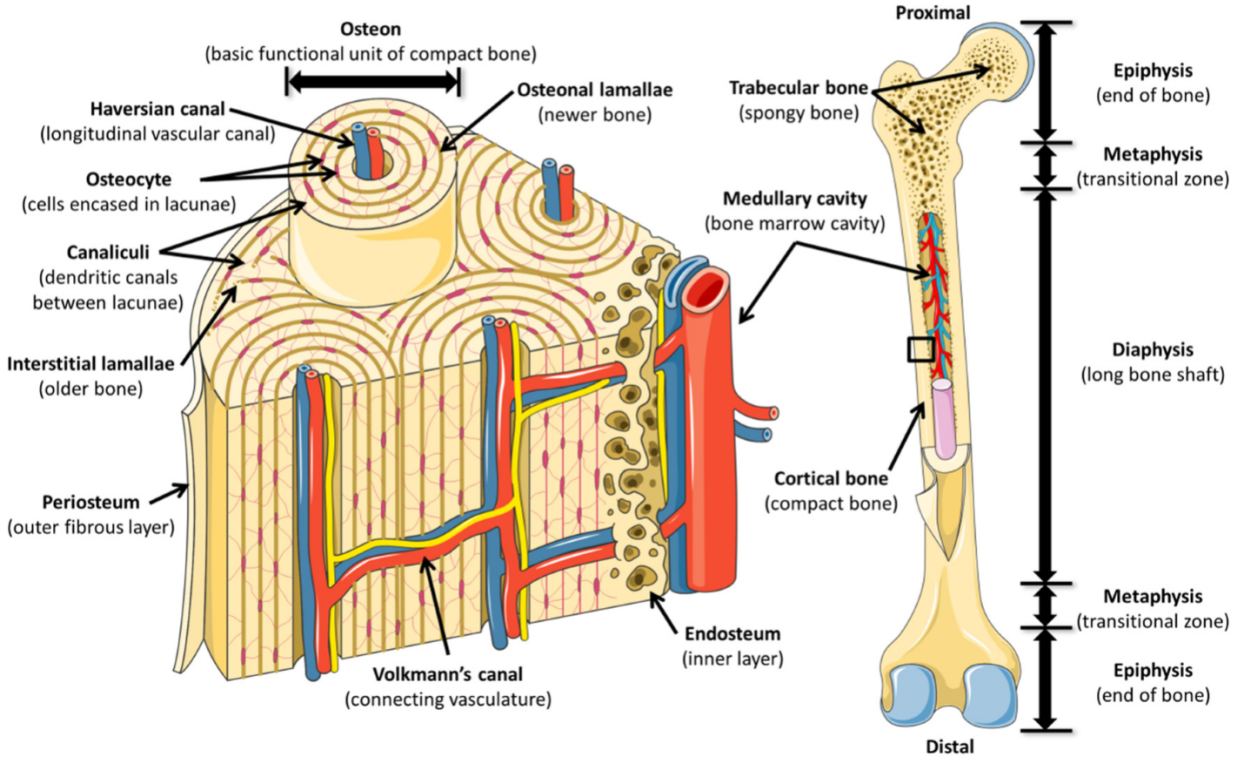

Figure 2.6: Bone Anatomy. (Left) magnification of boxed region, showing osteon and their anatomical features. (Right) Diagram of human femur, indicating the relevant terms for each bone region[36]

At the highest level, macrostructure, bone is separated into the cortical and trabecular bone tissue. Cortical bone, also known to as compact bone, is a dense, solid mass with only microscopic channels and is found in the shafts or diaphysis of the long bone and as a shell around the area of trabecular bone. Approximately 80% of the skeletal mass in the adult human skeleton is cortical bone, which forms the outer wall of all bones and is mainly responsible for the supportive and protective function of the skeleton. Cortical bone possesses a small range in porosity from 5% to 10% [37]. While trabecular bone represents only 20% of the total skeleton mass, has a porosity in the range of 45-95%, and is found in the inner parts of bones[2,35,37]. Due to its porous structure, trabecular bone is much weaker, lighter and more compliant than cortical bone, as shown in Figure 2.7. The mechanical properties of trabecular bone such as modulus and strength are different from those of cortical bone[2,35,38], as shown in Table 2.1.

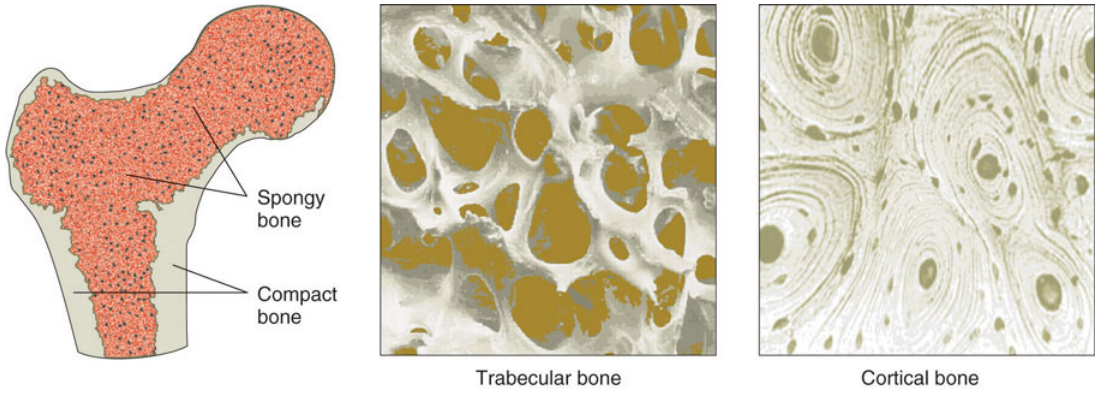

Figure 2.7: Cortical Bone vs Trabecular Bone[40]

Table 2.1: Apparent properties for transect bone in compression test

Reference	Material	Strength(MPa)	Elastic modulus(GPa)
[29]	Osteon (Longitudinal)	110	6.3
[39]	Trabecular bone	2.2	0.076
[39]	Cortical bone	170	17.9
[39]	Bone mineral(HA)	500-1000	80-110

2.3 Bone Cells

As shown in Figure 2.8, the cells specific to bone are osteoclasts, osteoblasts, osteocytes and bone lining cells[35,41-43].

Osteoclasts, bone-resorbing cells, remove damaged bone by resorption. These cells are formed from more than one cell, so they are multinuclear cells. They arise from hematopoietic stem cells in the bone marrow, and are responsive to stresses or their lack and erode bone by demineralising. Bone resorption by osteoclasts cause voids which remain inert because of an absence of stress or are filled with new bone which is formed by osteoblasts.

Osteoblasts are bone-forming cells and are located on the surface of the bone. These cells have only one nucleus and come from the bone marrow mesenchymal stem cells. Osteoblasts are sensitive to the presence of mechanical stresses. These cells produce new bone, osteoid, by depositing the organic portion of the bone matrix[44].

Bone-lining cells cover most resting surfaces of bones and control the movement of ions between the body and the bone. These cells are believed to be derived from inactive or old osteoblasts. Bone-lining cells control the way of calcium inside and outside of the bone, and they react to hormones by making particular proteins that activate the osteoclasts[43,44].

Osteocytes are the principal cell type in mature bone and are derived from osteoblasts. They are inside the bone, and surrounded by bone matrix, and end up residing in lacunae. These cells are the most plentiful type of all bone cells in the adult bone tissue. Osteocytes respond to mechanical load and changes in bone metabolism. They transmit the mechanical load through intra- and extracellular signal transmitters to induce bone formation or resorption or a combination of both[45]. The osteocytes have long branches which connect to the other osteocytes that help (1) stabilise the bone by keeping the protein and mineral content in the matrix, (2) sense and detect crack or microdamage, and (3) respond to the amount and distribution of strain within bone tissue[43].

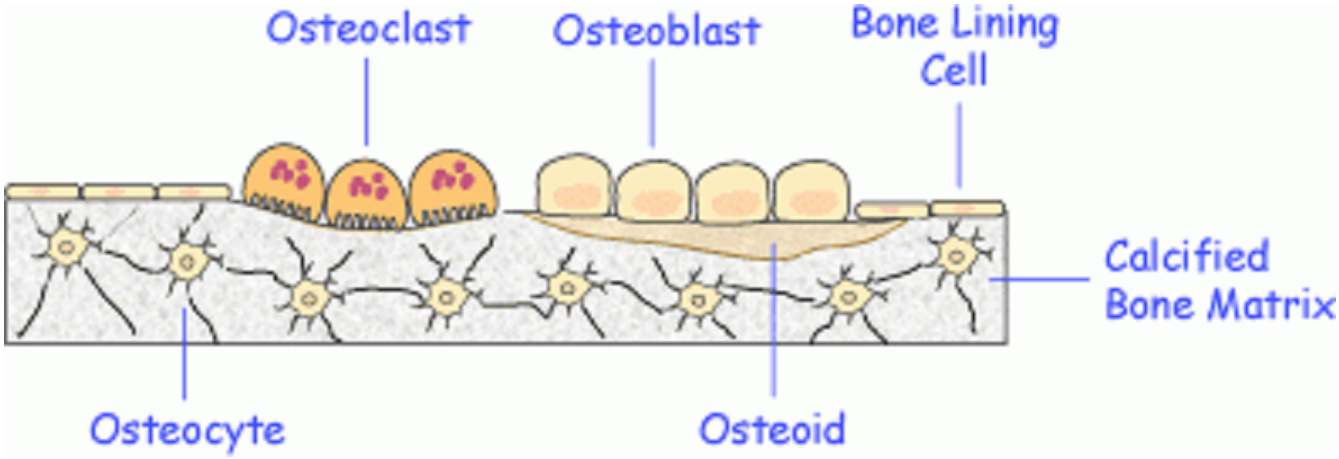

Figure 2.8: All types of bone cells[46]

2.4 Modelling and Remodelling of Bone

Throughout life, bone is continuously changing. As bone experiences greater or lesser forces, the overall structure is altered to maintain its level of function while using the least amount of bone material. Ossification and skeletal growth require two essential processes; bone modelling and remodelling. Bone modelling consists of changes in bone shape and size to allow growth and adaptation to mechanical loading and involves independent actions of osteoclasts and osteoblasts[44,47]. The process of repairing damaged bone is known as remodelling. Remodelling happens in both types of bone to repair microcracks or damage in bone. Osteoid may be added to or removed from the surface of existing bone, including the vascular cavities. During remodelling, old bone is removed under the signal delivered by damaged osteocytes and replaced with the same amount of bone in that was removed[47]. Therefore, remodelling is a balanced process; that is, bone resorption and bone formation must equilibrate to prevent dysfunctions[47-49]. Remodelling creates secondary bone which serves to strengthen and repair damaged bone, which resulted from increased stresses or fatigue damage, while modelling is typically the formation of primary bone.

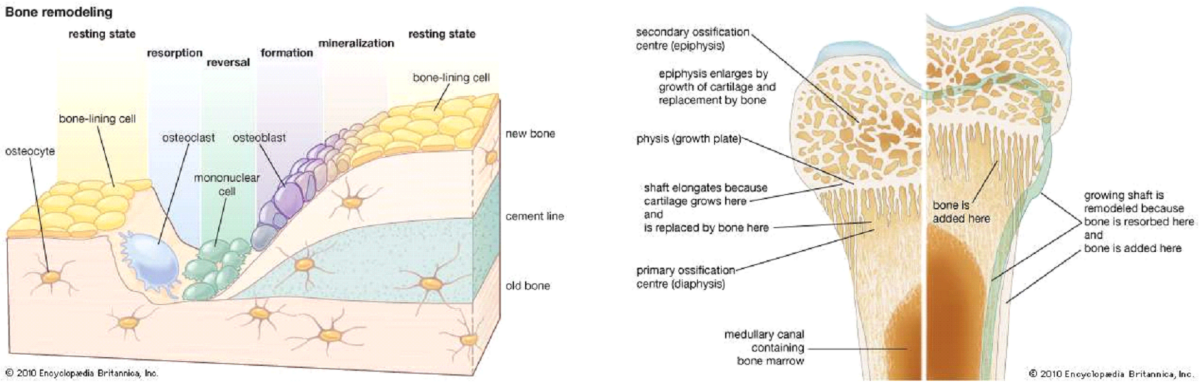

Figure 2.9: Modelling and Remodelling[50]

2.5 Bone Composition

Bone is strong and one of the stiffest structures of the body with different forms and mechanical functionalities depending on the species and anatomical position. Despite great dissimilarities,

all bones are a tri-phase composite, with each phase making a unique contribution to the mechanical properties of bone. From material aspect, bones share the same basic building components: minerals phase, organic phases and water. Generally, cortical bone composition in the long bones of human as well as some animals like horse and cow is, by weight percentage, about 60-70% apatite minerals, 18-25% organics, and 8-15% water[37].

The mineral phase consists of mainly plate-shaped nanoparticles in the form of hydroxyapatite-like crystals, a calcium phosphate-based apatite mineral, with an average size of 50 nm $\times$ 25 nm $\times$ 3 nm [51]. Apatite minerals act as fillers in an organic template, giving rigidity and stiffness to the bone. These high-stiffness (114 GPa [52]) carbonated apatite nanocrystals make up approximately 65% of the total bone mass[43] 33-43% of the bone volume[53] and are considered to be the main load-bearing components within the bone tissue.

The organic phase makes up a significant portion of bone and is consisted of mainly type-I collagen. About 90% of the total proteins are type-I collagen, while the remaining 10% is made up of the non-collagenous proteins(NCPs). NCPs play a crucial role to determine bone quality, fracture resistance and known as load-bearing proteins. NCPs are responsible for changes in microarchitectural features such as porosity, connectivity and anisotropy which are important factors in bone strength. Additionally, these proteins act as glue at the collagen mineral interface to resist the separation of the mineralised fibrils and therefore increase toughness. Therefore, removal of NCPs from bone matrix affects bone strength and changes its resistance to fracture[54]. The organic phase takes up to 35% of the total bone mass and 32-44% of the bone volume[53]. The organic matrix plays an essential role in the toughness of bone. From structural aspect, organics maintain the integrity of bone since they are much more flexible than the apatite minerals and can hold the inorganics together at greater strains without failing. Organics are also responsible for the viscoelastic and creep behaviours of bone with measured Young's modulus of only a few giga-Pascals[10,55,56].

Water is another major component of bone. It fills about 15-25% of the bone volume[53]. Water exists in firstly, free water in blood that runs through canals, vascular vessels, and lacunae; secondly, as one of the key 'sticky' agents along with non-collagenous proteins that offer additional bonding support between mineral and collagen interfaces; thirdly, in the hydration shells of apatite minerals[43]; finally, within the collagen fibrils which, depending on the degree of swelling, can impact their mechanical properties.

2.6 Bone Mechanical Properties

2.6.1 Linear "Elastic" properties

Bone is a highly adaptive material and sensitive to immobilisation, intense activity, and the level of physical loading. Bone can be adapted and may change its properties in response to the mechanical demand. The German anatomist Julius Wolff first hypothesised the theory on bone development now named Wolff's Law. This law states:

"Each change in the form and function of a bone or only its function is followed by certain definitive changes in its internal architecture, and secondary changes equally definitive in its external compliance, in accordance to the mathematics law" [57].

Biological tissue such as bone is often described concerning its structural and material properties. Structural properties characterise the tissue in its intact form. Critical structural properties are represented by a relationship between force and deformation, or stress and strain, and must be understood in order to predict how a tissue will behave in vivo. Material properties characterise the behaviour of the material comprising the tissue and, to a first approximation, are independent of the size of the tissue. Some material properties are usually expressed regarding the stress-strain relationship of the material[34,35]. The physiological loads acting on a given bone are typically characterised by some combination of external forces including tension, compression, torsion, and bending. Bones reply to these forces by deforming through processes such as elongation or stretching, compression, twisting, and bending, respectively. Strength determines the behaviour of any material under loading. When an external force is applied to a bone, there is an internal reaction. The strength may be assessed by examining the relationship between the applied load and the quantity of deformation that takes place in the bone[58].

A material mechanical behaviour is often described by the relationship between stress (σ) and strain (ε). The stress, σ *(Pa)*, is defined as the applied loading, *F (N)*, distributed throughout a material with the cross-section, *A* (m^2). Thus, for a simple tensile loading, and with the hypothesis of a homogeneous and isotropic material:

$$\sigma = \frac{F}{A} \tag{2.1}$$

On the other hand, strain, (ε) (no unit), characterises the local deformations such as changes in size and shape, which occur within a material as a result of the local stresses.

$$\varepsilon = \frac{l_1 - l_0}{l_0} = \frac{\triangle\, l}{l_0} \tag{2.2}$$

Here, l_0 *(m)* the initial length of the sample and l_1 its length after the tensile loading.

Similar to many materials, bone exhibits a linear relationship between stress and strain up to a certain point called the yield point. Bone is classically considered as a linear elastic material in order to use the slope of the stress-strain curve to determine a material modulus. The behaviour of this linear region is assumed to be a constant that is independent of the bone's size. This constant is a material property known as the elastic modulus, *E (Pa)*, and it describes a bone's intrinsic stiffness, as shown in Figure 2.10.

$$E = \frac{\sigma}{\varepsilon} \tag{2.3}$$

The yield point separates the elastic region and the plastic region of the stress-strain curve. Before the yield point, the bone is considered to be in the elastic region, and if unloaded, would return to its original shape with no residual deformation. Beyond the yield point, irreversible damage occurs, and the relationship between stress and strain becomes non-linear. The stress threshold associated with this point is known as the yield strength (σ_y). The physical meaning of the yield strength can be understood as the point at which permanent or plastic deformations like microcracking initiate within the bone tissue[59]. Even as this damage accumulates, the bone continues to support additional loading up to its ultimate strength (σ_{max}), after which catastrophic failure. The area under the stress-strain curve is a measure of the amount of energy needed to cause a fracture and is a measure of the toughness of the specimen[2,4]. Regarding the anisotropic shape of mineral particles which made collagen fibres, bone tissue is an anisotropic material, indicating that the bone behaviour will change depending on the direction of the load application.

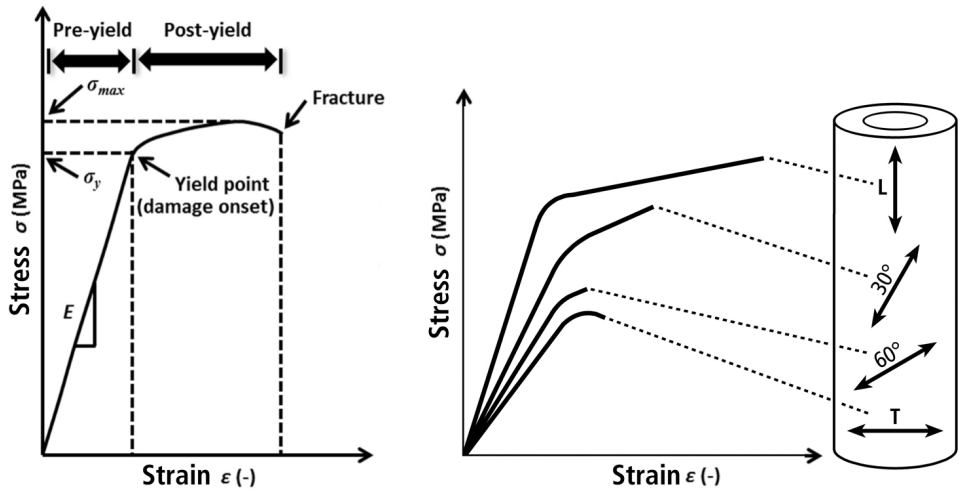

Figure 2.10: Stress-Strain curve of healthy bone.(Left) Mechanical properties for the bone like elastic modulus *(E)*, yield strength *(σ_y)*, and ultimate strength *(σ_{max})*. (Right) A graph depicting the anisotropic behaviour of cortical bone specimens machined from a human femoral shaft and tested in tension. The orientation of the load application was longitudinal (L), tilted 30 degrees; with respect to the bone axis, tilted 60 degrees;, and transverse (T). Orientation was found to strongly influences both the stiffness and the ultimate strength[60].

Additionally, bone supports higher loads in the longitudinal direction because it is used to receiving loads in this direction, as shown in Figure 2.10. Bone response differently depending on the speed to which the load is applied and the duration of loading. When bone receives the load quickly, the bone responds more rigidly and may show a higher peak force before it fails or breaks. On the other hand, when the bone receives the load slowly, the bone is not so rigid or stiff, breaking under lower forces[61].

Table 2.2: Mechanical properties of human bone tissues[62]

Property	**Cortical Bone**	**Trabecular Bone**
Compressive strength (MPa)	100-230	2-12
Flexural, tensile strength (MPa)	50-150	10-20
Strain to failure (%)	1-3	5-7
Fracture toughness (MPa.m$^{1/2}$)	2-12	-
Young's modulus (Tensile) (GPa)	7-30	0.05-0.5

2.6.2 Fracture Mechanics of Bone

Understanding the mechanical aspects of the fracture behaviours of cortical bone will help to reduce the chance of a bone fracture event in real life. Fracture of cortical bone can occur at the microscopic scale, where microcracks and defects may merge into or initiate more significant cracks and cause catastrophic failure event. Hence, investigation of the effect of bone's microstructure, bone's properties and loading conditions on crack initiation and propagation is of great importance.

2.6.3 Linear Elastic Fracture Mechanics

Bone's resistance to fracture depends on many properties and their interactions, including stiffness, the ability to resist elastic deformation; strength, the ability to resist permanent deformation; toughness, the ability to absorb energy during deformation; and fracture toughness, the ability to prevent cracks from initiating and progressing. All properties mentioned above also change with repetitive loading over time, a process known as fatigue[35,63,64].

A traditional method used to measure fracture resistance of human cortical bone is by evaluation of its mineral density, defined as the amount of bone mineral per unit of volume. However, several studies have shown that this single factor is insufficient to predict bone fracture because of its heterogeneous properties and hierarchical structure[65-67].

One of the main purposes of studying the fracture mechanics of cortical bone is to quantify fracture toughness which can be measured using different techniques such as the work of fracture and linear-elastic fracture mechanics (LEFM).

Work of fracture is obtained by dividing the area under the load-displacement curve, measured during a toughness test, by twice the nominal crack surface area. This approach has been widely used in the past to quantify the toughness of cortical bone in unnotched specimens[66]. However, in this method the results can be both specimen size and geometry dependent; therefore, it can only be used successfully to assess when the nominal sample size and geometry are kept constant[66,68].

Inglis explained that the applied stress on a material could be many times higher at sharp corners, notches, or cracks. Due to the inversely proportional relationship with the radius of curvature of the crack tip, the smaller the radius of curvature, the higher the stress concentration. The stress concentration factor depends only on the ratio of the crack size to the radius of curvature[69].

$$\sigma_{max} = \sigma(1 + 2\sqrt{\frac{a}{\rho}}) \tag{2.4}$$

where a is the crack of length and ρ is the radius of curvature of the crack tip. A stress concentration factor is the ratio of the highest stress (σ_{max})to an applied stress (σ). Inglis's theory was not completely correct because no material can support infinite stress without yielding and failing. Therefore, Griffith introduced an energy-balance approach which states that crack growth will occur, when there is enough energy available to generate the new crack surface[70]. The strain energy per unit volume of stressed linear material is derived:

$$U = E\epsilon^2 = \frac{\sigma^2}{E} \tag{2.5}$$

As shown in Figure 2.11, at each plate two triangular regions near the crack sides are completely unloaded, while the remaining material continues to feel the full stress. The strain energy U_s is calculated by the strain energy per unit volume times the volume in both triangular regions:

$$U_s = -\frac{\sigma^2}{E}\pi B a^2 \tag{2.6}$$

with propagation of crack new surface energy is created. The surface energy S associated with a crack of length a is:

$$S = 4\gamma B a \tag{2.7}$$

where γ is the surface energy (Joules/m^2) and the factor 4 is needed since two free surfaces have been formed.

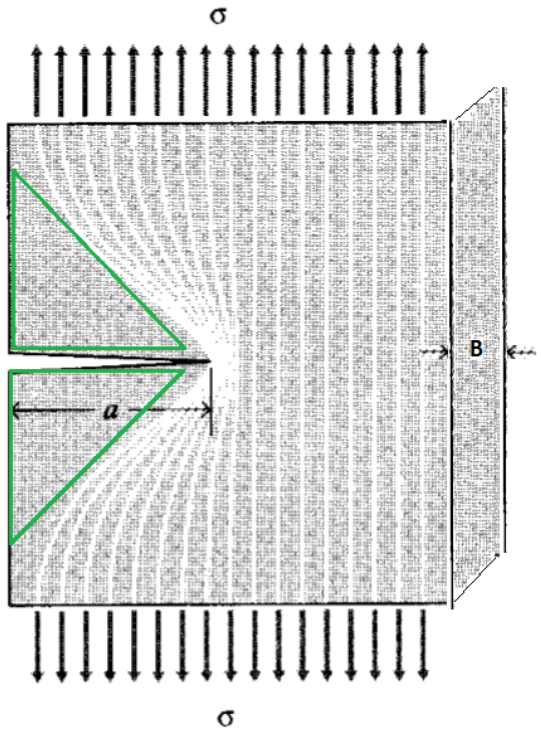

Figure 2.11: The effect of a notch on the path of stress in a loaded object

As seen in Figure 2.12, the total energy is the sum of the (positive) energy absorbed to create the new surfaces, plus the (negative) strain energy. The critical crack length, a_c, is calculated by setting the derivative of the total energy to zero. If the crack length, a, is greater than the critical crack length, a_c, the crack will propagate, and failure happens. Now the critical stress σ_f is defined by Griffith equation:

$$\sigma_f = \sqrt{\frac{2E\gamma}{\pi a_c}} \tag{2.8}$$

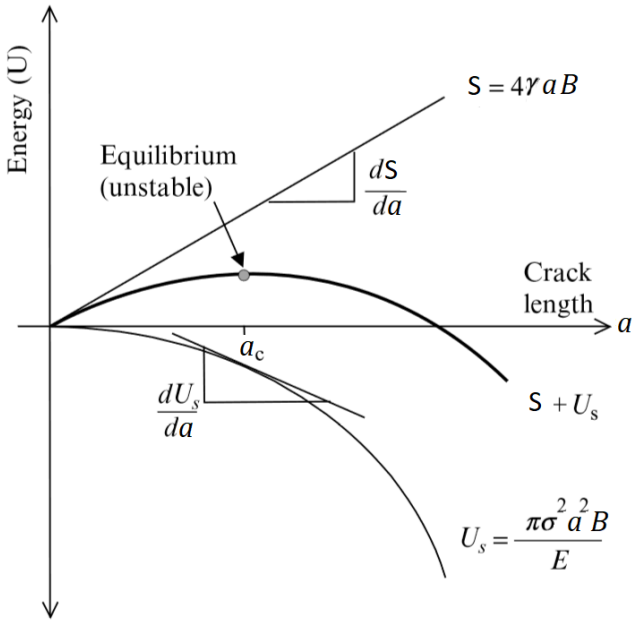

Figure 2.12: Griffith energy criterion

Wherever the material has ductile behaviour, the released strain energy was absorbed not by creating new surfaces, but by energy dissipation due to plastic flow in the material near the crack tip. This strain energy release rate, G, is calculated by:

$$G = \frac{\pi\sigma^2 a}{E} \tag{2.9}$$

$$G = \frac{K^2}{E} \tag{2.10}$$

When $K = K_c$, then G_c becomes the critical value of the rate of release in strain energy for the material which leads to crack extension and possibly fracture of the specimen.

The LEFM approach assumes that cortical bone experiences a linear-elastic fracture process with only limited plastic deformation within a small region. So the stress field near the crack tip can still be described under linear-elastic region by the stress intensity factor, K. Dr George Rankin Irwin was one of the first to study the fracture mechanisms and the behaviour of cracks in brittle materials. He introduced three different loading modes, which are still used today. Depending on the applied loading conditions, K can be described based on three fracture modes: mode I (tensile-opening mode), mode II (shear mode) and mode III (tearing or anti-shear mode)(see Figure 2.13)[71].

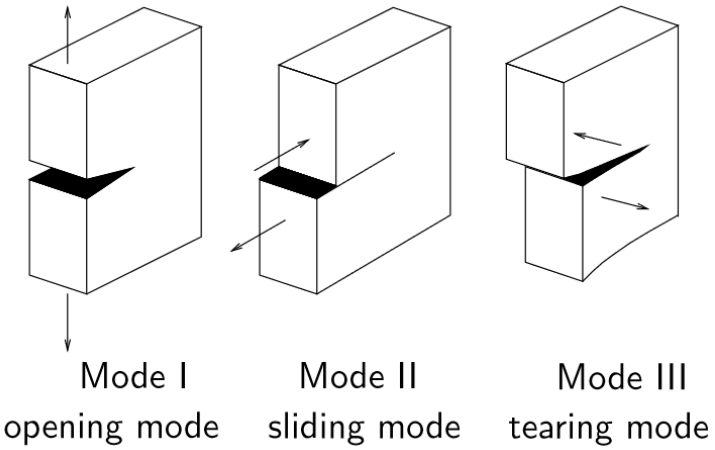

Figure 2.13: Three standard loading modes of a crack

The fracture toughness can also be described regarding the change in potential energy such as the critical strain energy release rate, G, or its non-linear-elastic equivalent form J, a critical value of the J-integral[72]. One of the differences between G and J is the validity under non-linear fracture process: the concept of G is based on the LEFM approach using linear-elastic material assumption which is only valid for elastic materials or when plasticity is negligible, while J considers for the non-linear behaviour of the material. Thus, the nonlinear elastic fracture mechanism approach is essential to assess the toughness of cortical bone with its large post-yield deformation and subcritical cracking behaviour[17,73,74]. The J-inegral method is explained in further detail in section 2.7.

2.6.4 Fracture at individual length scales

As shown in Figure 2.2, the hierarchical structure of bone significantly contributes to its high stiffness, strength, toughness and energy absorption, and better strength to weight ratio. Bone fracture is a complicated phenomenon that requires insight into the hierarchical of bone tissue. Deformation and fracture mechanisms at hierarchical structure of bone contribute to its mechanical integrity, most significantly its strength, which arises from intrinsic mechanisms at smallest length-scales. These mechanisms promote plasticity and determine the inherent resistance of the material to deformation or crack initiation. In contrast, bone toughness is determined by both intrinsic and extrinsic toughening mechanisms[11,18], as shown in

Figure 2.14.

Intrinsic toughening mechanisms act ahead of a growing crack and can be recognised as plasticity mechanisms that are derived primarily at sub-micrometre length-scales[75]. At the smallest length-scale, cortical bone deforms by stretching and unwinding of individual collagen molecules and by deformation in the mineral's crystals. Intrinsic toughening mechanisms increase the resistance to fracture by forming larger local yielding regions around crack like defects, a mechanism that protects the integrity of the entire structure by allowing for localised failure. As a result, mineralised collagen fibrils can endure microcracks on the order of several hundred micrometres size without letting any macroscopic failure of the bone tissue[66]. When a load is applied, at the nanostructural level of the bone, the mineralised fibrils separate, and cracks form between fibrils. This separation causes the energy to dissipate through the sacrificial bondings which are hidden between mineralised fibrils. NCPs such as osteopontin (OPN) proteins, interact with Ca^{2+}, form and reform sacrificial bonds as a result of that absorbing energy and increasing bone's fracture toughness. Additionally, NCPs like osteocalcin (OC) and OPN have a mechanical role in bone matrix, through dilatational band formation where microdamage accumulates as diffuse damage. Diffuse damage provides bone for absorbing large amounts of energy. However, in the lack of either OC, OPN, or both diffuse damage formation is significantly decreased. Hence, the bone tendency to fracture increases[54].

Extrinsic toughening mechanisms, at micron length-scales, act essentially to hinder cracking by 'shielding' the crack from the applied stresses when a crack tip appears; their strength in limiting the growth of cracks depends on the size of the crack[44,66,76].

Crack-tip shielding in the cortical bone is created by crack bridging and crack deflection mechanisms at the level of the osteon. Collagen fibres or uncracked regions of bone matrix, which remain undamaged in the crack path, form 'bridges' that can carry part of the load to prevent further crack extension[77]. Another extrinsic mechanism, crack deflection and twist, occurs when a crack faces the highly mineralised cement lines or the lamellae[73,76]. This mechanism promotes the crack to divert away from its original path, which causes a significant decrease in the driving force[78]. However, due to the structure of cortical bone, the aspect of porosity, which exists in the Haversian canal and cellular pores, should also be considered. Experimental investigations showed that microcracks less than 300 mm are either deflected in the region of the osteon or ended at the cement line. On the other hand, fracture surface studies show that if microcracks can grow up to a particular length (approx. 300 mm) within a Haversian, they can

then enter osteons[79]. If these cracks continue to develop through the concentric lamellae inside an osteon and have a high enough stress intensity value to break through the Haversian canal, they have a clear pathway with no limits to further growth, and catastrophic failure occurs[68].

Table 2.3: Comparison of the mechanical properties of the different wet cortical femur in various mode of loading[80]

Femur bone	**Human (20-39 years)**	**Equine**	**Bovine**
Ultimate tensile strength (MPa)	124 ± 1.1	121 ± 1.8	113 ± 2.1
Elastic modulus in tension (GPa)	17.6	25.5	25.0
Ultimate compressive strength (MPa)	107 ± 4.3	145 ± 1.6	147 ± 1.1
Elastic modulus in compression (GPa)	4.9	9.4 ± 0.47	8.7
Ultimate shear strength (MPa)	54 0.6	99 ± 1.5	91 ± 1.6
Elastic modulus in torsion (GPa)	3.2	16.3	16.8

Table 2.4: Comparison of fracture toughness of cortical bone in the transverse crack direction between human and animals

Reference	**Bone**	**Fracture toughness (MPa.m$^{1/2}$)**	**Test**
[81]	Human Femur	5.1	SENB
[35]	Human Femur	6.4	SENB
[82]	Equine Femur	8-10	SENB
[83]	Bovine Femur	5.59	SENB
[35]	Bovine Femur	5.7	SENB

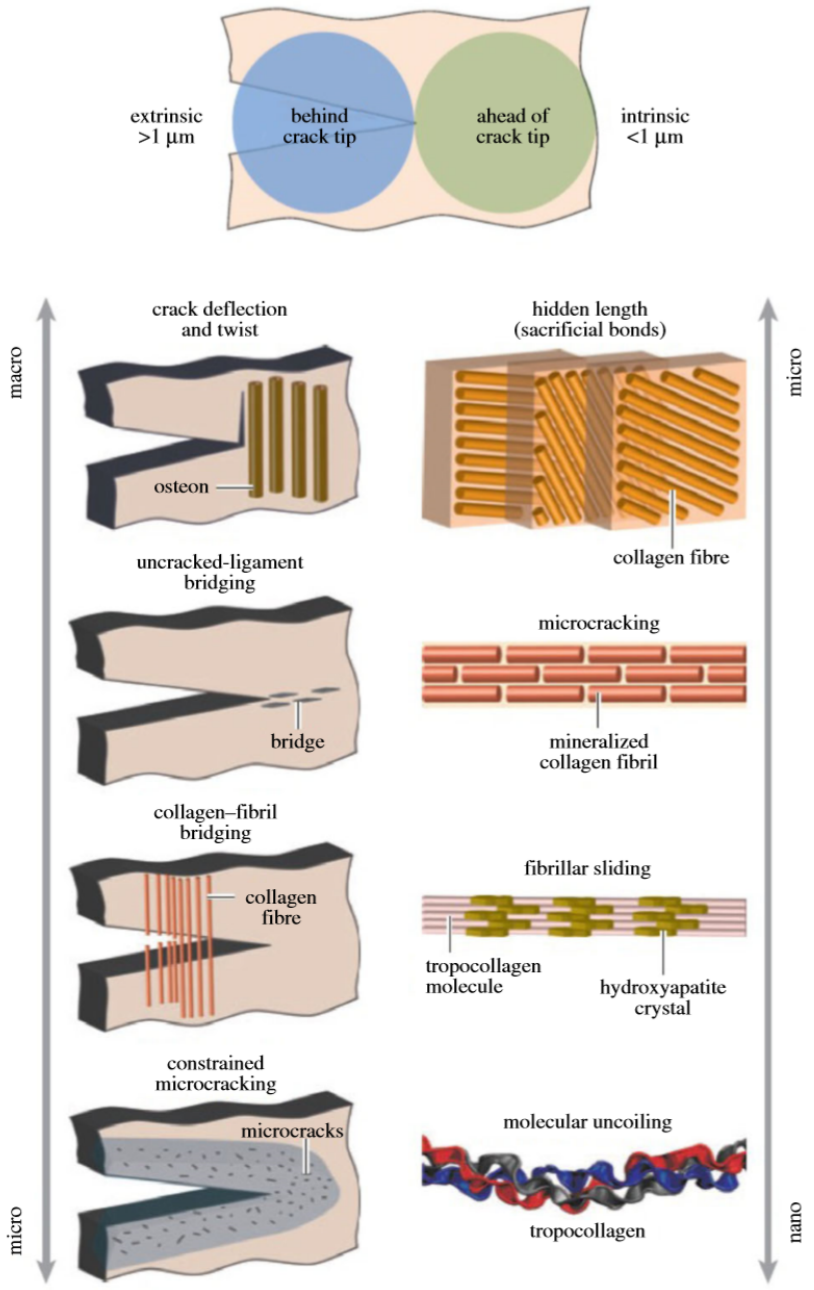

Figure 2.14: Bone toughness mechanisms at different levels of hierarchy[67]

2.7 Fracture Toughness Measurement-Three Point Bending Method

Mechanical testing can provide researchers with necessary information regarding various properties of bone. A load-deformation test is typically conducted, using tension, compression, torsion, or bending configurations[48]. Three-point bending is frequently used in bone research for characterisation of long bone biomechanical properties. In the case of fracture toughness testing, many researchers use a three-point bending test configuration as the setup and sample preparation for the notched beam are quite simple. Standards for accurate determination of fracture toughness using three-point bending testing have been established by ASTM International[84]. This test, coupled with measured geometric dimensions can be extrapolated to give the resulting stress and strain experienced by the bone. From this information, the elastic modulus, stiffness, and fracture toughness can be determined. The single-edge notched bend (SENB) specimen is widely used in determining the fracture toughness of bone. As the name states, the specimen is loaded in bending. The specimen is supported on its two ends and loaded in the plane of the notch. The configuration of SENB specimen is shown in Figure 2.15, where P is load, B the specimen's thickness, W the specimen's width ,S specimen length, and a initial crack length.

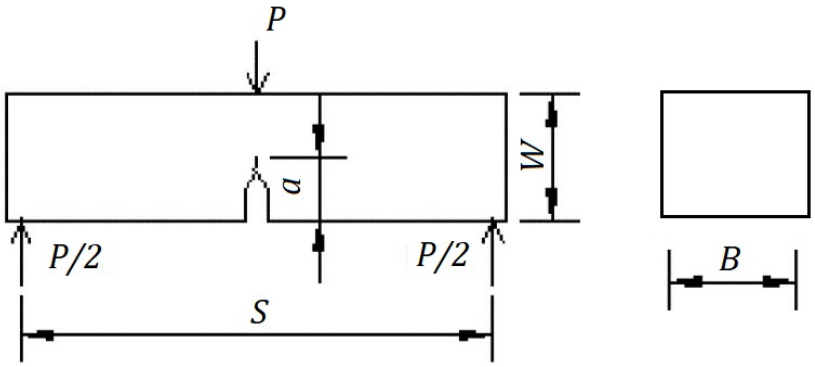

Figure 2.15: Single Edge Notched Bend

The equation to determine the stress intensity factor using this specimen is given by ASTM, which has standardised the specimen for testing engineering materials[84], as seen in (2.11).

$$K = \frac{P}{B\sqrt{W}} \frac{3(\frac{S}{W})\sqrt{\frac{a}{W}}}{2[1+2(\frac{a}{W})][1-(\frac{a}{W})]^{\frac{3}{2}}} [1.99 - (\frac{a}{W})(1-\frac{a}{W})2.15 - 3.93(\frac{a}{W}) + 2.7(\frac{a}{W})^2] \quad (2.11)$$

Non-linear fracture mechanics are better suited for evaluation of the fracture behaviour of bone because of the large degree of plastic deformation which occurs in front of the crack tip[9,20]. This plastic region is often comparable to the sample size, particularly for millimetre- and sub-millimetre-sized bone specimens. This phenomenon is identified as large-scale yielding[20]. In such a case, the specimen fracture toughness is best estimated through the J-integral[9]. Begley and Landes were introduced the first approach of the J-integral[85] which could be experimentally determined from the energy release rate:

$$J = -\frac{dU}{Bda} \quad (2.12)$$

where U, B and a indicate the strain energy, specimen thickness and crack length, respectively. Regarding the Begley and Landes model, J is calculated with determining the energy absorbed from the load-displacement curve. However, this technique is time-consuming since many specimens need to be tested and analysed to evaluate a single result of J. Therefore, Rice introduced a more useful way to calculate J directly from the load-displacement curve of a single test specimen[86]. Either the load controlled from Equation 2.13 or displacement controlled from Equation 2.14.

$$J = \frac{1}{B}\int_0^P \frac{\partial \Delta}{\partial a} \mathrm{d}P \quad (2.13)$$

$$J = -\frac{1}{B}\int_0^\Delta \frac{\partial P}{\partial a} \mathrm{d}\Delta \quad (2.14)$$

where P indicates the applied load; Δ is the specimen displacement, and U represents as the area under the load-displacement curve.

Three years later in 1976, Sumpter and Turner offered an alternative method of Equation 2.14 that based on the limit load analysis[87].

$$J = \frac{\eta}{(W-a)B}\int_0^\Delta P d\Delta = \frac{\eta A}{(W-a)B} \quad (2.15)$$

where W is the specimen width; a is the crack length, and η is a dimensionless geometry factor relating J and the strain energy, and A indicates the total area under the load-displacement curve, which is the total work done by the external force during the test.

As shown in Figure 2.16, the total area, A, under the load-displacement curve can be divided into two regions; first the elastic region, A_{el}, unloading path, and second the plastic region, A_{pl}. Thus, this unloading path separates the total displacement Δ into an elastic part, Δ_{el}, and a plastic part, Δ_{pl}. Hence, the J value can also be divided into two parts:

$$J = J_{el} + J_{pl} \tag{2.16}$$

where J_{el} and J_{pl} are the elastic and plastic regions of J, respectively. The elastic part of J can be directly calculated from the stress intensity factor.

$$J_{el} = \frac{K^2(1-\nu^2)}{E} \tag{2.17}$$

where K is the stress-intensity factor; $\nu = 0.33$ is the Poisson's ratio; E is Young's modulus. While the plastic region of J can be determined:

$$J_{pl} = \frac{2A_{pl}}{Bb} \tag{2.18}$$

where b is the uncracked ligament length; and A_{pl} is the area of the plastic region under the load-displacement curve.

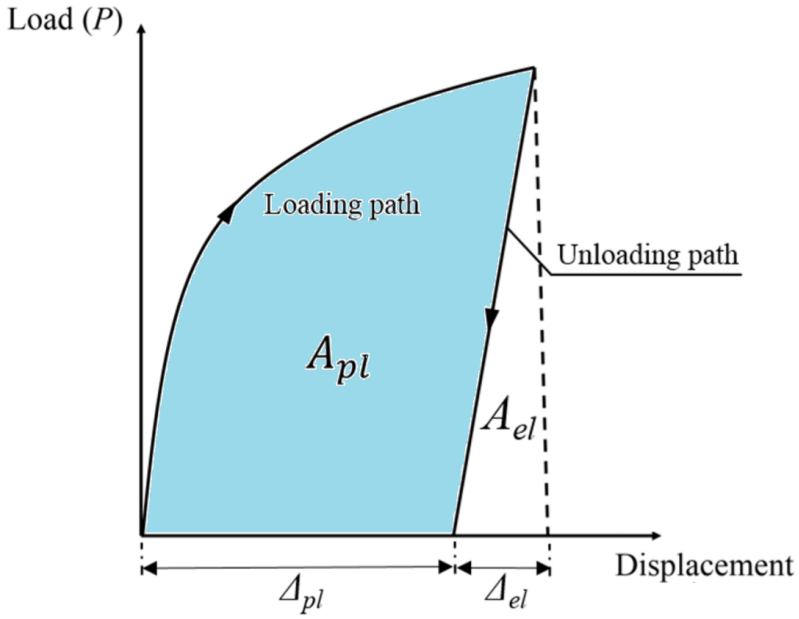

Figure 2.16: Elastic and Plastic areas under the load-displacement curve

Herein, E is the elastic modulus for a notched sample, which was calculated by Equation 2.19, where S_s is the support span in mm, B, W and a are the depth, width, and the length of the notch in mm, and m is the slope of the linear part of the load-displacement curve in N/mm as defined in[10]. The equivalent effective stress intensity K_{eff} was calculated from J and E using Equation 2.20.

$$E = \frac{{S_s}^3 m}{4B(W-a)^3} - 22.6a - 72.7a^2 \ [a \ in \ mm] \tag{2.19}$$

$$K_{eff} = \sqrt{JE} \tag{2.20}$$

2.8 Animal Models

Human cadaveric bone has often been used to study the fracture properties of bone. However, the limited availability of human tissues can lead to difficulties in obtaining different specimen populations for fundamental and comprehensive studies concerning the effects of diseases or clinical treatments on bone fracture properties. Due to ethical and logistic concerns, the use of human bones for research testing is limited. Therefore, large animals like horse, cow, pig, and sheep are commonly used to substitute human bone in biomedical and biomechanical studies since their bone tissue is relatively inexpensive and is readily available. Adequate features of an animal model include an exhibition of similarities with human tissue concerning physiological and pathological attention as well as being able to examine different subjects over a short time span[88-90].

For choosing the species of animal for an appropriate model, several factors should be considered. Some of these factors include: cost to acquire, availability, ease of handling, biological characteristics similar to humans, an existing database of biological information for the species, and also the size of the animal need to be considered to ensure that it is suitable for the research[90].

In order to choose an animal model to investigate biomechanical properties of bone, it is essential to know severe differences in macrostructure and microstructures between human and animal bone. Firstly, at macrostructure level, animal bones compared to human bones have a higher density relative to size, low porosity, and can be denser in cross-section. For instance, cortical thickness of the femur in large animal is twice of the total diameter in comparison to human[91,92]. On the other hand, the inside of animal leg bone is absent of trabecula compared to long human bones. Secondly, at a microstructural level, in human cortical bone, osteons and interstitial bone are uniformly spaced while osteon in animal bones tend to arrange in rows (osteon banding) or rectangular formations (plexiform bone)[91-93].

Below are short explanations of some of the structural properties of bone in several large animals such as pig, cow, horse, goat, and sheep[19]; a summary of relevant microstructural properties are given in Table 2.5.

Pig: Long bone, e.g. femur, of mature pigs consist fundamentally of plexiform bone with thick Haversian bone found at the posterior cortex of the bone. Haversian canals are often smaller in shape to compare with the human. In contrast, the cortical bone of immature pig femur includes layers of lamellar bone with primary tissue including osteonal banding [94-96]. In the immature pig, plexiform bone may also exist throughout the whole long bone, with a total lack of Haversian tissue or osteonal banding[94,97].

Cow: In mature bovine long bones, a well-organised plexiform structure, distinguished by a three-dimensional network of vascular canals, can be found [98]. Bovine osteons usually few in number, oval, and irregularly scattered in amongst abundant interstitial tissue. These osteons consist of a vascular canal, typically surrounded by 5-7 lamellae[99]. The cortical bone of the immature cow includes plexiform bone near the periosteal surface, Haversian bone located near the endosteal surface, and osteonal banding at the interface between both [94,97]. Haversian canals are smaller in size and irregular in shape to compare with the human. Fetal calf femur also shows the same pattern, plexiform bone tissue near the endosteal surface, a middle part of the laminar bone with an irregular arrangement, and a periosteal area of Haversian bone[94,95].

Horse: Mature horse long bone consists of thick circular Haversian tissue with plexiform tissue and remnants of a large number of attaching, primary Volkmann's canals, giving the secondary bone a reticular aspect which is common in horse[94,100,101]. Typically, a large number of osteons are gathered together, and all tend to have a higher number of lamellae (often up to 10). These osteons are more regularly shaped in contrast with those of cows. Additionally, in adult horse bone the outer lamella is typically well defined and simply recognisable[99]. Due to different anatomy and movement between horse and cow, horse femur sustains large mechanical stress. Hence, diameter and area of osteons and Haversian canals are typically higher in horses compared to cow. Foal cortical bone consists primarily of plexiform bone with rows of pseudo-osteons with Haversian canal structures. The pseudo-osteons include woven bone, and due to that, they differ from Haversian systems[100,101].

Goat: Cortical bone of the femur in mature goats consists of both plexiform and Haversian bone tissue. Plexiform bone with spread areas of Haversian tissue is found near the outer fibrous layer. Goats have smaller Haversian canals and secondary osteons than humans. The form of the secondary osteons is differently described as circular, oval, irregularly round and irregular. A compound of Haversian tissue with large, irregular Haversian systems and primary tissue exists in the osteons zone, and thick Haversian tissue is placed near the inner surface[94,102]. Immature goats will more likely present full amounts of plexiform tissue as the primary tissue of growth[94,103].

Sheep: The cortical bone of mature sheep is similar to goats from the histological aspect. Haversian systems are nonuniformly scattered throughout different bones. Sheep are characterised as having a predominantly primary bone structure where osteons are containing at least two central blood vessels and the lack of a cement line[104], in contrast with the largely secondary bone of humans[105]. Immature sheep show plexiform bone throughout whole parts of the femur, with a potential for a small number of scattered Haversian systems located in posterior region of the cortex[94,96].

As a consequence bovine and equine cortical bones were used in this thesis to evaluate structural and mechanical properties. Hence, in the initial study, the cortical of bovine bone was used to assess the effect of beam size on the fracture behaviour. However, from the microstructure of bovine cortical bone, it can be understood the bovine bone is not a good comparison to human bone. Therefore, for further investigation equine cortical bone was used since the equine microstructure of bone is the closest to human bone.

Table 2.5: Comparison of some parameters of cortical bone between human and animals

Reference	**Sample**	**Bone**	**Haversian Canal Diameter (μm)**		**Haversian Canal Area (μm^2)**	**Osteon Diameter (μm)**		**Osteon Area (μm^2)**
			Min	**Max**		**Min**	**Max**	
[**106**]	Horse	Femur	29.37	45.12	1213.83	183.74	238.5	35506.87
[**99**]	Horse	Femur	33.4	50.9	1824.8	156.2	211.6	30483.9
[**106**]	Cow	Femur	30.99	42.56	1176.37	181.49	238.46	36067.23
[**99**]	Cow	Femur	20.7	36.5	717	128.8	195.3	23576.9
[**107**]	Cow	Femur	15.58	48.76	1224.71	76.22	269.63	32664.97
[**107**]	Sheep	Femur	11.48	33.63	609.23	65.11	206.27	21034.67
[**106**]	Sheep	Femur	18.36	31.76	574.13	123.79	169.66	16457.6
[**106**]	Pig	Femur	26.23	36.18	826.45	180.72	232.26	33118.87
[**107**]	Pig	Femur	15.61	40.60	1015.21	83.15	211.07	28031.8
[**107**]	Human	Femur	32.26	59.99	2164.15	90.20	263.76	37762.06
[**106**]	Human	Femur	41.15	68.73	2877.37	206.44	263.91	44119.88

Table 2.6: Comparison between the material properties of between human, equine and bovine long bones[108]

	Ultimate bending strength (MPa)	**Young's modulus (GPa)**	**Yield strain in bending**
Human	208	14.8	14100
Equine	247	19.9	12400
Bovine	179	18.7	9000

Yield strain=Ultimate strength ÷ Young's modulus

2.9 Micro-computed Tomography

Micro-Computed Tomography (μCT) technique is a nondestructively imaging tool for the generation of high-resolution three-dimensional images, which provide to observe the internal structure of materials such as bones or soft tissues.

In μCT x-rays are radiated from an x-ray generator, pass through a specimen, and are recorded by a detector on the other side to generate projection images. These two-dimensional projection images are taken gradually over a rotation of the specimen of either 180 or 360 degrees and mathematically transformed to display a three-dimensional image. The principle of μCT is based on the attenuation of x-rays passing through the specimen which happens by two absorption types; 1) Partial absorption: when some x-ray photons are absorbed in the object while others are transferred to the detector. 2) Differential absorption: when different materials within the object have different absorption features to give contrast. If there is no differential absorption, the result appears as a uniform grey level. The x-ray absorption of a material increases with the atomic number of the components it includes as well as with its density, causing it easy to detect different structures if they alter in their elemental composition, thickness or density[109]. One of the most important types of μCT analysis in the bone biomedical research is a morphometric analysis derived from histomorphometry which includes some parameters such as bone volume *(BV/TV)* and cortical thickness.

The μCT analysis process is divided into three steps: first the physical scan; second the reconstruction; and third, obtaining quantitative data from a selected part of the image. In order to apply the morphometric analysis, two steps need to be carried out with a reconstruction phase. Firstly binarisation, also known as segmentation, and secondly selection of the volume of interest(VOI). The grey level images generated by reconstruction consist of voxels which have 256 grey levels if the images are 8-bit. In the binarised image, black indicates bone and white indicates void. The easiest and fastest method is 'global thresholding' which means setting a single threshold grey level density value so that every voxel with an equal or higher value is represented as a solid colour, and lower values represented as space. Global thresholding is generally sufficient for obtaining morphometric data where the bone images are of adequate quality[110,111].

Chapter 3

Methods and Materials

3.1 Specimen Preparation

3.1.1 Bovine Bone Preparation

Sections of midshaft cortical bone from bovine femurs were provided by the MMLAB of the Technical University of Vienna. The diaphysis of the femur was sectioned and prepared for machining into SENB specimens (see Equine Bone Preparation for details). However, the age of bovine bone was unknown. All bovine bone specimens were stored in a freezer at -20 °C.

3.1.2 Equine Bone Preparation

Equine femurs were immediately brought to the MMLAB of the Technical University of Vienna from a local slaughterhouse in a hard plastic bag surrounded by ice. Fresh equine femur bone tissues were obtained from two horses, ages eleven and five years(Figure 3.1).

Figure 3.1: Five year old (Left)and eleven year old (Right)frozen horse femura

All equine bone specimens were stored in a freezer at -80°C, The epiphysis was removed, and the middle diaphysis of each equine femur was sectioned into 40 mm cylinders using a tooth handsaw. Then, the diaphysis part of each femur was sliced using a Diamond band saw (Exakt 300 CP, Germany) into four cortices Anterior, Posterior, Medial, and Lateral (Figure 3.2).

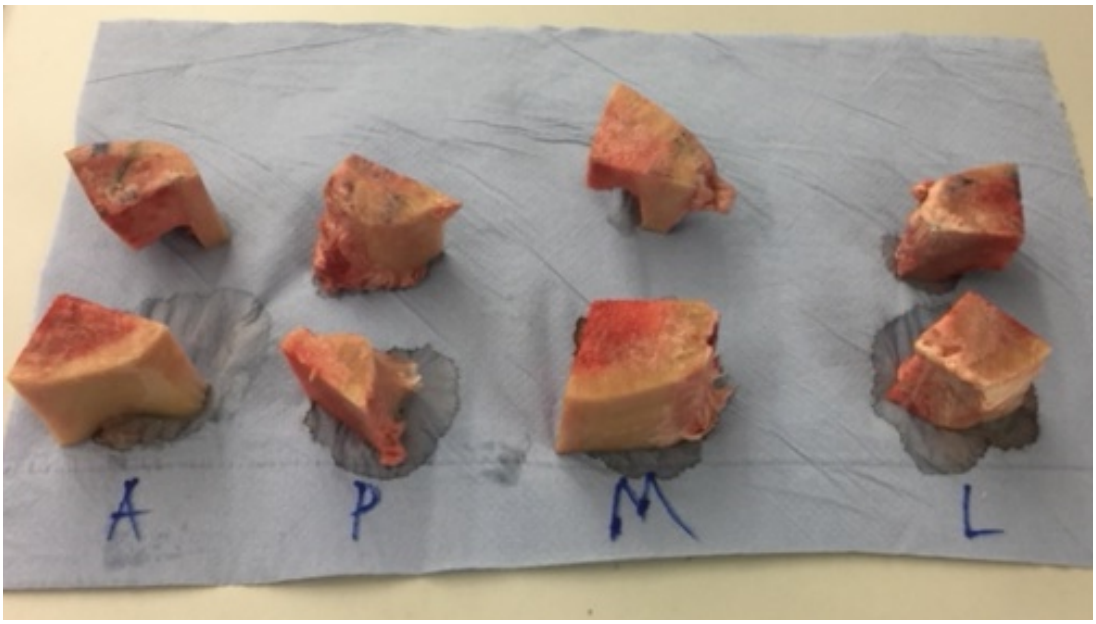

Figure 3.2: Four cortex of horse femur. (A), (P), (M), and (L) indicate Anterior, Posterior, Medial, and Lateral, respectively.

The anatomical location of the femur and the sample orientation used in the experiments are illustrated in Figure 3.3.

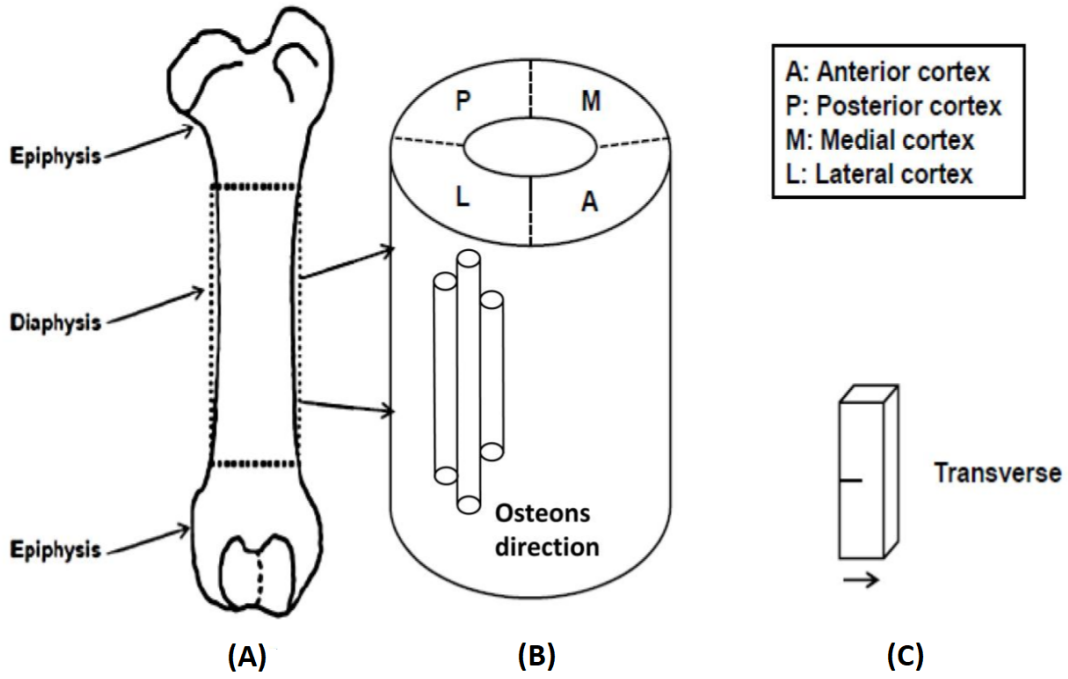

Figure 3.3: (A) schematic illustration of a femur; (B) cortex positions in cortical bone;(C) schematic illustration specimens with different crack propagation directions[112]

In order to investigate the effect of beam size on the mechanical properties of bovine and equine cortical bone, three-point bending tests were conducted on SENB specimens of varying size. Cortical bone from the femur midshaft was machined into SENB specimens using a low-speed saw (Buehler Isomet, LAKE BLUFF, IL, USA)(Figure 3.4) and a diamond coated blade according to the ASTM E120-16 standard. All specimens were polished with carbide papers (P800, P1200 and P4000) until the surfaces appeared smooth under optical microscopy. Once the surface was clean, without any scratches or irregularities, the specimen was notched (Figure 3.5) and loaded under three-point bending conditions. The notch was positioned perpendicular to the predominant osteonal direction, generating transverse SENB specimens (Figure 3.3). During cutting and polishing, a constant spray of water was supplied to keep the bone from heating and to keep it wet. Specimens from all groups were submerged in Hanks Balanced Salt Solution (HBSS, pH=7.4) a few hours before testing and were tested in hydrated condition. The final SENB beam dimensions were shown in Table 3.1.

Table 3.1: The final SENB beam dimensions

Beam size	**Thickness**	**Height**	**Length**	**Support Span**	**Height/Support Span**
Beam 3 mm	3 mm	3 mm	22 mm	18 mm	0.17
Beam 1.7 mm	1.7 mm	1.7 mm	14 mm	10 mm	0.17
Beam 1 mm	1 mm	1 mm	10 mm	6 mm	0.17

A total of 324 specimens were machined for the experiments. The beams were tested using a servo-electric load frame (SEL-mini Thelkin, Switzerland) under three-point bending test conditions. The beam sizes and support spans were selected to maintain a constant length to diameter ratio across all tests. For these tests, a 100 Newton load cell was used to record the force, crosshead position was used to track displacement, and a high-resolution camera (Messphysik Video Extensometer ME46, Austria) was used to track crack propagation. The obtained force, displacement, and videography data were evaluated using an adapted version of the "Whitening Front Tracking Method"[113] in Matlab (version 2017) to determine structural and mechanical properties. In this report, initiation toughness (K-Initial), a linear fit to the instantaneous fracture toughness (K-Slope), effective fracture toughness (K-Max), effective modulus (E), initiation fracture energy (J-Initial), crack growth resistance (J-Slope), and effective fracture energy (J) are considered.

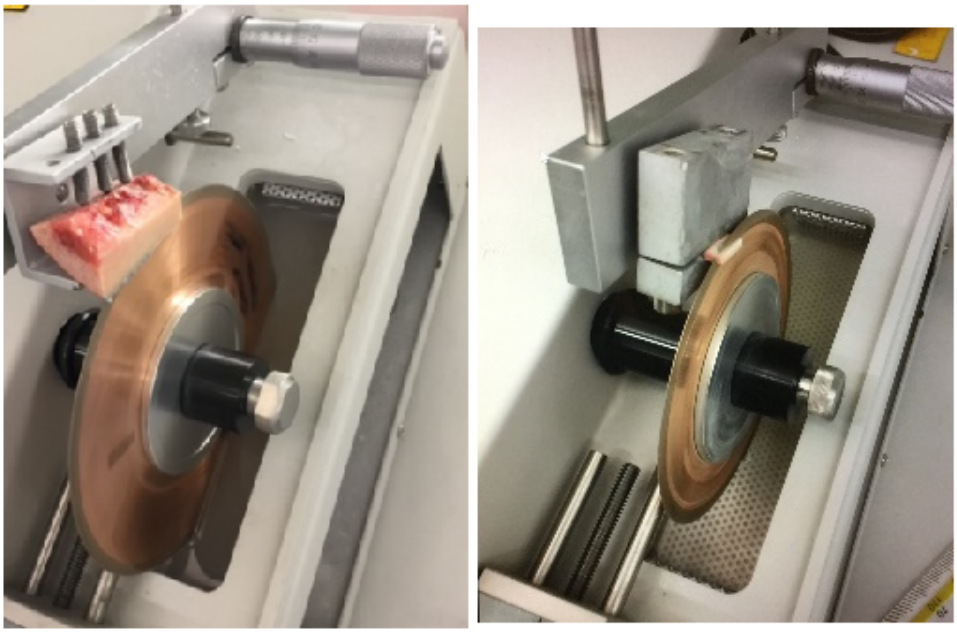

Figure 3.4: Cut bone with low-speed saw

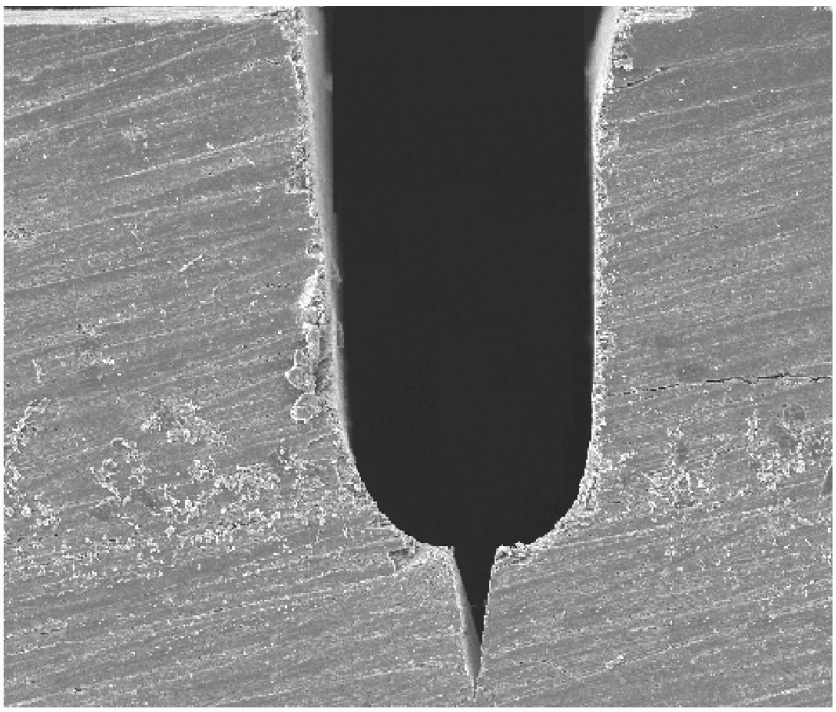

Figure 3.5: Notched and polished beam

3.2 Micro-Computed Tomography

Micro-computed tomography (μCT) was used to determine cortical porosity. All cortical bone specimens from the equine femurs were scanned using μCT(Switzerland, The Scanco Medical μCT 100) at 70 kV and 114 μA with a voxel resolution of 10 μm. Before scanning, all beams were brought to room temperature while immersed in Hank's Balanced Salt Solution (HBSS) within a large test tube. A low X-ray attenuation plastic holder was used to hold each beam in place for scanning. Image analysis of all beams was performed using BoneJ [114] to determine bone volume fraction, BV/TV, which represents the thresholded bone tissue volume to the total sample volume, and reported as a %.

3.3 Statistical Methods

Statistical analysis of results was performed using the Datalab (version 3.5), Python (version 2.7.14), Matlab (version 2017), and R (version 3.4.1). For the different beam sizes, the mean height and standard deviation in height were calculated. Analysis of Variance (ANOVA) tests were used to determine if there were any significant differences in the structural and mechanical properties of the beams machined with different heights. ANOVA tests should meet two conditions:

1) The samples should be normal distributed

2) The variance of the samples should be equal

Therefore, Shapiro-Wilk tests were conducted to ensure the first condition was met and Bartlett tests were applied to ensure the second condition was met. Outlier detection was used to assess the data. Regression models were used to find the best fit model for each data set, and then the interquartile range *(IQR)* was used to detect data points that were more than $1.5 \times IQR$ above the third quartile or below the first quartile. Afterwards, any outliers were removed. When the distribution of the data was not normal or the variances of data sets were not equal, Kruskal-Wallis Tests were used to determine if there were significant differences between groups. In the last step, Tukey tests were used to compare the means of all groups. The Tukey test

output gave the difference in means, confidence levels, and the adjusted p-values for all possible beam size pairs.

All of the above mentioned statistical analyses were used to determine any significant differences of different beam sizes in the different anatomical location as well. Additionally, the T-test was used for comparison the age to find significantly different between the age of two donors. T-test has the same conditions as ANOVA test. However, if the two groups have unequal variance, Welch's test was used instead of T-test. In this report, boxplots were obtained to provide an overview of the collected data and to enable comparison of the mechanical and structural properties of each beam size.

As shown in Figure 3.6, the description of a boxplot, all boxplots show corresponding medians (red horizontal lines) of each group of parameters. Horizontal lines of the blue box boundaries indicate first and third quartiles. Whiskers (long single vertical lines) indicate variabilities from maximum to minimum, and red '+' markings on the boxplot graphs indicate outlier values (i.e. lying out of the inter quartile range).

In this study, the level of significance was set to $\alpha = 0.05$, corresponding to a confidence level of 95%.

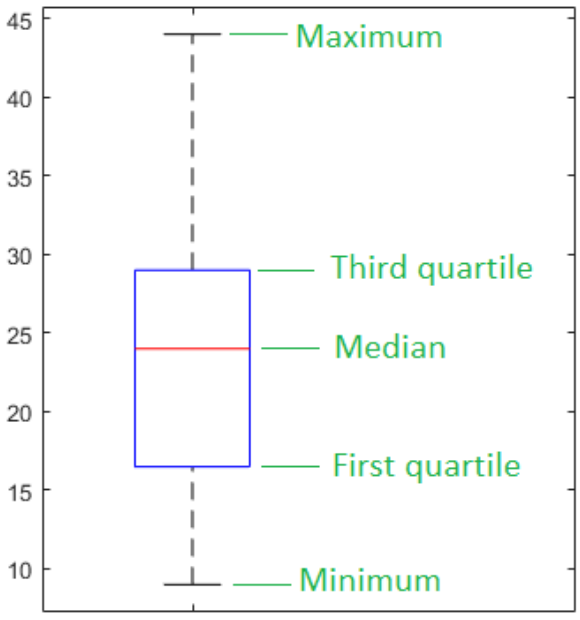

Figure 3.6: Description of a boxplot

For a better understanding of the results chapter, as seen in Figure 3.7, the all parameters indicate in the R-curve. However, it should be mentioned that the codes were used to determine the initial values of fracture energy and fracture toughness, J-Initial and K-Initial, by extrapolating leading to negative values. Therefore, these values are not reported here as not meaningful. When the crack extends the slope of the curves slightly reduces by increasing beam size. In contrast, the effective value of fracture energy and fracture toughness, J and K-Max, is enhanced with the crack extension that means resistance to crack propagation increases substantially in beam size 3 mm than the beam sizes 1 mm and 1.7 mm.

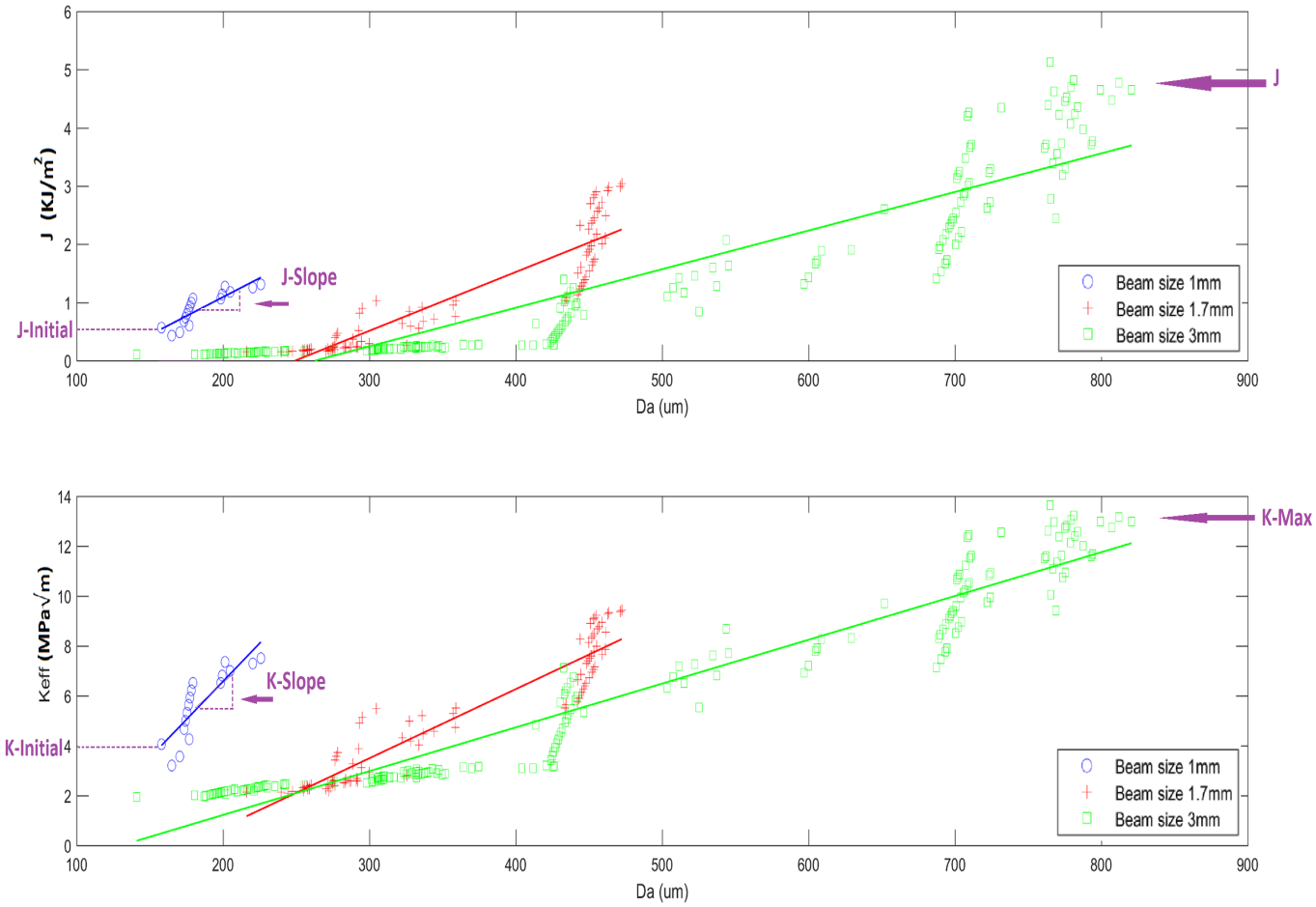

Figure 3.7: Crack resistance curves of different beam sizes shown in terms of J and K_{eff}

Chapter 4

Results

4.1 Bovine Bone

4.1.1 Introduction

Fracture mechanics properties of bovine cortical bone from the femur mid-shaft were determined under three-point bending test of notched (SENB) samples. This first study was conducted to determine whether fracture toughness, fracture energy and effective modulus were influenced by beam size. Detailed statistical summary tables for the bovine cortical bone samples can be found in Appendix A.

4.1.2 Fracture Toughness properties

In this section, the results on K-Slope and K-Max of bovine femur are presented. All of the above-mentioned mechanical properties were normally distributed except K-Max of the 1.7 mm beams, which had p(W)=0.0002. In this case, one outlier was found and removed. Afterwards, K-Max for the 1.7 mm beams became normally distributed. All variables for each beam size were found to have equal variance. As seen in Figure 4.1, no significant difference was found in the means of K-Slope for any beam size.

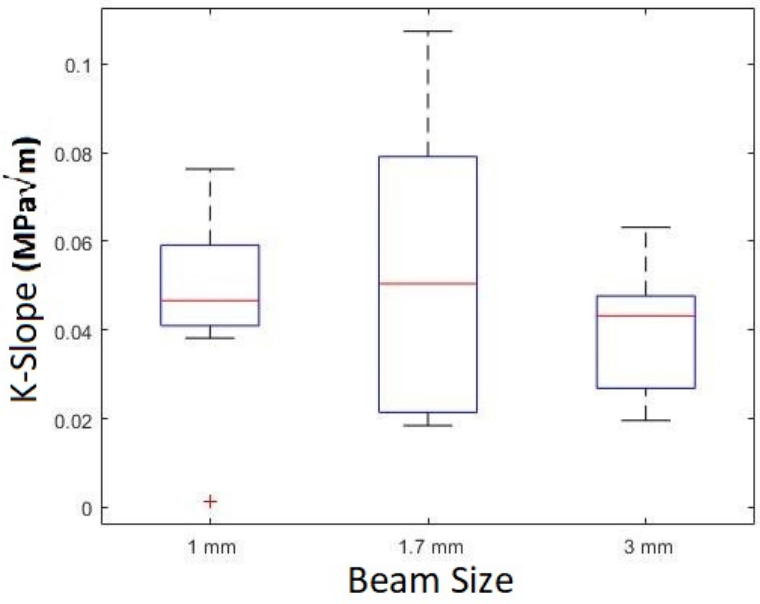

Figure 4.1: Boxplot K-Slope

A significant difference was detected in the mean values of K-Max for the three beam sizes (p-value=0.002). As shown in Figure 4.2, the mean K-Max of the 3 mm beams was significantly higher than that of the 1.7 mm (p=0.0377) and the 1 mm beams (p=0.001).

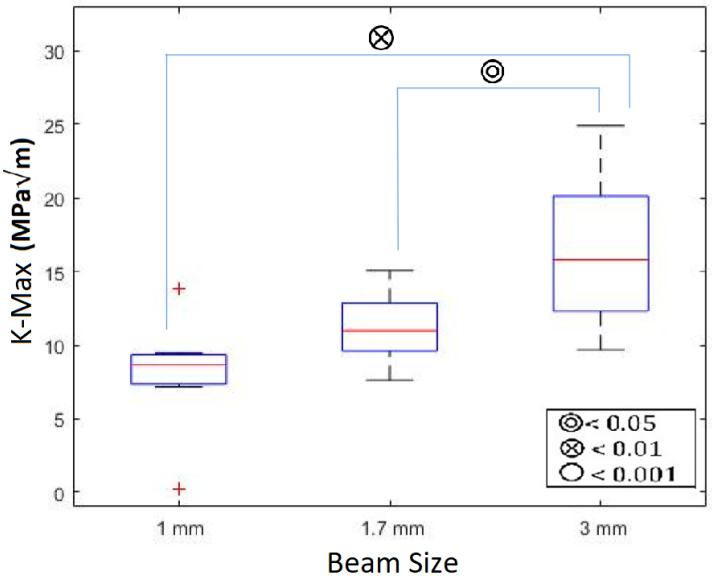

Figure 4.2: Boxplot of K-Max after removing outliers and with significant differences between beam sizes labelled in the legend

4.1.3 Fracture Energy properties

In this section, the results on J-Slope and J of bovine femur are presented. All of the above-mentioned mechanical properties were normally distributed. J-Slope for each beam size had equal variance. In contrast, the variance for each beam size of J was not equal. Hence, an ANOVA test was used to determine if any significant differences existed in the mean values of J-Slope while a Kruskal-Wallis Test was used for J. As shown in Figure 4.3, no significant difference was found in the means of J-Slope.

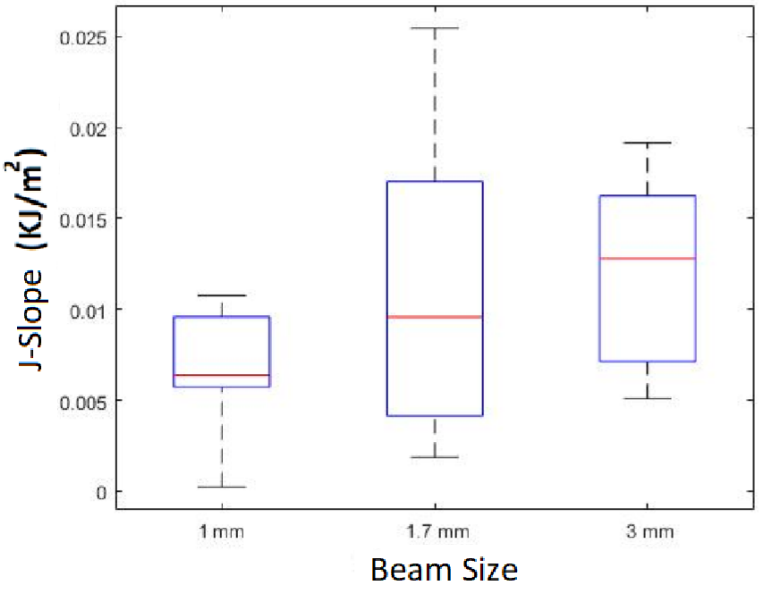

Figure 4.3: Boxplot J-Slope

However, significant differences were detected between the beam sizes for J. As shown in Figure 4.4, the mean J of the 3 mm beams was significantly higher than the 1.7 mm ($p=0.013$) and the 1 mm ($p<0.001$).

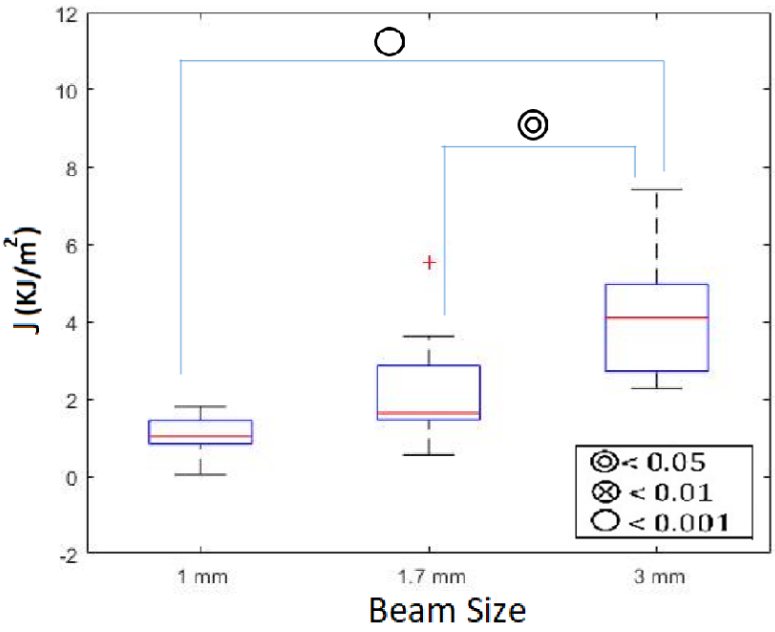

Figure 4.4: Boxplot J after removing outliers and with significant between beam sizes labelled in the legend

4.1.4 Elastic property

In this section, E was presented. The elastic property, E, for all beams was normally distributed. The variance for each beam size of E was not equal. No significant differences were found in E between the groups, see Figure 4.5. However, it should be mentioned that the values of elastic modulus were overestimated up to 200 GPa. Because of the correction factor of Equation 2.19 which was calculated for one-third of the specimen thickness as the notch length whereas, in this thesis, the notch length was measured half of the specimen thickness.

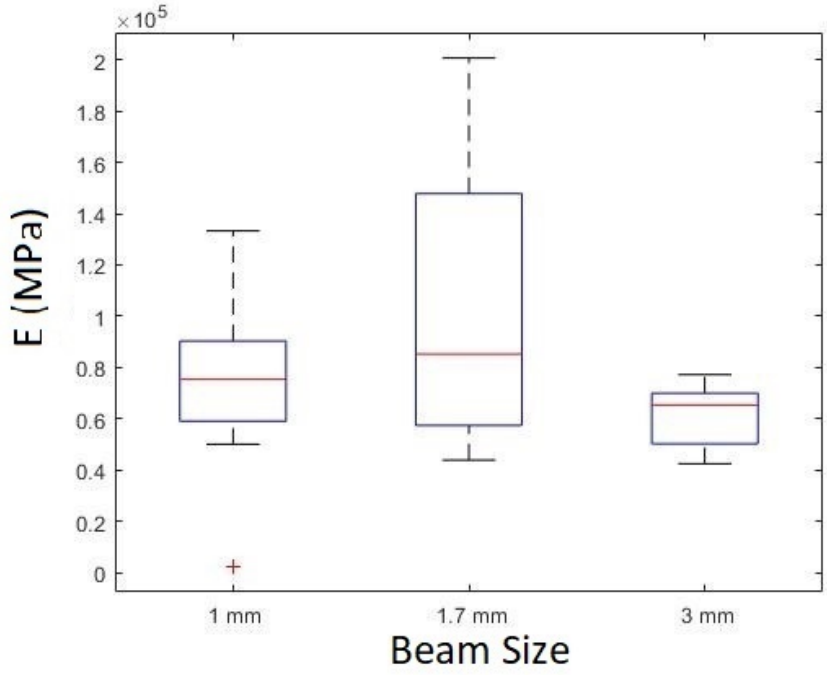

Figure 4.5: Boxplot E

4.2 Equine Bone

4.2.1 Introduction

In this section, the results on the fracture behaviour of equine cortical bone in different regions of the cortex of the femur are reported. This study was conducted in order to investigate anisotropy and variability in fracture resistance of femur midshaft cortical bone. The mechanical properties of midshaft, equine cortical bone from two femurs (ages 5 and 11 years) were determined under three-point bending test conditions. Specifically, this study was conducted to discover whether the beam size, age, or location influenced the fracture toughness, fracture energy or effective modulus. Detailed statistical summary tables for the equine cortical bone samples can be found in Appendix B.

4.2.2 MicroCT

As fracture behaviour may depend on porosity, all equine specimens were scanned with MicroCT. Thus no significant differences were found in the BV/TV of the different sized cortical specimens from different regions of the cortex between the old and young femurs (Figure 4.6, Figure 4.7, Figure 4.8). Beam size was also found to have no significant effect on the measured specimen BV/TV. Hence, the bone volume fraction of all equine specimens was considered to be equal.

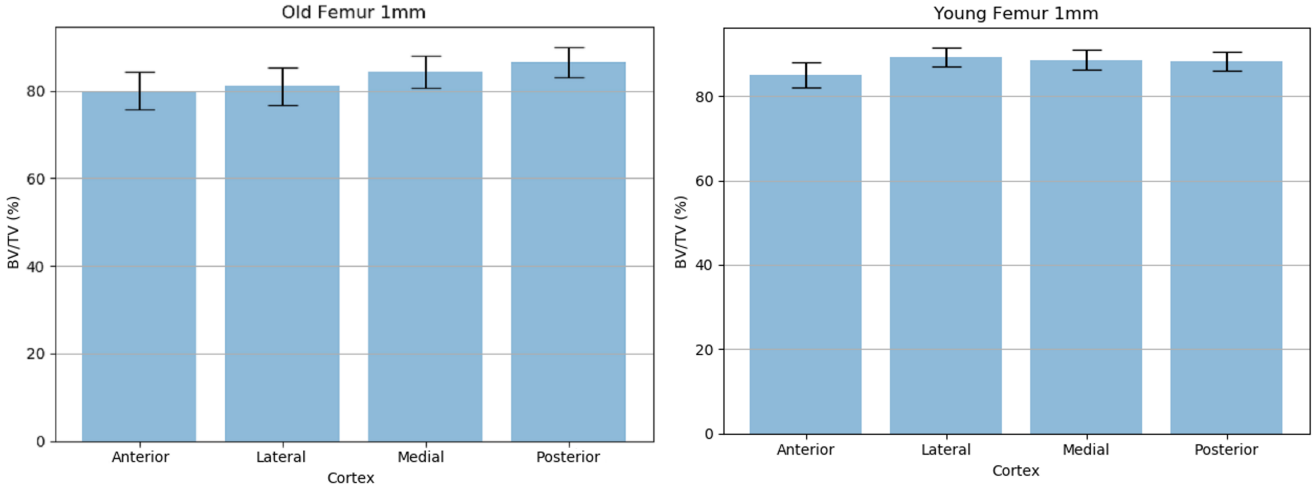

Figure 4.6: Comparison of the 1 mm specimen BV/TV, differentiated by anatomical location, between the old and young femurs

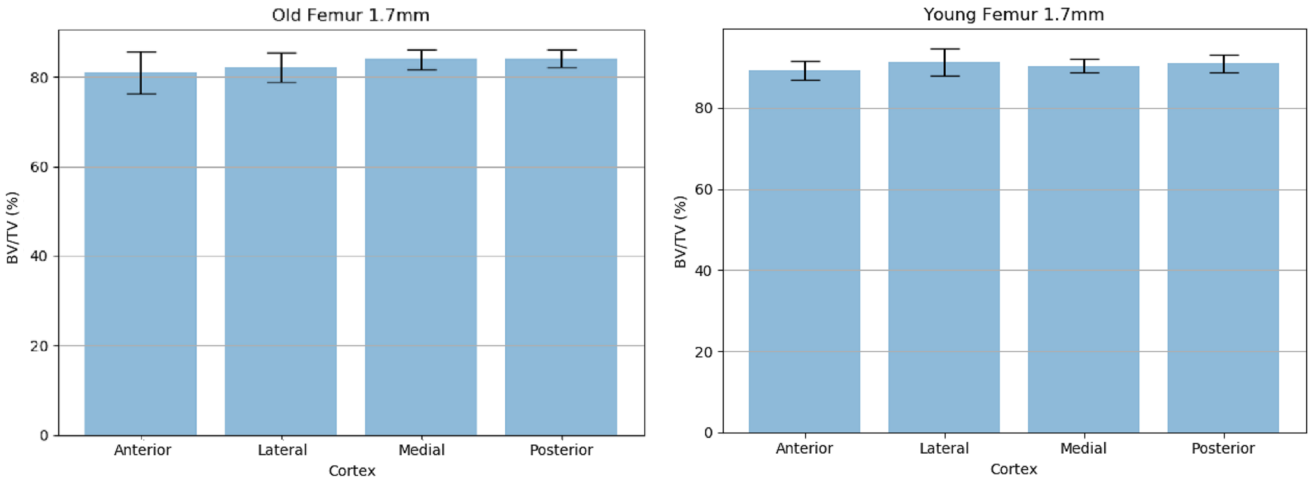

Figure 4.7: Comparison of the 1.7 mm specimen BV/TV, differentiated by anatomical location, between the old and young femurs

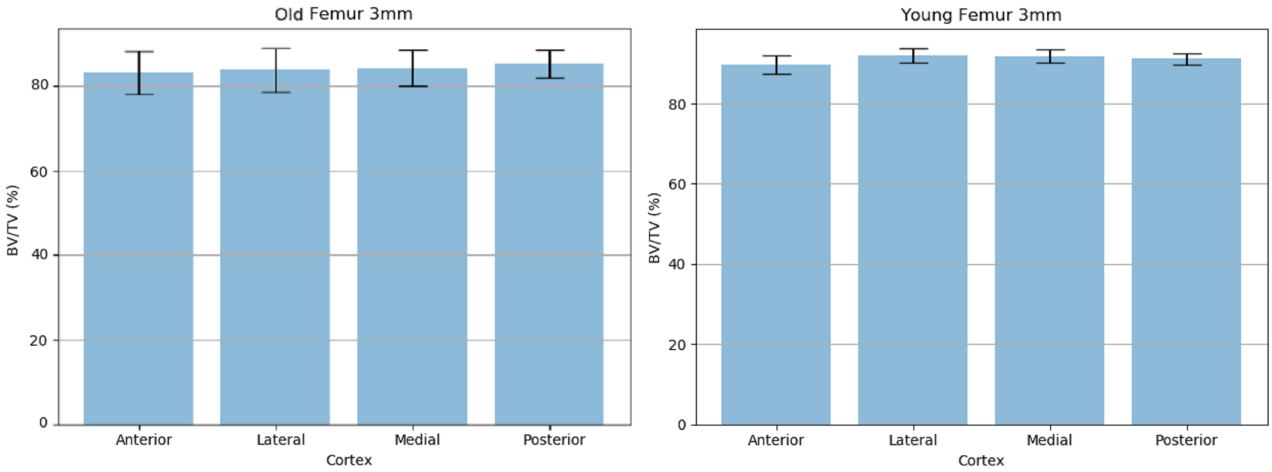

Figure 4.8: Comparison of the 3 mm specimen BV/TV, differentiated by anatomical location, between the old and young femurs

4.2.3 Fracture Toughness properties

In this section, the results on K-Slope and K-Max of four anatomical areas (Anterior, Lateral, Medial, and Posterior) from old (11 years) and young (5 years) equine femurs are presented.

Old Equine Femur (11-year-old):

- **K-Slope:**

  K-Slope was normally distributed only in the anterior cortex. For the other cortices some outliers were found and removed, then K-Slope became normally distributed. As seen in Figure 4.9, no significant difference was found in the mean of K-Slope for any beam size in all cortices except in the medial cortex where the mean K-Slope of the 3 mm beams was significantly lower than the 1 mm beams(p=0.011).

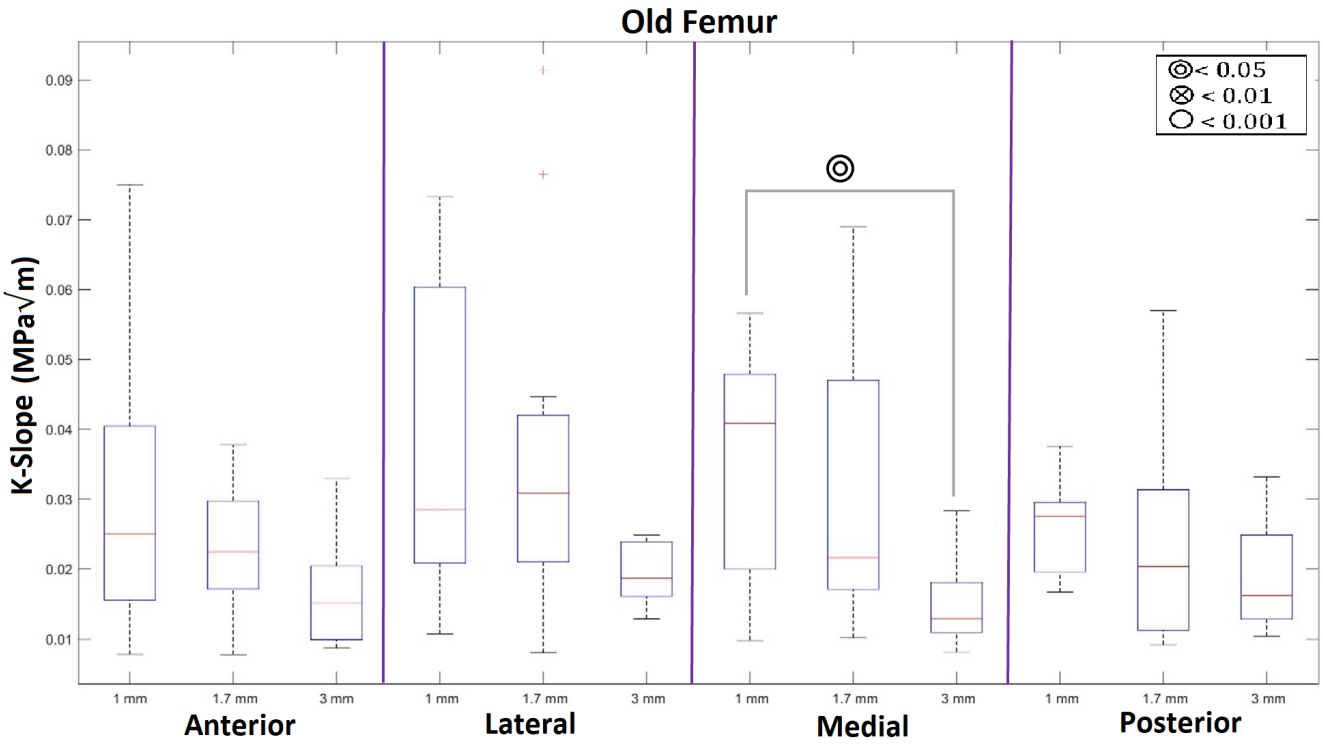

Figure 4.9: Boxplot K-Slope for old femur (11-year-old) with significant between beam sizes labelled in the legend

- **K-Max:**

  K-Max was normally distributed only in the anterior cortex. For the other cortices some outliers were found and removed, then K-Max became normally distributed. As seen in Figure 4.10, no significant difference was found in the mean of K-Max for any beam size in the lateral and medial cortices. On the other hand, in the anterior cortex, the mean K-Max of the 1 mm beams was significantly lower than that of the 3 mm (p=0.011) and the of 1.7 mm beams (p=0.016). Additionally, in the posterior cortex, the mean K-Max of the 3 mm beams was significantly higher than that of the 1.7 mm (p=0.03) and the of 1 mm beams (p=0.009).

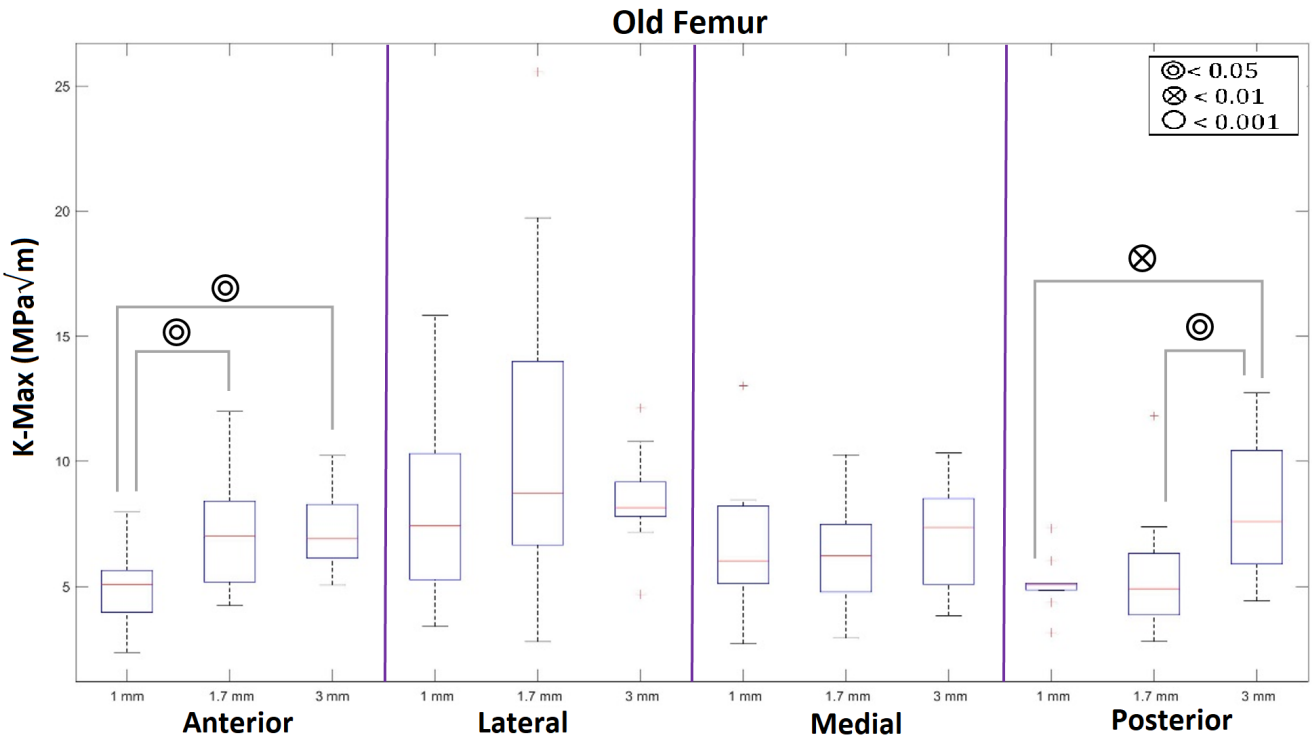

Figure 4.10: Boxplot K-Max for old femur (11-year-old) with significant between beam sizes labelled in the legend

Young Equine Femur (5-year-old):

- **K-Slope:**

  K-Slope was not normally distributed for some beam sizes in all cortices. Therefore, some outliers were found and removed, then K-Slope became normally distributed. As seen in Figure 4.11, no significant difference was found in the mean of K-Slope for any beam size in the anterior and lateral cortices. Although, in the medial and posterior cortices, the mean K-Slope of the 3 mm beams was significantly lower than the 1 mm beams (p=0.026) and (p=0.003), respectively.

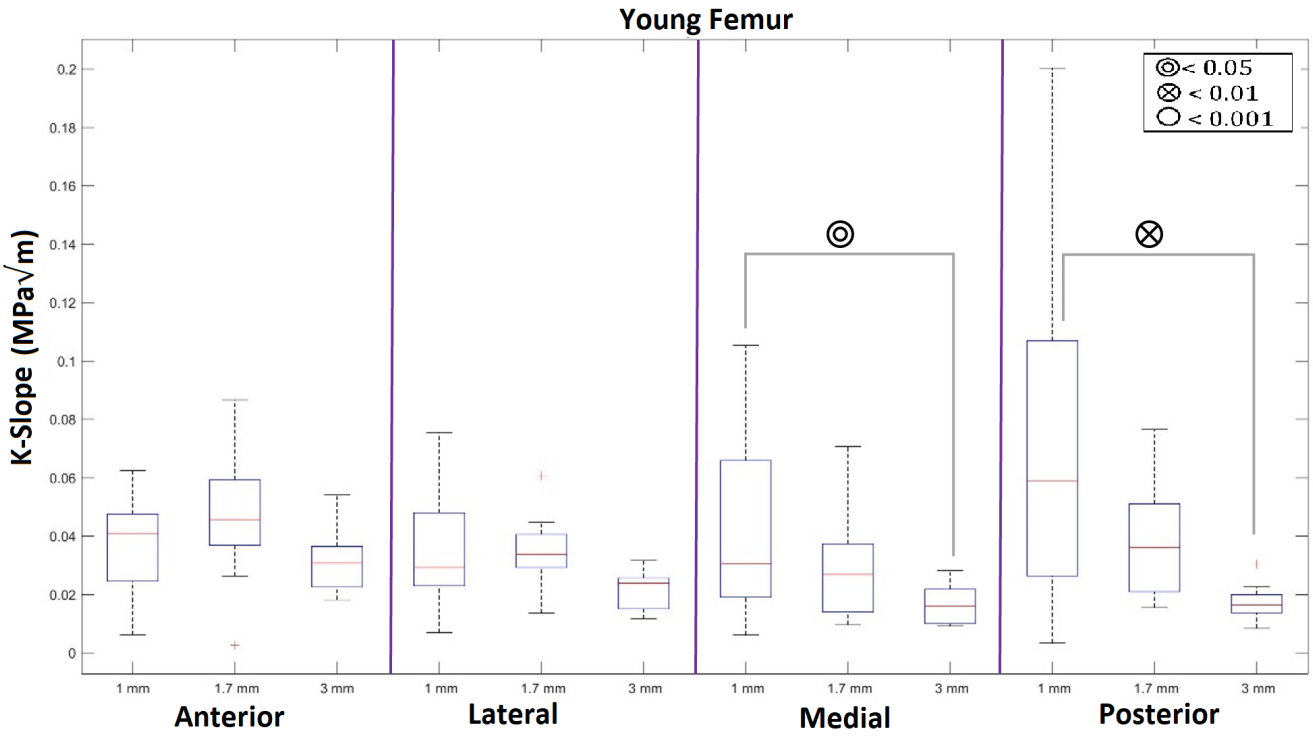

Figure 4.11: Boxplot K-Slope for young femur (5-year-old) with significant between beam sizes labelled in the legend

- **K-Max:**

  K-Max was normally distributed in all cortices except in the lateral cortex for 3 mm beam size. For the lateral cortex one outlier was found and removed, then K-Max became normally distributed. As seen in Figure 4.12, no significant difference was found in the mean of K-Max for any beam size in the posterior cortex. Although, in the anterior cortex, the mean K-Max of the 1 mm beams was significantly lower than that of the 1.7 mm ($p=0.007$) and the 3 mm beams ($p<0.001$). In the lateral cortex, the mean K-Max of the 1.7 mm beams was significantly higher than that of the 1 mm ($p<0.001$) and the 3 mm beam ($p=0.02$) while the mean K-Max of the 3 mm beams was higher than the 1 mm beam ($p=0.022$). Additionally, in the medial cortex, the mean K-Max of the 3 mm beam was significantly higher than the 1 mm beam ($p=0.049$).

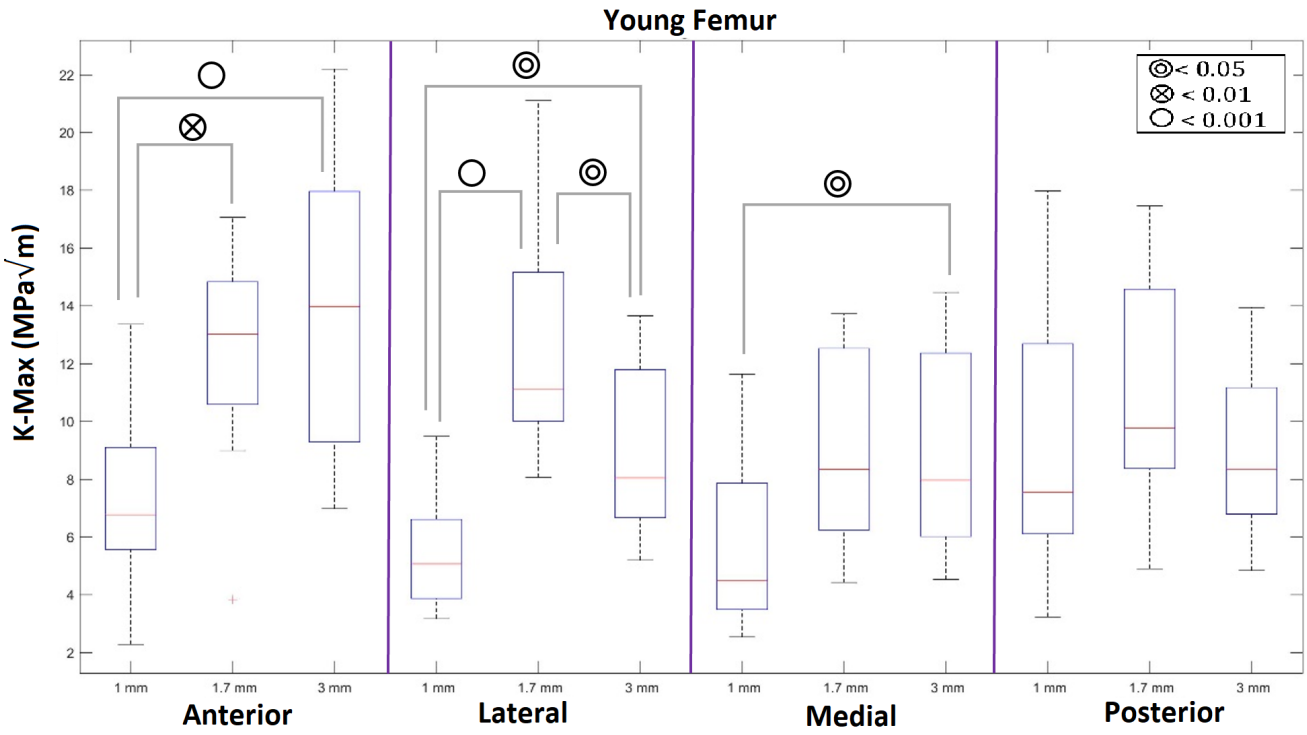

Figure 4.12: Boxplot K-Max for young femur (5-year-old) with significant between beam sizes labelled in the legend

4.2.4 Fracture Energy properties

In this section, the results on J-Slope and J of four anatomical areas (Anterior, Lateral, Medial, and Posterior) from old (11 years) and young (5 years) equine femurs are presented.

Old Equine Femur (11-year-old)

- **J-Slope:**

  J-Slope was normally distributed in all cortices except in the posterior cortex for 1 mm beam size. For the posterior cortex a few outliers were found and removed, then J-Slope became normally distributed. As seen in Figure 4.13, no significant difference was found in the means of J-Slope for the three beam sizes in all cortices.

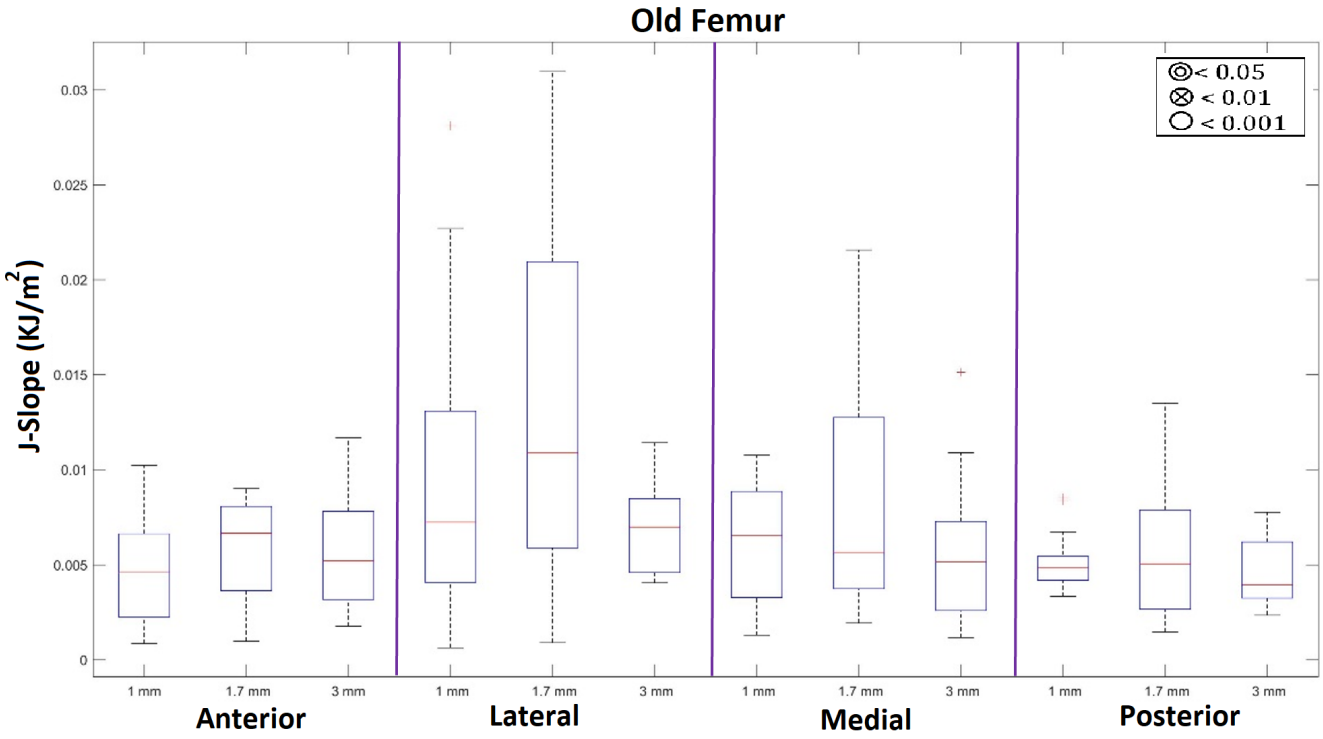

Figure 4.13: Boxplot J-Slope for old femur (11-year-old) with significant between beam sizes labelled in the legend

- **J:**

J was normally distributed in all cortices except in the posterior cortex for 3 mm beam size. For the posterior cortex, one outlier was found and removed. Afterwards, J became normally distributed. As shown in Figure 4.14, in the medial cortex, no significant difference was found in the means of J for any beam size. On the other hand, in the anterior cortex, the mean J of the 1 mm beams was significantly lower than that of the 1.7 mm ($p=0.004$) and the 3 mm beams ($p<0.001$). In the lateral cortex, the mean of the 1.7 mm beams was significantly higher than the 1 mm beams ($p=0.012$). Finally, in the posterior cortex, the mean J of the 3 mm beams was significantly higher than the 1 mm ($p=0.007$).

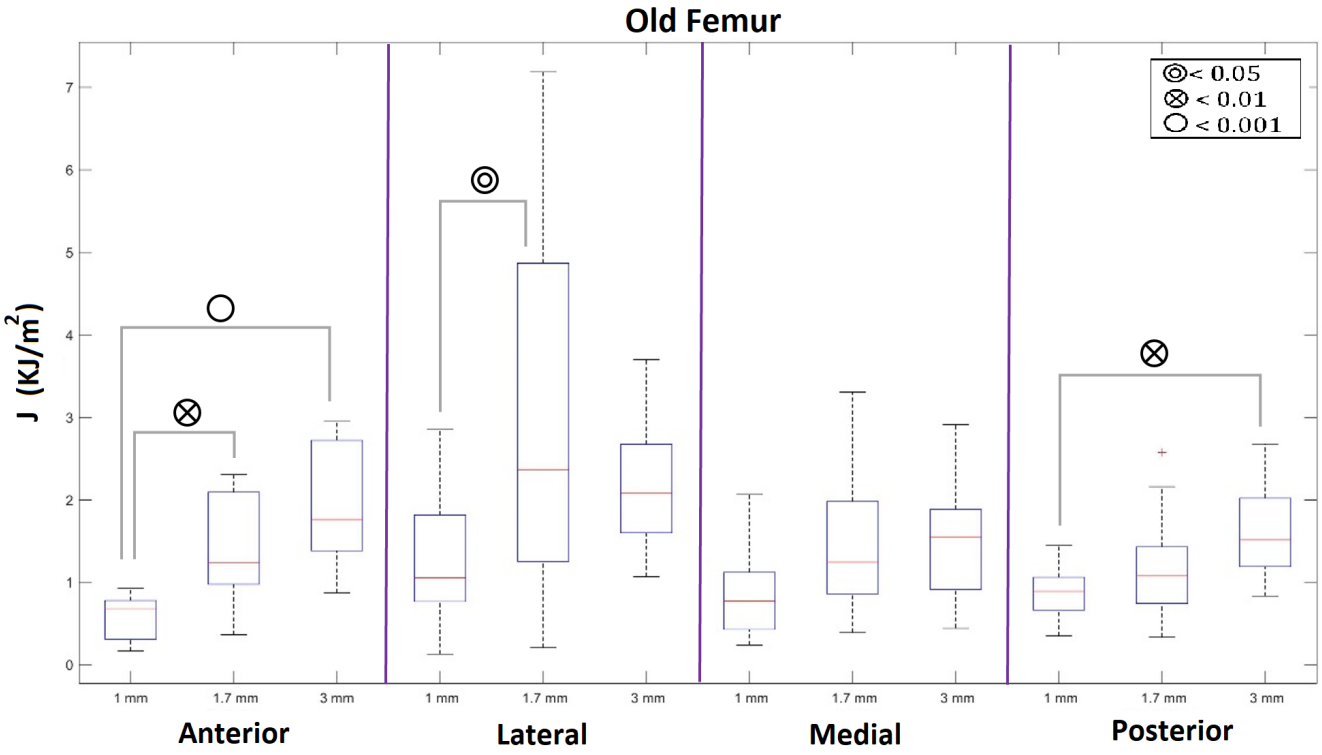

Figure 4.14: Boxplot J for old femur (11-year-old) with significant between beam sizes labelled in the legend

Young Equine Femur (5-year-old)

- **J-Slope:**

  J-Slope was normally distributed only in the anterior cortex. For the other cortices some outliers were found and removed, then J-Slope became normally distributed. As seen in Figure 4.15, no significant difference was found in the means of J-Slope for any beam size in the medial and posterior cortices. Although, in the anterior cortex the mean J-Slope of the 1.7 mm beams was significantly higher than the 1 mm beams (p=0.0495), and in the lateral cortex the mean J-Slope of the 1.7 mm beams was significantly higher than the 3 mm beams (p=0.004).

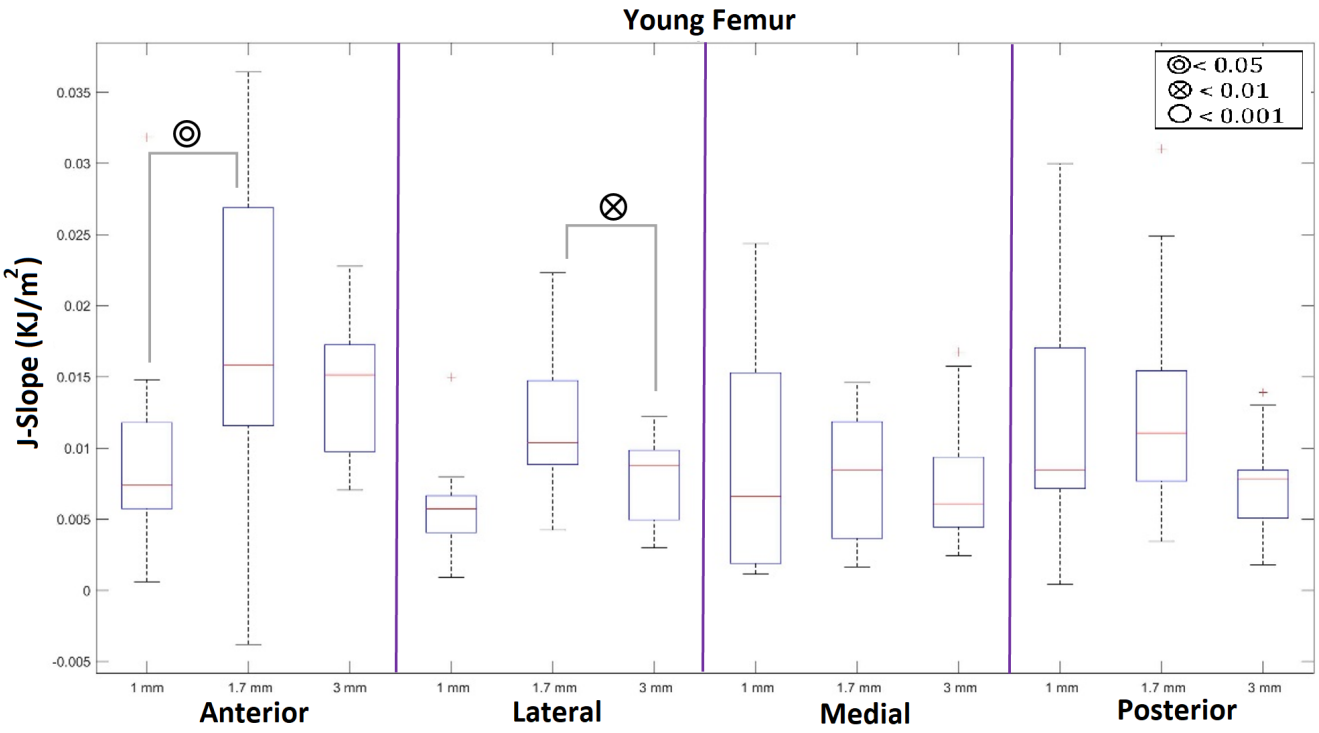

Figure 4.15: Boxplot J-Slope for young femur (5-year-old) with significant between beam sizes labelled in the legend

- **J:**

  J was normally distributed in all cortices except in the medial cortex for 1 mm beam size. For the medial cortex, some outliers were found and removed. Afterwards, J became normally distributed. As shown in Figure 4.16, the significant difference was observed in the means of J for each beam size in all cortices. In the anterior cortex, the mean J of the 1 mm beams was significantly lower than that of the 1.7 mm beams ($p<0.001$) and the 3 mm beams ($p<0.001$). In the lateral cortex, the mean J of the 1 mm beams was significantly lower than that of the 1.7 mm beams ($p=0.013$) and the 3 mm beams ($p<0.001$). In the medial cortex, the mean J of the 1 mm beams was significantly lower than that of the 1.7 mm beams ($p=0.024$) and the 3 mm beams ($p=0.002$). Finally, in the posterior cortex, the mean J of the 1 mm beams was significantly lower than the 1.7 mm beams ($p=0.049$).

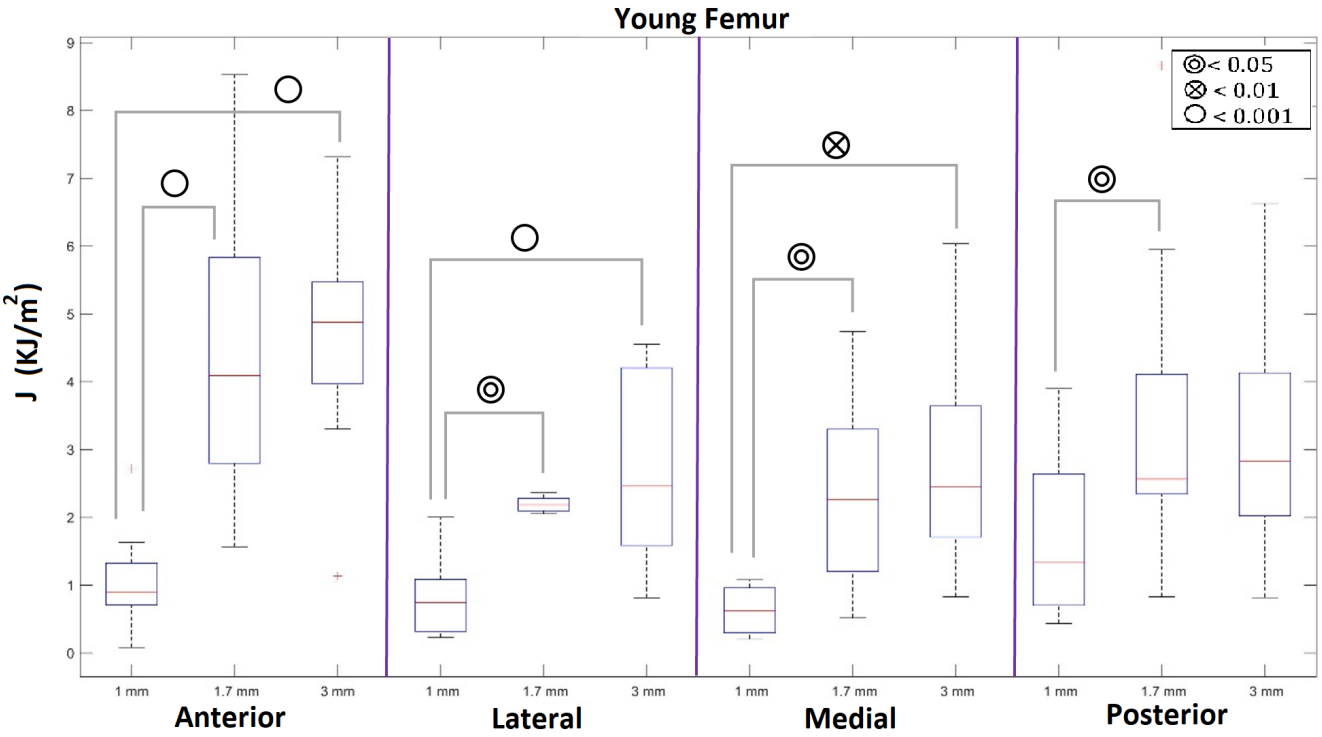

Figure 4.16: Boxplot J for young femur (5-year-old) with significant between beam sizes labelled in the legend

4.2.5 Elastic property

In this section, the results on E of four anatomical areas (Anterior, Lateral, Medial, and Posterior) from old (11 years) and young (5 years) equine femurs are presented.

Old Equine Femur (11-year-old)

- **E:**

  The elastic modulus, E, was not normally distributed in all cortices. Some outliers were found and removed. Afterwards, E became normally distributed. As seen in Figure 4.17, in the posterior cortex, no significant difference was found in the means of E for any beam size. Although, in the anterior cortex, the mean E of the 3 mm beams was significantly lower than that of the 1.7 mm (p=0.031) and the 1 mm beams (p=0.017). In the lateral cortex, the mean E of the 3 mm beams was significantly lower than the 1 mm (p=0.006). Finally, in the medial cortex, the mean E of the 1 mm beams was significantly higher than

that of the 1.7 mm (p<0.001) and the 3 mm beams (p<0.001).

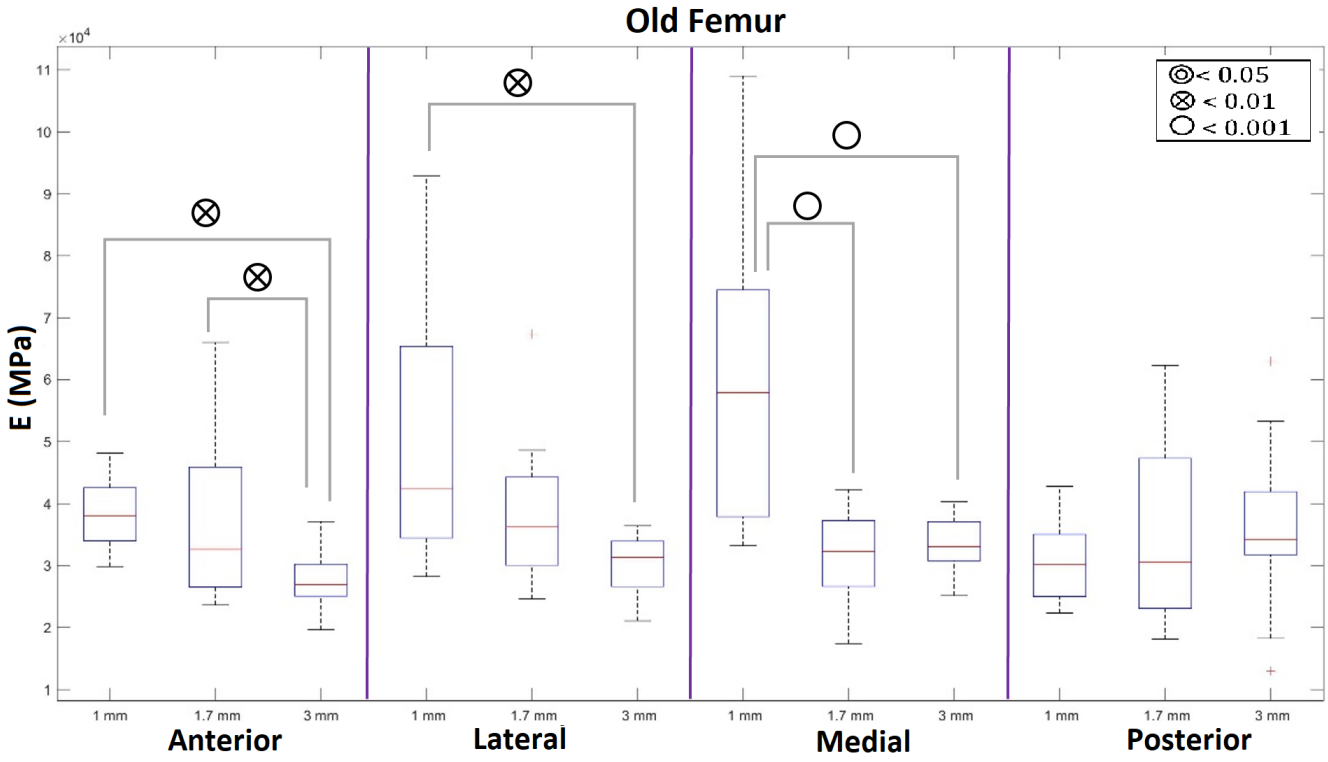

Figure 4.17: Boxplot E(MPa) for old femur (11-year-old) with significant between beam sizes labelled in the legend

Young Equine Femur (5-year-old)

- **E:**

  The elastic modulus, E, was normally distributed only in the medial cortex. In the other cortices, some outliers were found and removed. Afterwards, E became normally distributed. As seen in Figure 4.18, the significant difference was detected in the mean values of E in all cortices. In the anterior cortex, the mean E of the 3 mm beams was significantly lower than that of the 1.7 mm beams (p=0.013) and the 1 mm beams (p<0.001). In the lateral cortex, the mean E of the 3 mm beams was significantly lower than that of the 1.7 mm beams (p=0.003) and the 1 mm beams (p=0.009). In the medial cortex, the mean E of the 3 mm beams was significantly lower than that of the 1 mm beams (p=0.002). Finally, in the posterior cortex, the mean E of the 1 mm beams was significantly higher than that of the 1.7 mm beams (p=0.043) and the 3 mm beams (p=0.001).

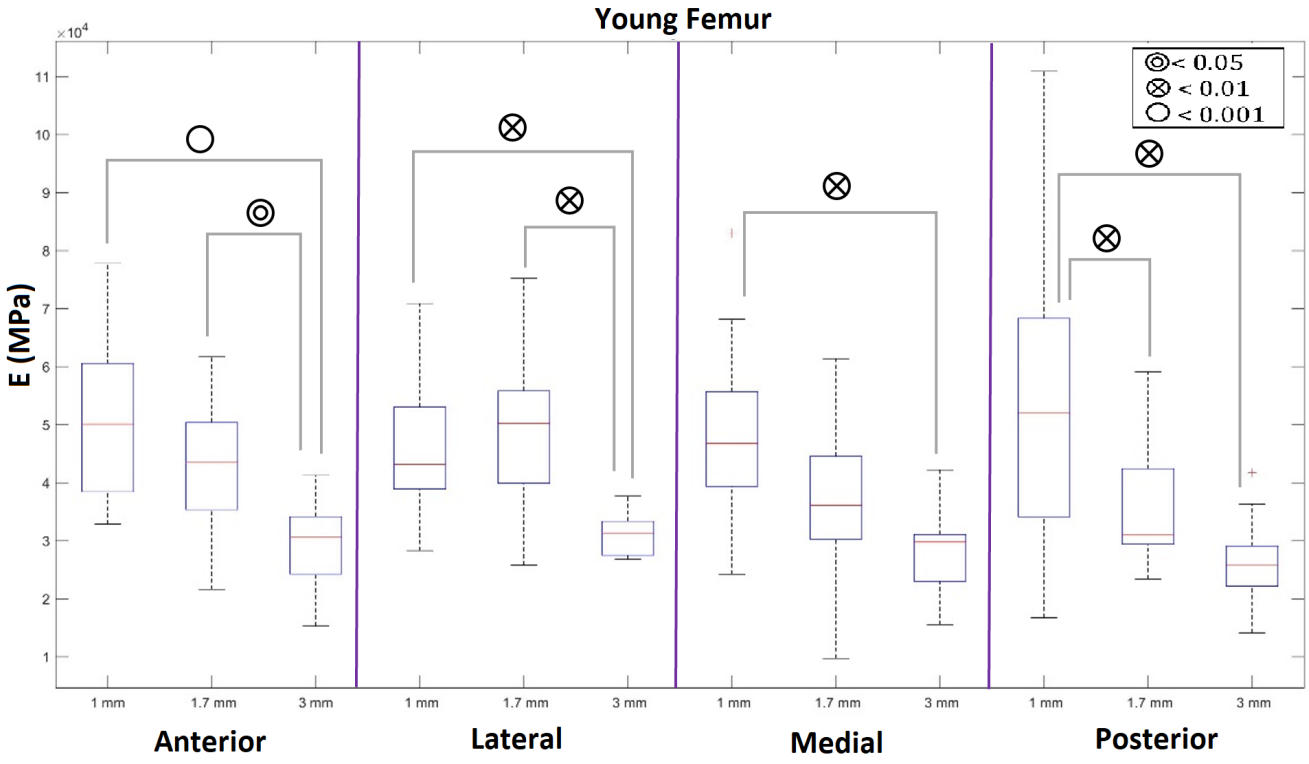

Figure 4.18: Boxplot E(MPa) for young femur (5-year-old) with significant between beam sizes labelled in the legend

4.2.6 Age Comparison

In this section, the age comparison results on K-Slope, K-Max, J-Slope, J, and E for the 3 mm and 1 mm beam sizes of four anatomical areas (Anterior, Lateral, Medial, and Posterior) from old (11 years) and young (5 years) equine femurs are presented. Additionally, the age comparison results on K-Initial and the 1.7 mm beam size can be found in Appendix B.

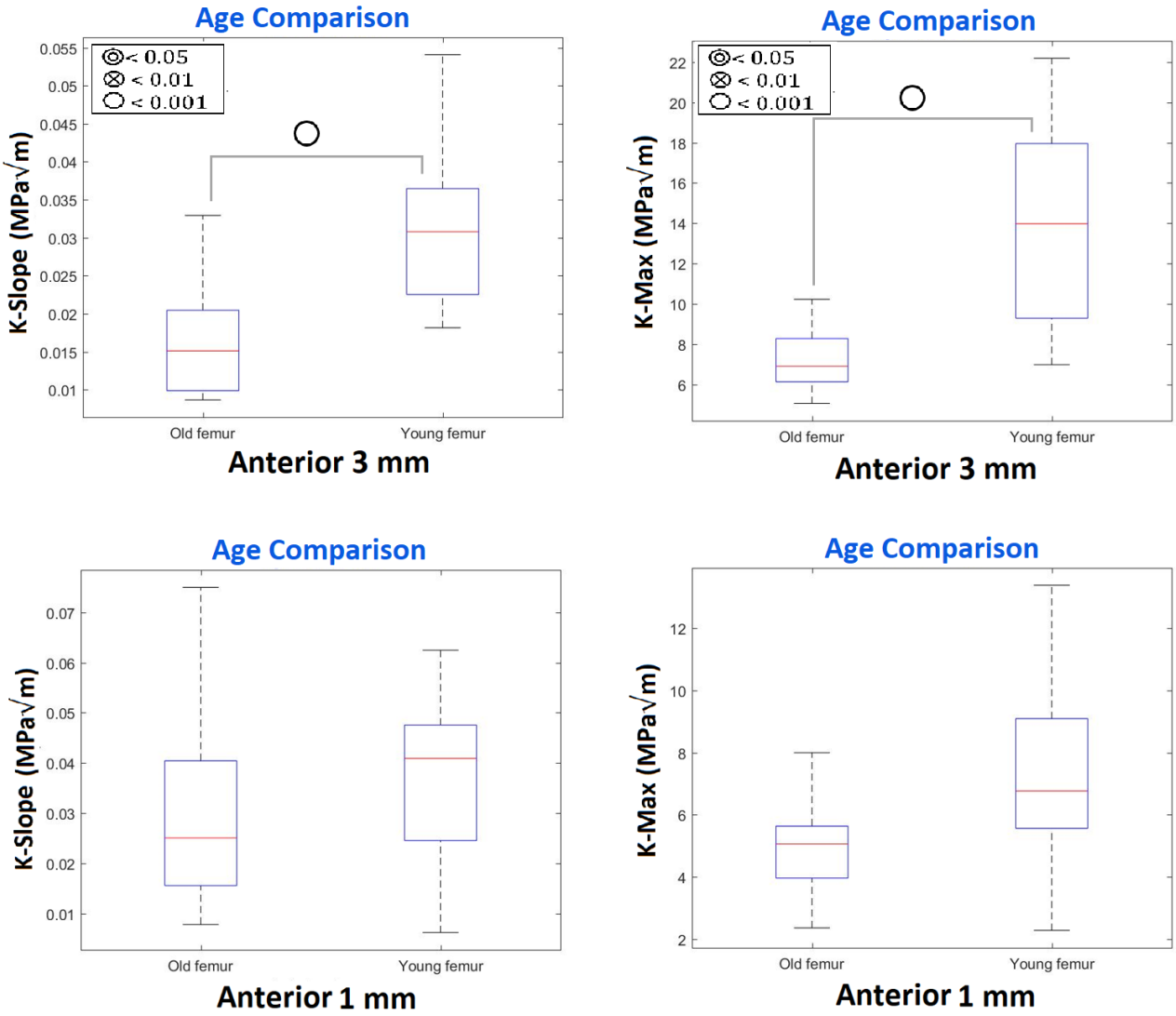

Figure 4.19: Age comparison of K-Slope and K-Max in the anterior of beam size 3 mm and 1 mm

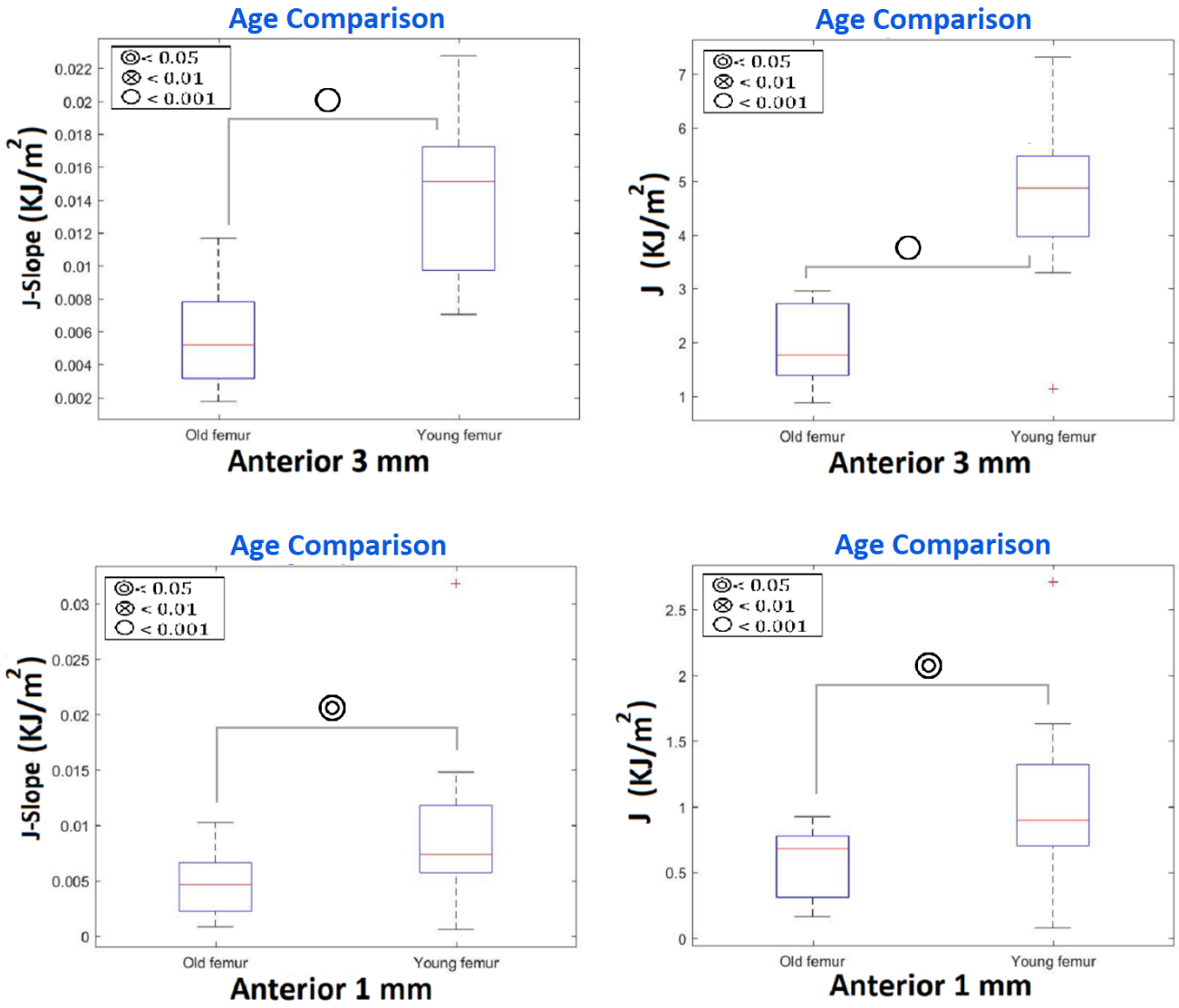

Figure 4.20: Age comparison of J-Slope and J in the anterior of beam size 3 mm and 1 mm

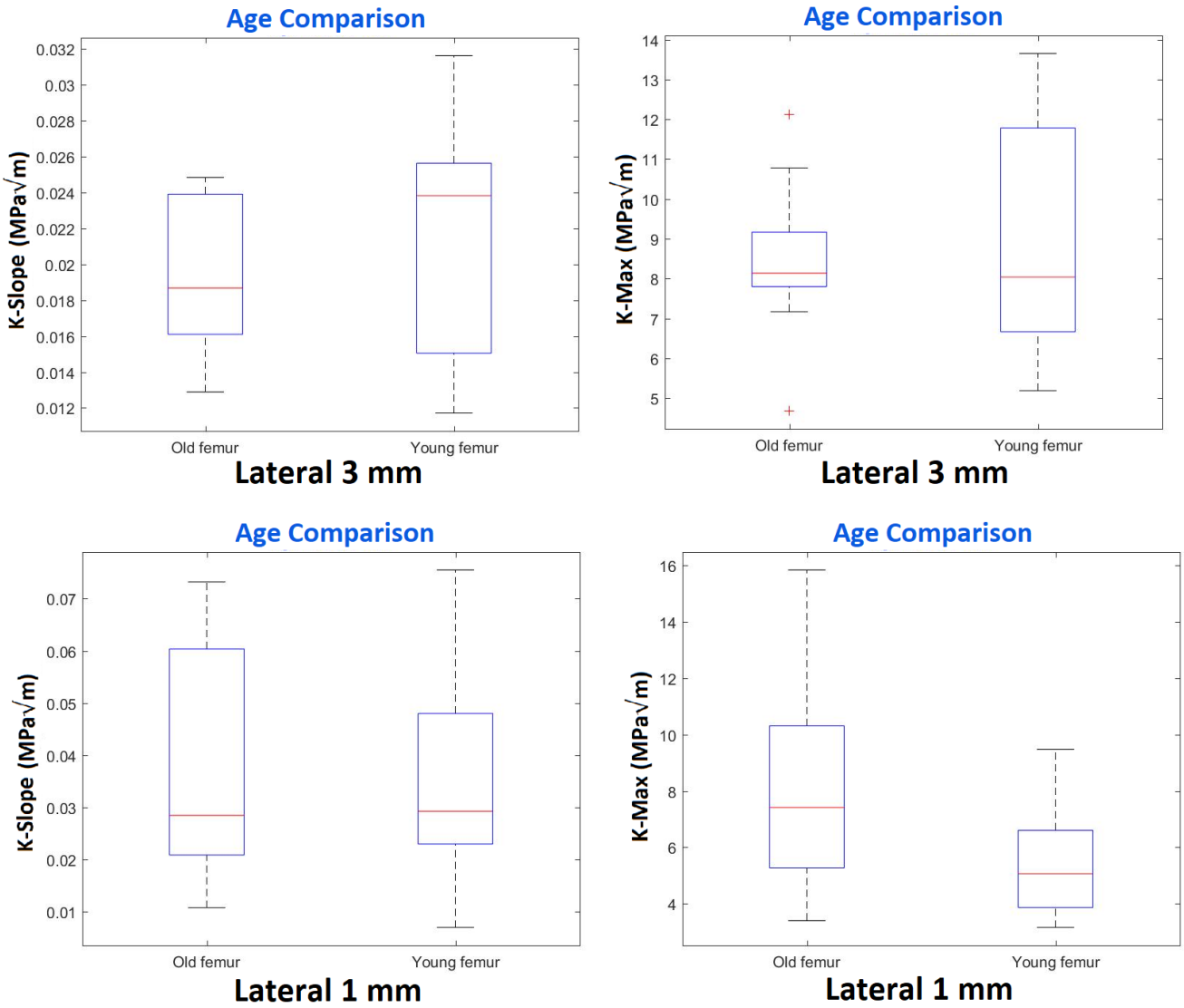

Figure 4.21: Age comparison of K-Slope and K-Max in the lateral of beam size 3 mm and 1 mm

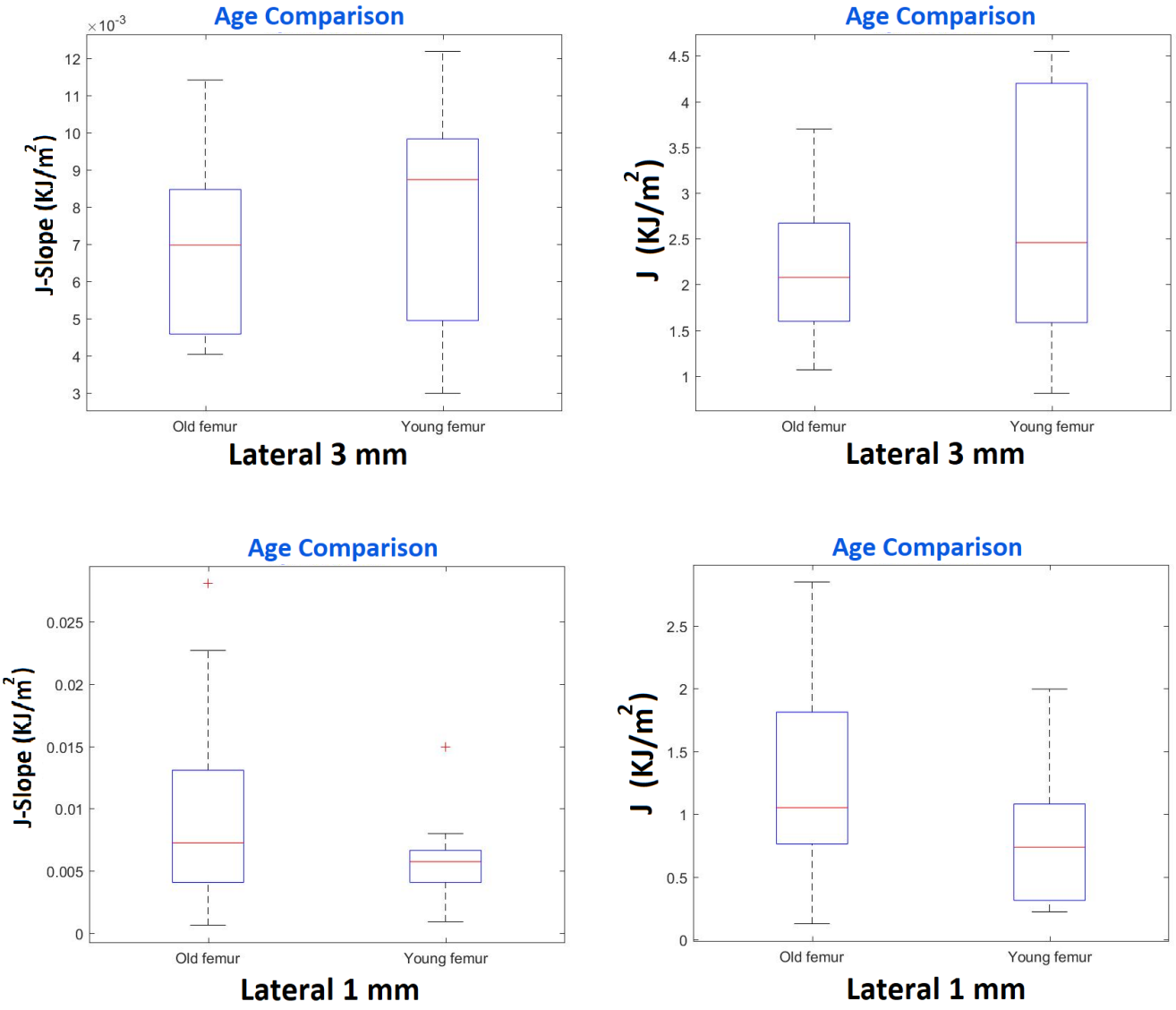

Figure 4.22: Age comparison of J-Slope and J in the lateral of beam size 3 mm and 1 mm

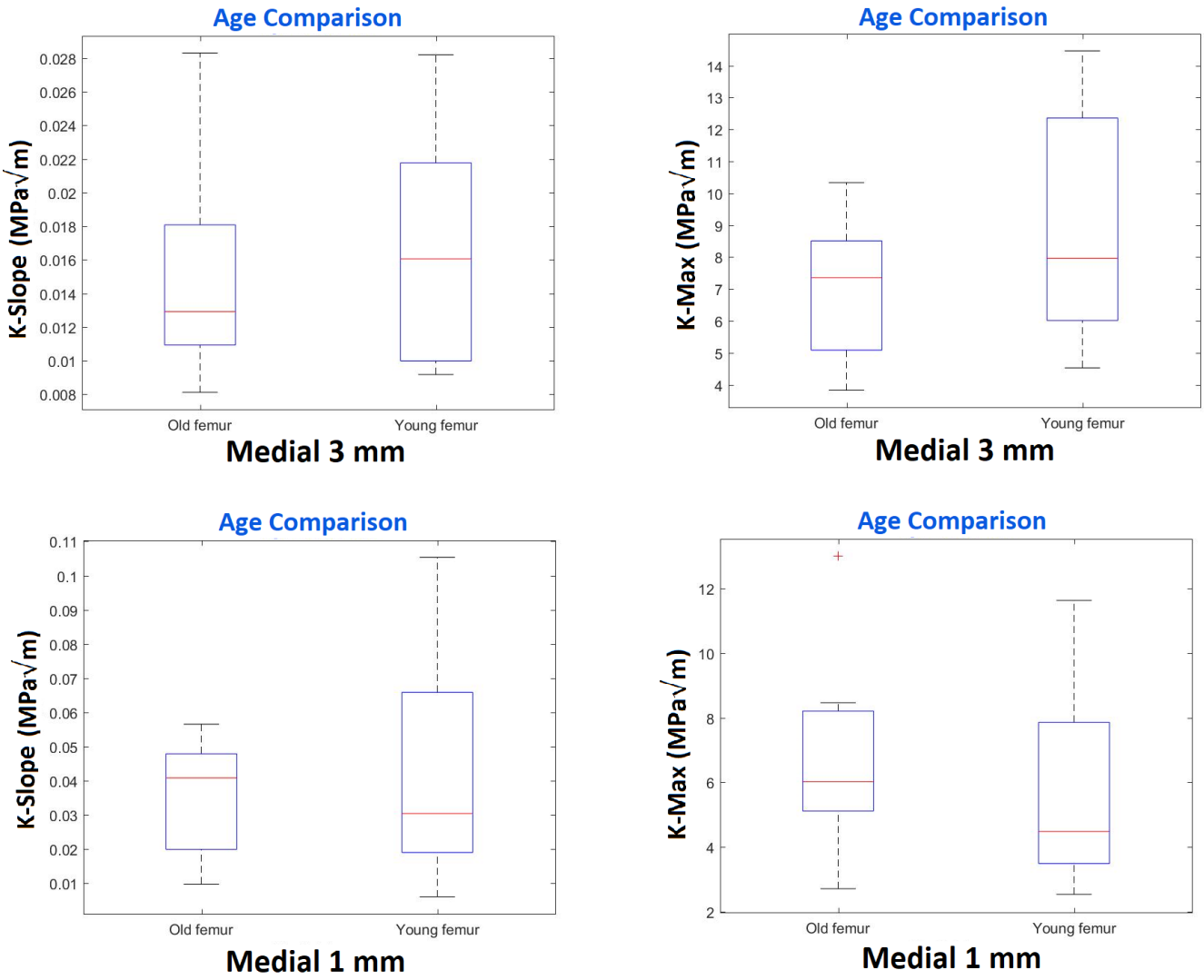

Figure 4.23: Age comparison of K-Slope and K-Max in the medial of beam size 3 mm and 1 mm

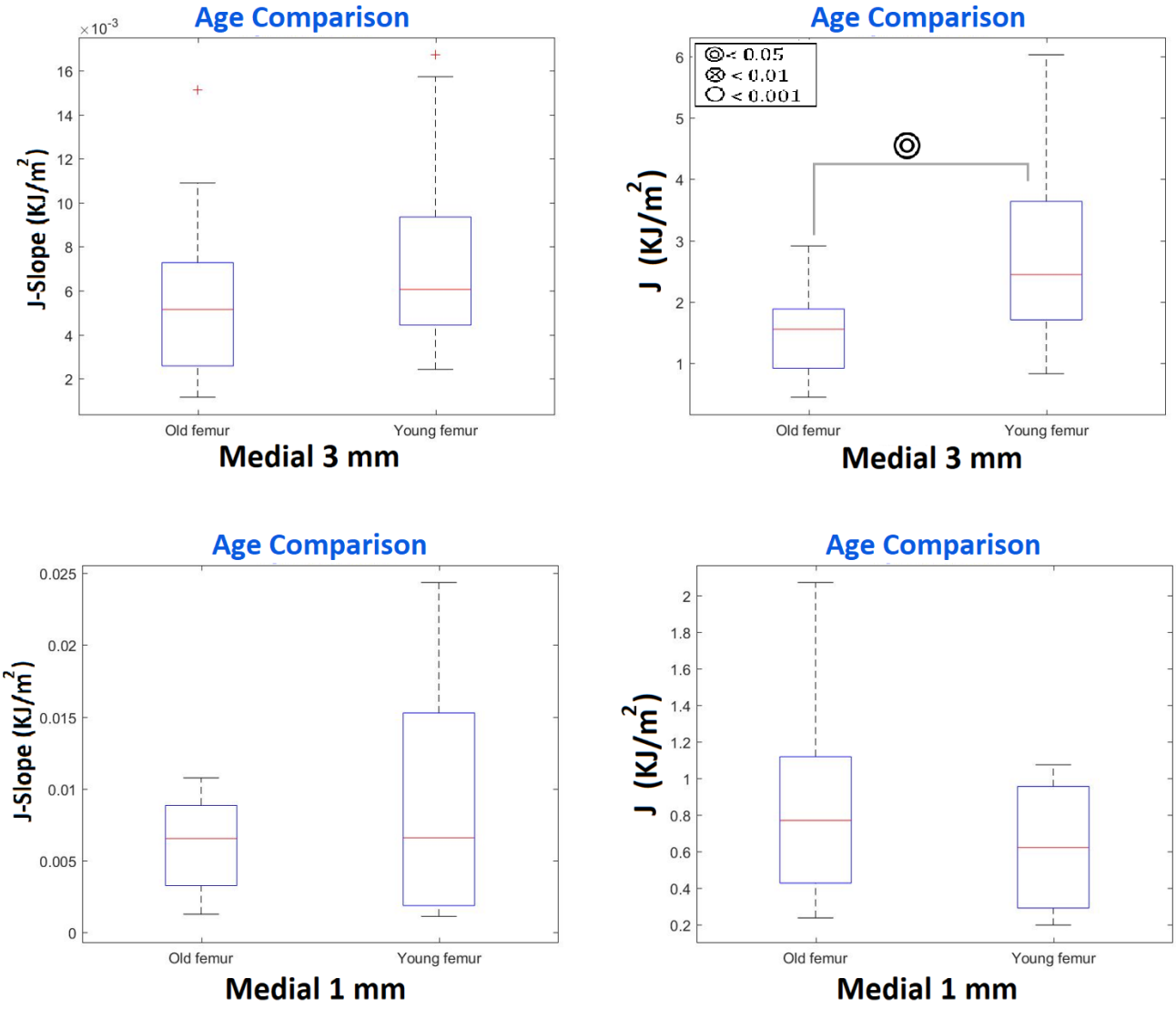

Figure 4.24: Age comparison of J-Slope and J in the medial of beam size 3 mm and 1 mm

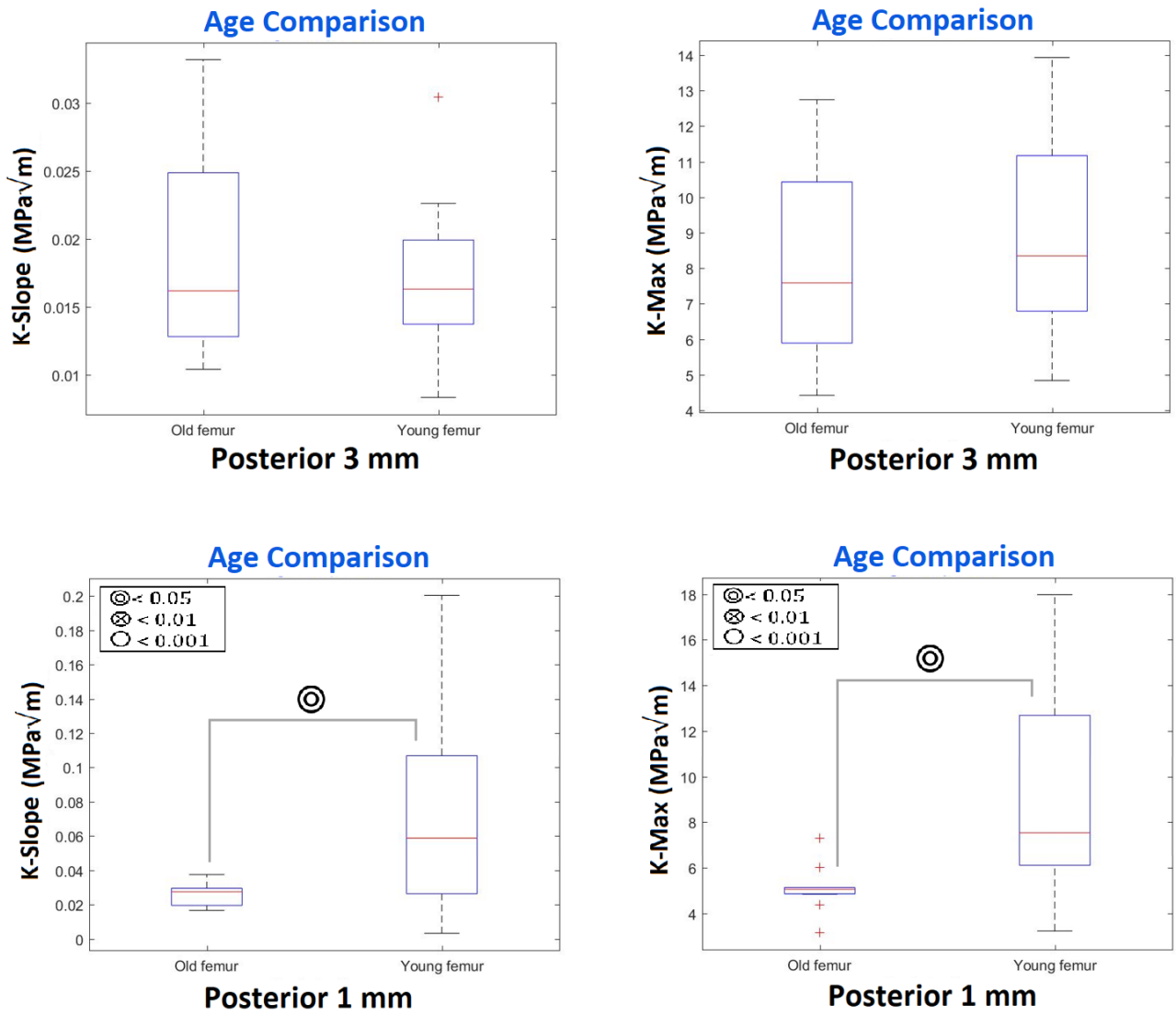

Figure 4.25: Age comparison of K-Slope and K-Max in the posterior of beam size 3 mm and 1 mm

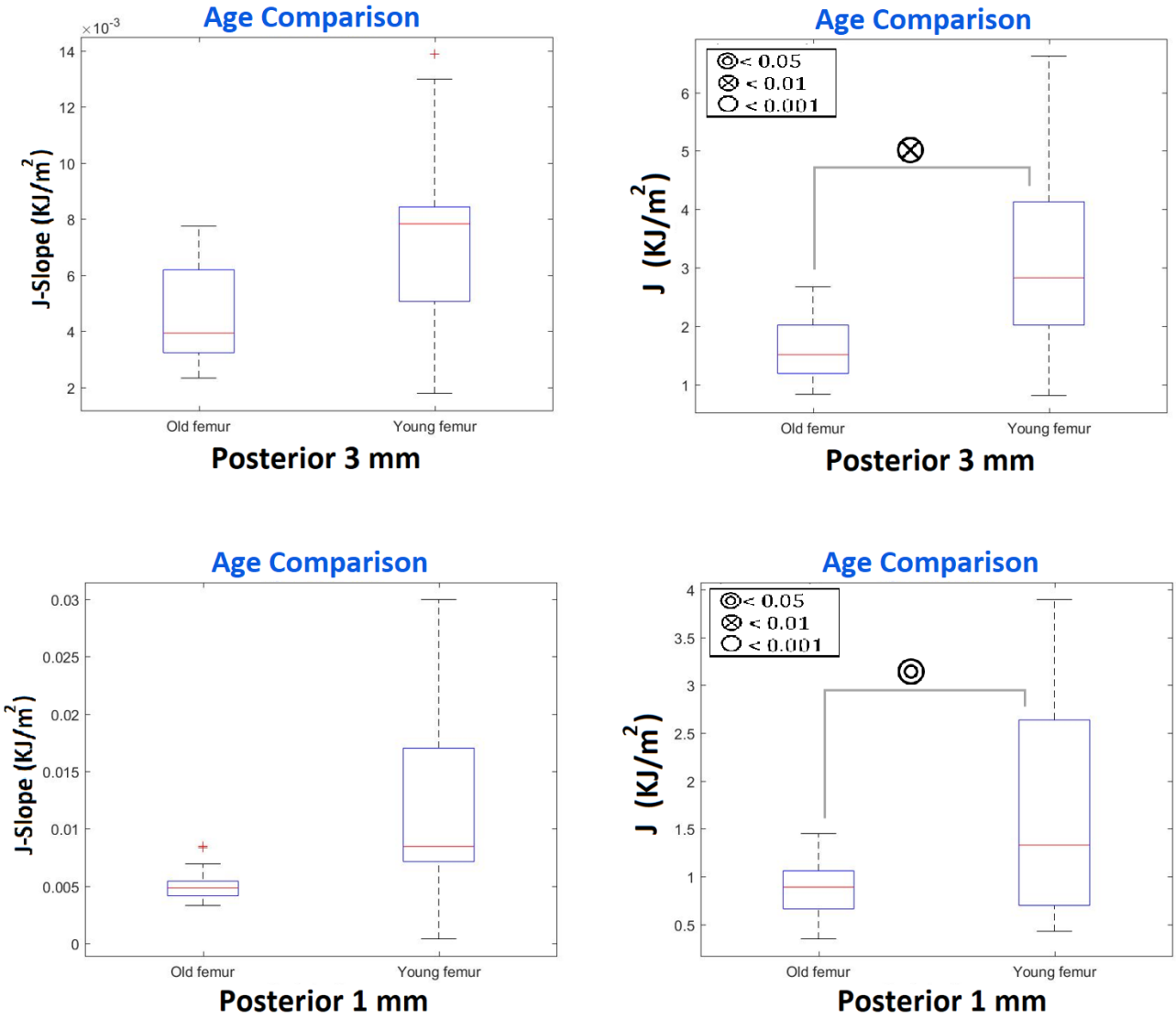

Figure 4.26: Age comparison of J-Slope and J in the posterior of beam size 3 mm and 1 mm

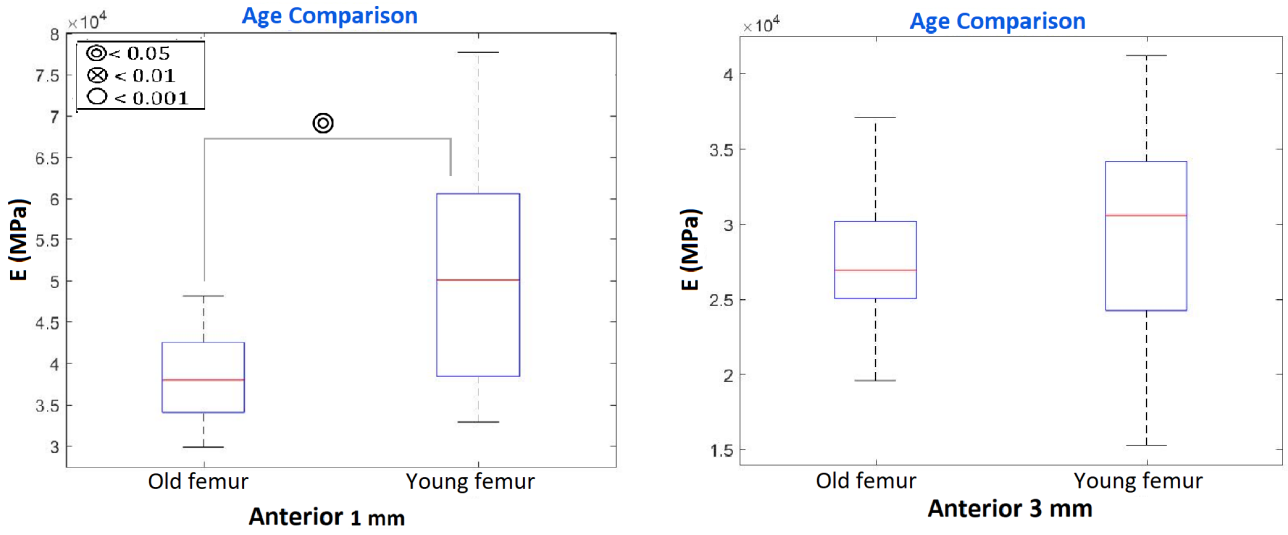

Figure 4.27: Age comparison of E in the anterior cortex of beam size 3 mm and 1 mm

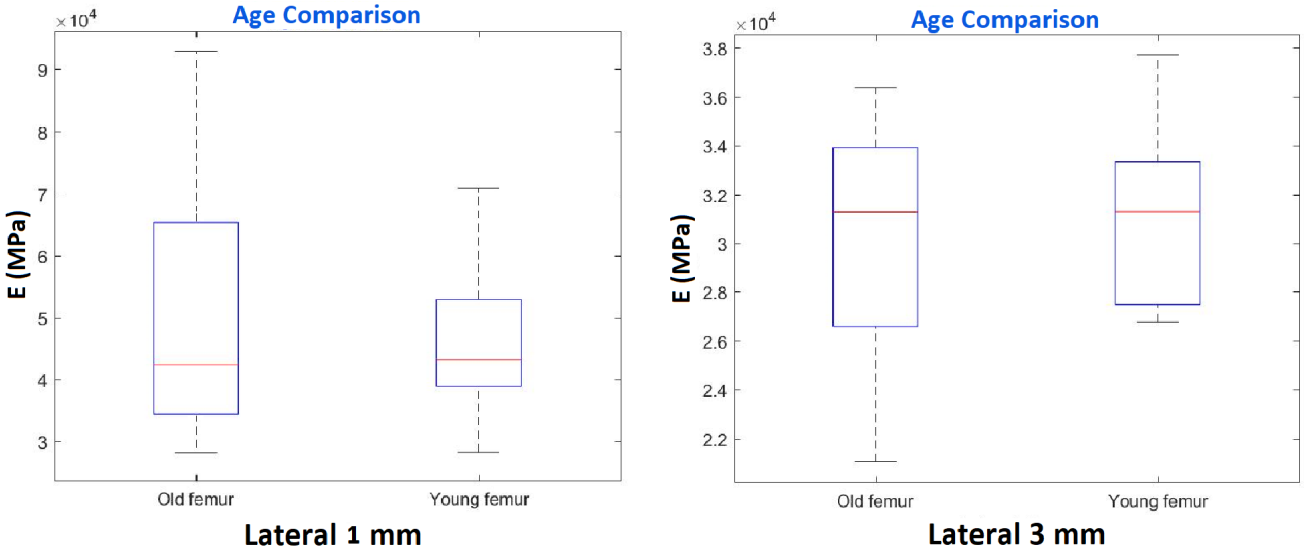

Figure 4.28: Age comparison of E in the lateral cortex of beam size 3 mm and 1 mm

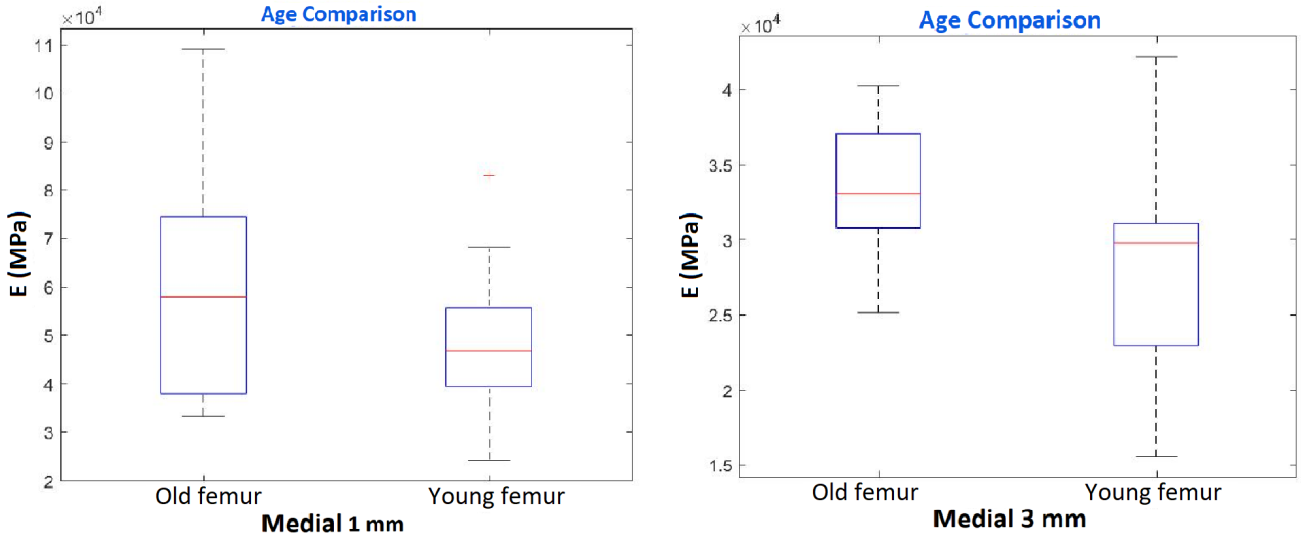

Figure 4.29: Age comparison of E in the medial cortex of beam size 3 mm and 1 mm

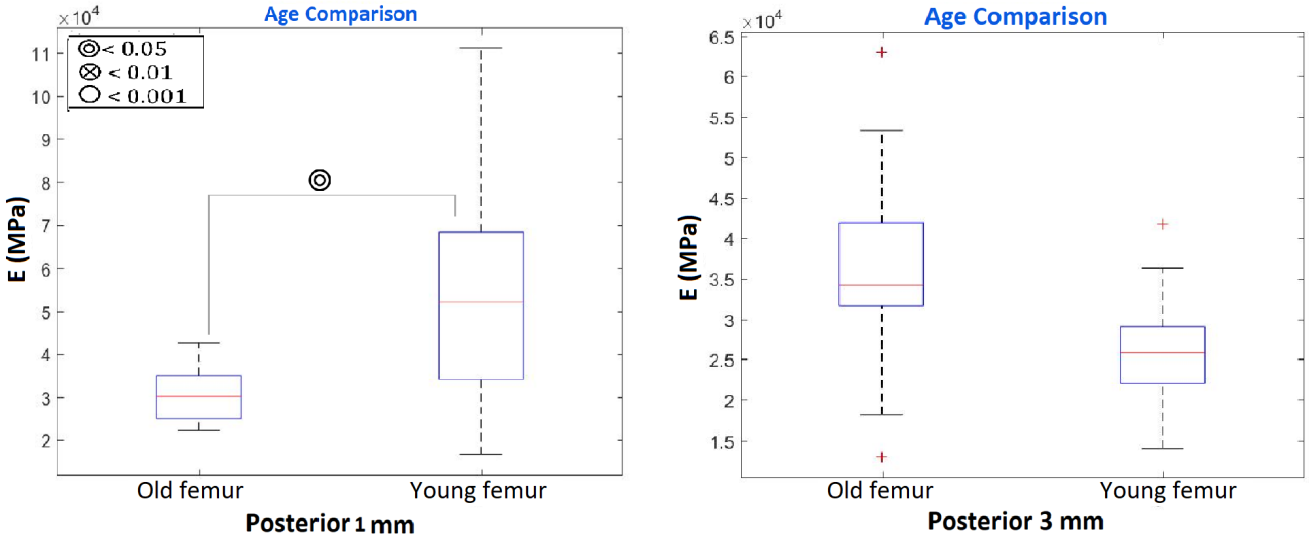

Figure 4.30: Age comparison of E in the posterior cortex of beam size 3 mm and 1 mm

4.2.7 Anatomical Location Comparison

In this section comparison of the anatomical locations is considered to better understanding of the effect of different anatomical sites on fracture behaviour. In the case of the old femur, no significant differences were observed in 3 mm beam size. In contrast, there were significant differences in K-Max, J, and E in 1 mm beam size (see Appendix B). On the other hand, in the young femur, significant difference was observed between the anterior cortex and other cortices in K-Slope, K-Max, J-Slope, and J in case of 3 mm beam size, see figures below. Additionally, the significant differences for 1 mm and 1.7 mm beam sizes can be found in Appendix B.2.

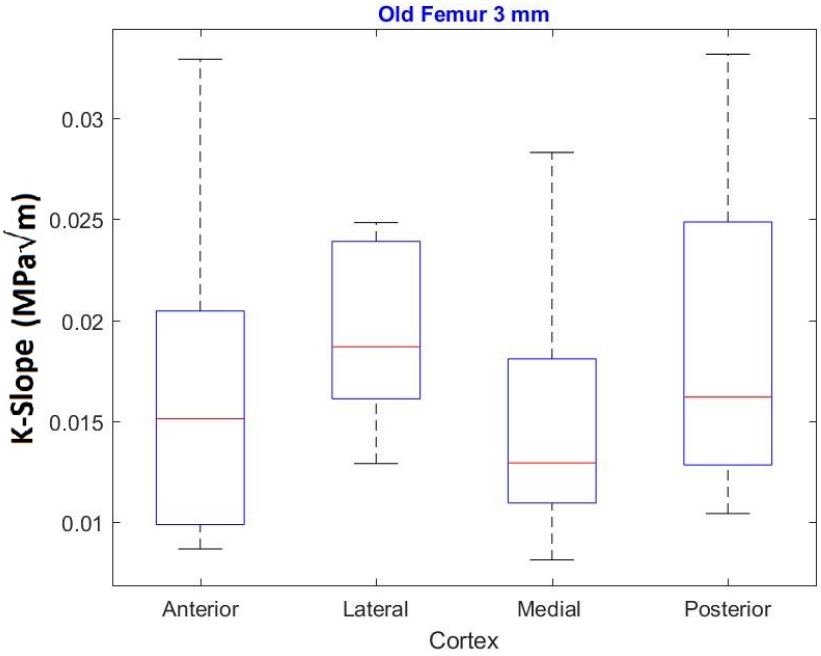

Figure 4.31: Comparison of anatomical locations of K-Slope in the old equine femur for beam size 3 mm

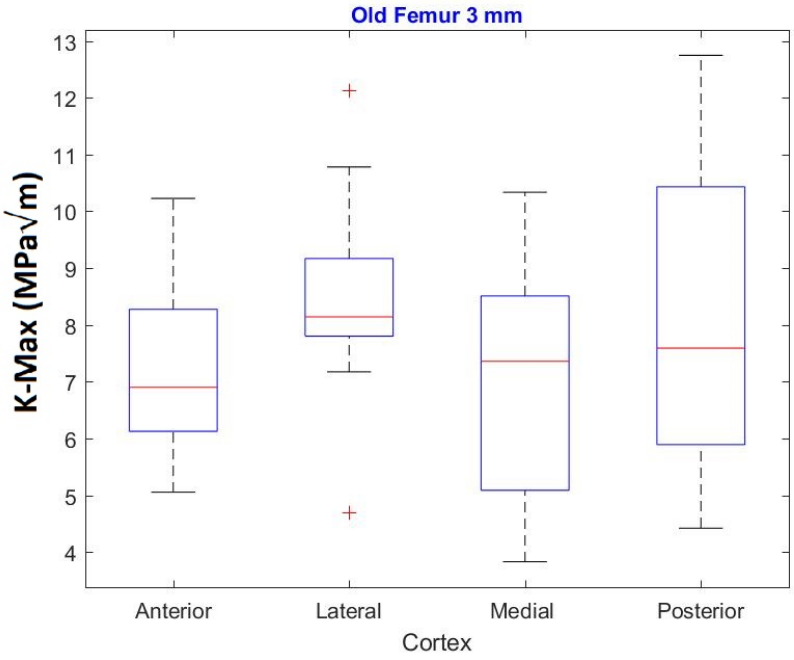

Figure 4.32: Comparison of anatomical locations of K-Max in the old equine femur for beam size 3 mm

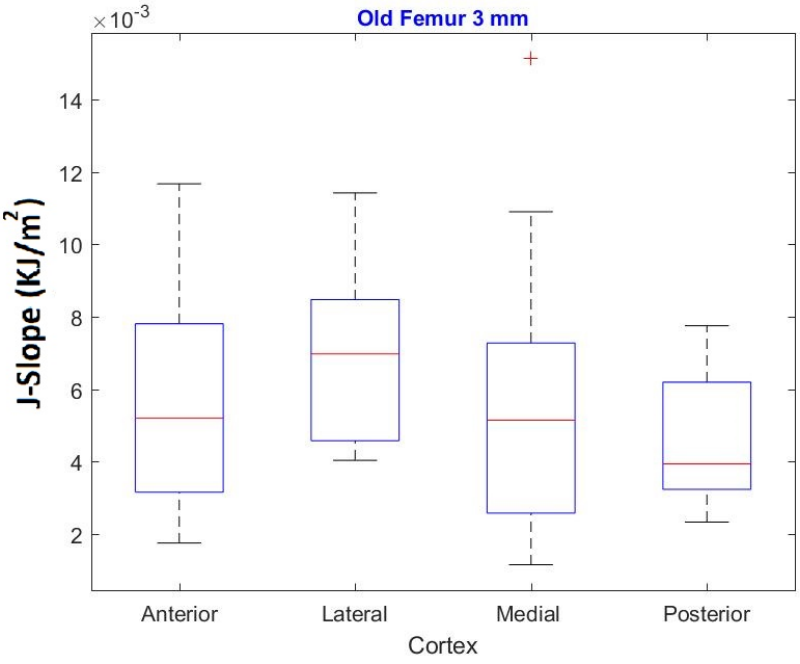

Figure 4.33: Comparison of anatomical locations of J-Slope in the old equine femur for beam size 3 mm

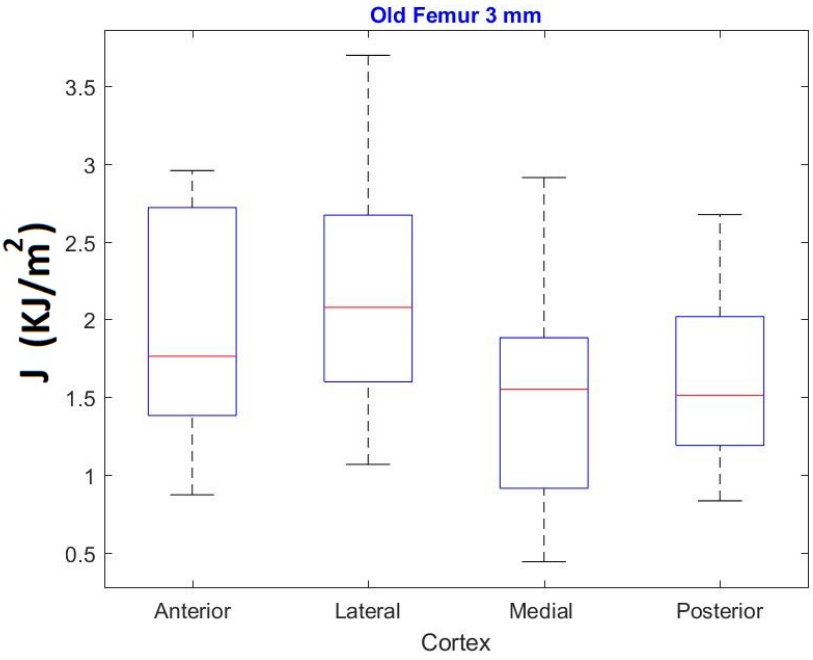

Figure 4.34: Comparison of anatomical locations of J in the old equine femur for beam size 3 mm

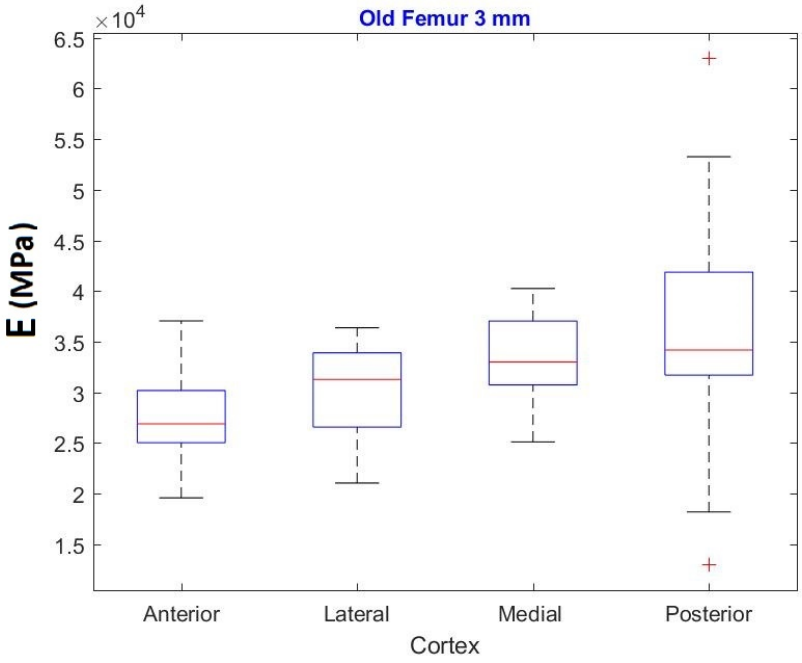

Figure 4.35: Comparison of anatomical locations of E in the old equine femur for beam size 3 mm

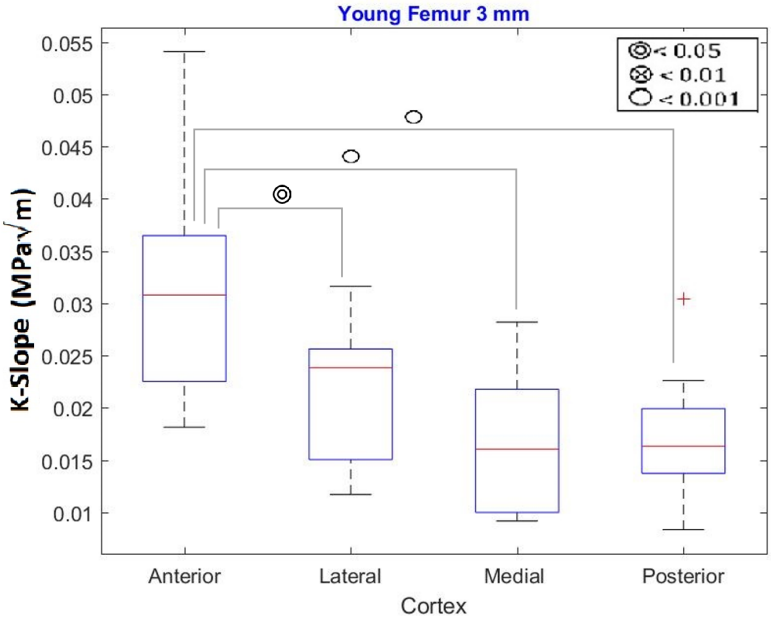

Figure 4.36: Comparison of anatomical locations of K-Slope in the young equine femur for beam size 3 mm

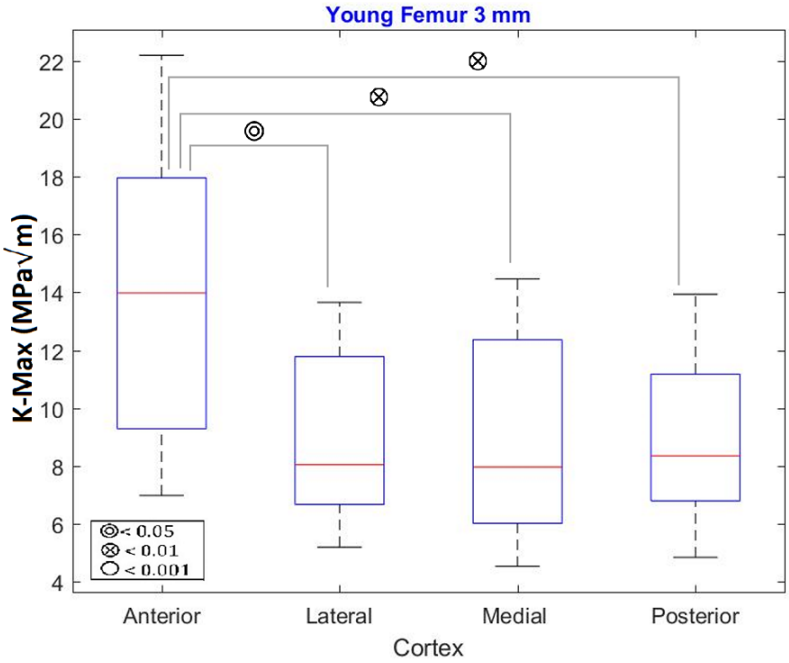

Figure 4.37: Comparison of anatomical locations of K-Max in the young equine femur for beam size 3 mm

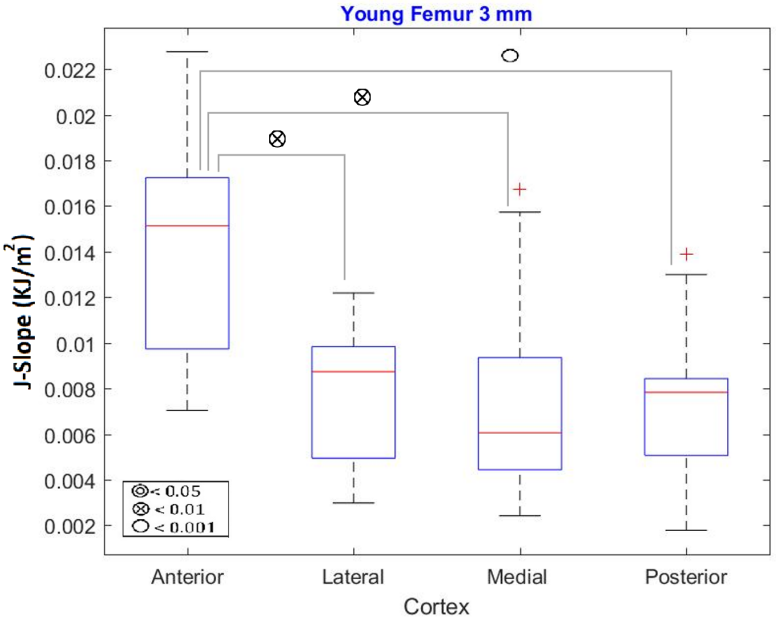

Figure 4.38: Comparison of anatomical locations of J-Slope in the young equine femur for beam size 3 mm

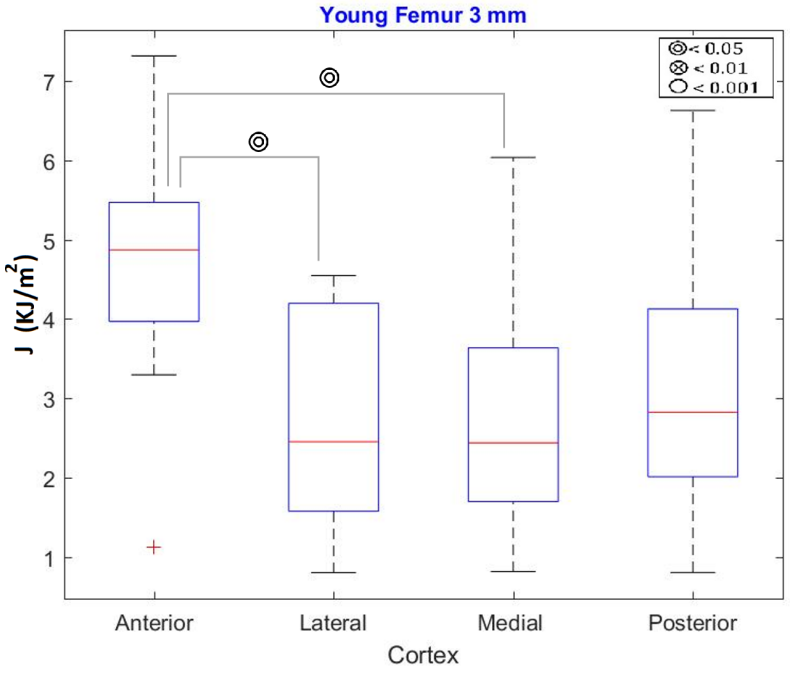

Figure 4.39: Comparison of anatomical locations of J in the young equine femur for beam size 3 mm

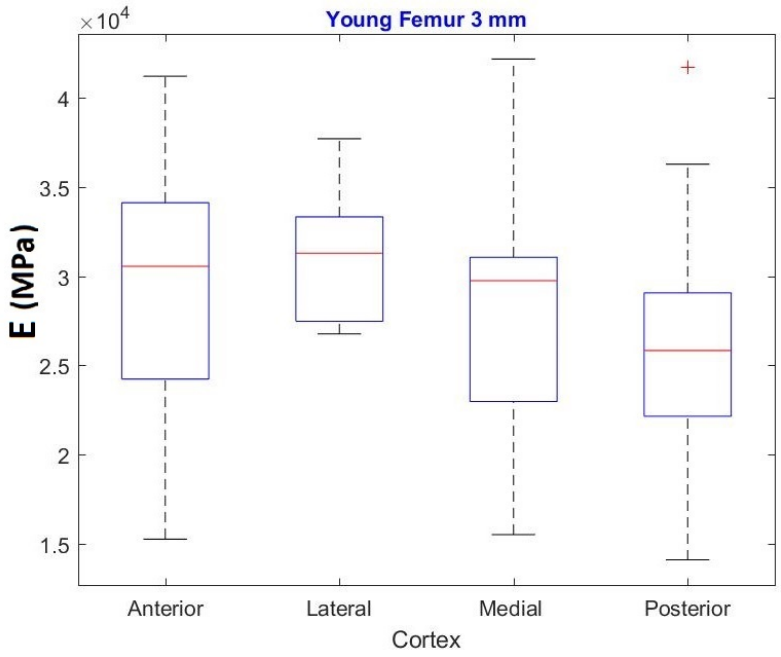

Figure 4.40: Comparison of anatomical locations of E in the young equine femur for beam size 3 mm

Chapter 5

Discussion and Conclusion

The mechanical properties of equine and bovine cortical bone from the femur mid-shaft were determined through mechanical testing SENB of specimens under three-point bending conditions. This study was conducted to observe whether the beam size, age, and location influence the fracture toughness, fracture energy, and effective modulus of cortical bone. The initial study using bovine bone had several issues such as the bovine age was unknown and the bone was kept in a freezer at -20 °C for long-term storage. As a result of the long term sample storage, the bone was potentially more brittle and fragile compared to its native state due to tissue deterioration. Furthermore, not enough tissue was available to differentiate between anatomical locations.

Nevertheless, important results were obtained from two fresh equine cortical bones of different ages were acquired to repeat the initial study and attempt to limit variability in the results. Typically, bone tissue used in biomechanical studies is preserved at -80 °C to keep the bone in the best condition and to avoid protein denaturation; hence, the equine bone was kept in a freezer at -80 °C. A distinct limitation of the experimental results used in both studies was the creation of a notch that is the initial starting point for fracture. Instead of analysing fractures initiated by naturally existing crack tips, artificial pre cracks (notches) were made using a diamond saw and a razor blade to induce specific conditions for fracture initiation and propagation. Since the notch was created by hand, the notch sizes were likely not the same size for all specimens. Despite all these limitations, all samples were treated the same way and responded to the limitations in the same manner. In this thesis, the effect of beam sizes, age, and different anatomical locations were studied. Each factor was investigated through three main mechanical properties: fracture

toughness, fracture energy, and elastic properties.

Before going to the result discussion, it should be mentioned that due to an issue in the algorithm of Matlab codes K-Initial and J-Initial had negative values. The values were extrapolated from R-curves. The linear regression was used to determine the slopes. However, some data had non-linear shapes, whereas the linear fit was not proper for the determination of the initial values; as a result, negative values were obtained. Therefore, it should be applied a better model to determine the initial values, but in this thesis, due to time constraint, K-Initial and J-Initial were not considered.

Beam size effect: Considering the toughness properties less noticeable difference was found in K-Slope in the medial cortex of both equine femurs and the posterior cortex of the young femur between the smallest and largest beam size. Furthermore, the significant difference was observed in K-Max in all cortices of the young equine femur, except in the posterior cortex. A substantial increase, about twice in value, was observed in the anterior and lateral cortex between beam sizes of 1 mm and 3 mm, as well as 1 mm and 1.7 mm, respectively. On the other hand, in the case of the old equine femur, the difference in the anterior and posterior cortices was observed between 1 mm and 3 mm, 1 mm and 1.7 mm.

For the bovine bone, no significant difference was observed in K-Slope between the beam sizes. In contrast, the smallest p-value was found in K-Max between the beam sizes 1 mm and 3 mm. In fracture energy properties, no significant difference was observed in J-Slope for the old equine femur. Although in the young equine femur, the smallest p-value was found in J-Slope in the lateral cortex between 1.7 mm and 3 mm. The most significant difference was observed between beam sizes in J in the young equine femur. On the other hand, for the bovine femur, no significant difference was found in J-Slope. However, the smallest p-value was observed in J between smallest and largest beam size.

Overall, in the old femur, most of the significant differences happen between the smallest and the largest beam size, while the properties of the younger femur are more often significantly different for each beam size. This indicates a reduced sensitivity to beam size in the old donor compared to the young donor, which may be related to the skeletal maturity that can impact the microstructure of cortical bone.

In elastic property, significant differences were observed in all cortices of both femurs between beam sizes, except in the posterior cortex of the old femur. The smallest p-values were found in all cortex except in the anterior cortex of the young femur between 1.7 mm and 3 mm. On

the other hand, there was no significant difference in all beam sizes for the bovine femur. That means the beam sizes did not affect the elastic modulus in the bovine case. In the equine case, it can be observed from the obtained results that with increasing beam size the elastic modulus decreases. As seen in Equation 2.19 with increasing beam size the notch length, i.e. the un-cracked ligament length, increases while the ratio of the support span to the specimen thickness is constant for all beam sizes. Additionally, it should be mentioned that the values of elastic modulus in this thesis were overestimated up to 100 GPa because the applied elastic modulus equation from [113] calculated for one-third of the specimen thickness as the notch length while in this thesis, the notch length was measured half of the specimen thickness.

Regarding the fracture energy, J, two regions are considered. Firstly J_{el} rises because of reducing the elastic modulus with increasing the notch length. Secondly, J_{pl} increases due to growing the plastic area under the load-displacement curve. Furthermore, the effective stress intensity factor, K_{eff}, increases with increasing beam size, because of the direct proportionality with J.

This thesis investigated fracture behaviour in case of small specimens such as 1 mm in order to find a proper size to further study of mechanical and structural properties in a small sample where a larger sample is not possible to obtain such as femur neck, which has a critical size and geometry. Finally, cortical bone mechanical properties from both young and old femurs were found to be sensitive to beam size, particularly in the case of the 1 mm size beam. Hence, care should be taken when using small beam sizes as their mechanical properties cannot be directly compared to those of beam sizes 3 mm or larger. However, most of the significant differences of fracture energy, J, in the largest beam size still present in the smallest beam size with the lower detectability differences except for one case. Therefore, it should be feasible to use J for smaller samples where it is not possible to obtain larger samples.

Age and anatomical locations effects: From the previous results, it can be understood the small beam size is not ideal and has to be used only if no larger samples can be obtained. Therefore, the 3 mm and 1 mm beam sizes are considered for age effect while the 3 mm is studied for anatomical sites influence. However, the comparison in case of 1.7 mm can be found in the appendix.

Considering the anatomical locations, the most significant differences in fracture toughness and fracture energy were observed in the anterior cortex of the young equine femur, which were almost twice in value compared to the other compartments. In contrast, almost no difference was found in the other cortices. These observations could be a result of differences in bone mineral content

and osteon size in different regions of the cortex. In view of the fact that osteon's role in cracking mechanisms depends on the osteon's mechanical properties related to the surrounding bone, the differentiation in osteon structure between different anatomical locations may result in different behaviour of fracture toughness[13,115]. Additionally, due to physiological loading applied by animal's weight and muscle forces, the long bone is exposed to combined loading conditions that are non-uniform. Hence, these differences in results between anatomical locations of the young femur likely occur because of structural and material property heterogeneity across the bone cross-section. As seen in Figure 5.2 and Figure 5.4, the fracture toughness and fracture energy results indicate the anterior cortex based on osteon density more resistant to fracture compared to other cortices. Moreover, Table 5.1 shows the osteon density data of both femurs. The difference in the relationship of the microstructure to fracture toughness between largest and smallest beam size may be connected to potential differences in osteon structure between two beam sizes. Since due to osteon size, in the 3 mm beam size exists more osteon in the un-cracked region compared with the 1 mm beam size.

Based on some studies, microstructural elements such as porosity, osteon size and density, distribution of minerals, and orientation of collagen fibrils are key factors to evaluate the mechanical and structural features of bone[13,115-117]. Therefore, after calculating bone porosity in this thesis, BT/TV was considered the same for all specimens whereas the osteon densities were found different between anterior cortex compared to the other cortices. Nevertheless, for future studies, it is suggested to consider all mentioned factors to investigate the fracture behaviour of bone.

Table 5.1: Osteon density in different anatomical locations in both equine femurs ($\frac{Osteon_{number}}{mm^2}$)

	Anterior	**Lateral**	**Medial**	**Posterior**
Old Femur (11-year-old)	15.7	18.1	21.74	20.87
Young Femur (5-year-old)	17.4	21.3	20.52	20.17

In conclusion, the results from this investigation show the fracture toughness of cortical bone from both old and young femurs was sensitive to beam size particularly in the young donor. Thus if a suitable sample size cannot be obtained this value may not be accurate compared with the standard sample size. However, the fracture energy in this study shows promising results which indicate it is possible to use a small sample when there is no way to obtain a larger sample. Therefore, the fracture energy can be used to determine the fracture behaviour of bone in mechanical testing on beams with less than 3 mm square cross-section. Thus further work is required to determine if beams with square cross-sections with a small variability, between 1.7 mm and 3 mm, produce the same fracture toughness properties as those with 3 mm square cross-sections. Reducing beam sizes to enable tissue level testing at anatomical locations with reduced cortical bone thickness remains an important topic of discussion. Regardless of the beam size, age, and location, a careful selection of bones and test variables is needed to achieve reliable and accurate fracture mechanical properties of bone.

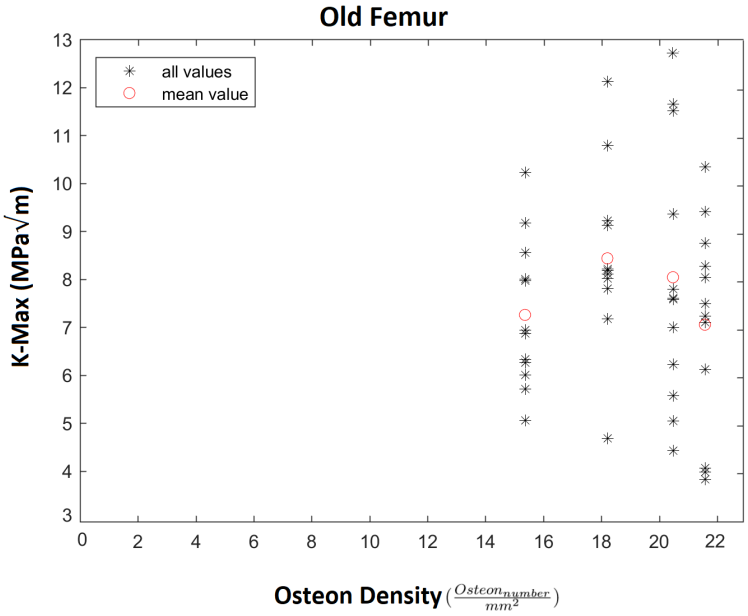

Figure 5.1: Correlation plot of fracture toughness versus osteon density in the old femur

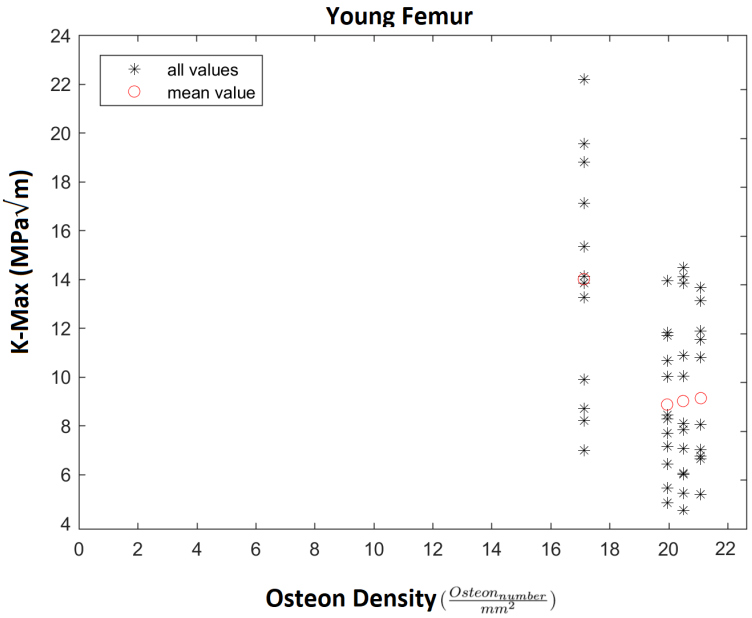

Figure 5.2: Correlation plot of fracture toughness versus osteon density in the young femur

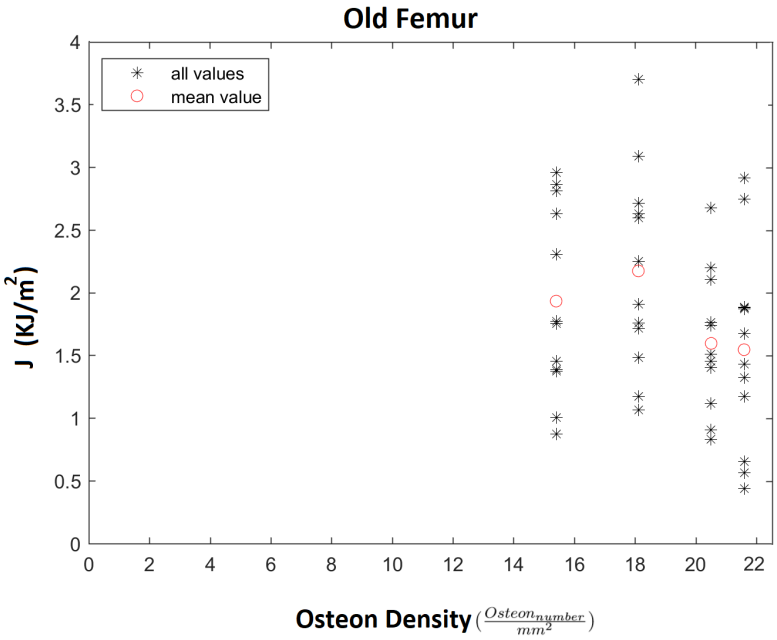

Figure 5.3: Correlation plot of fracture energy versus osteon density in the old femur

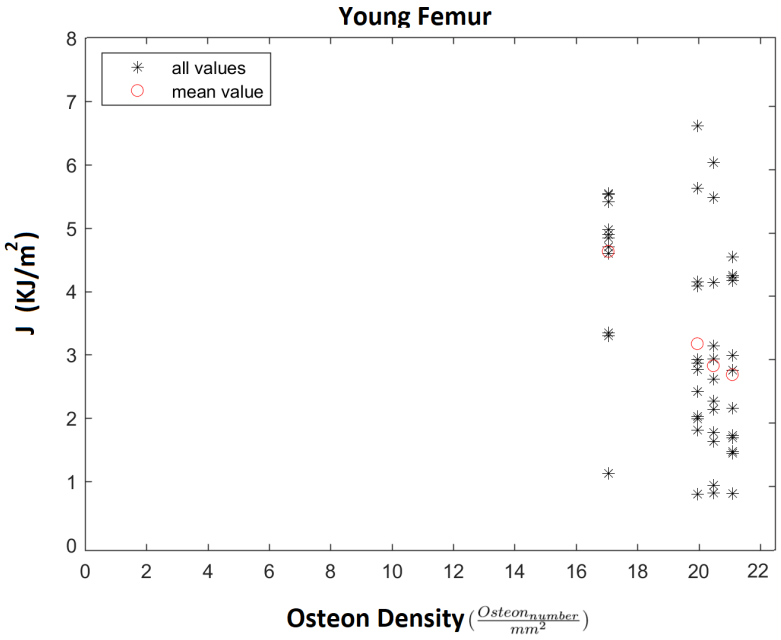

Figure 5.4: Correlation plot of fracture energy versus osteon density in the young femur

Appendix A

Description Bovine Femur

Table A.1: Result Shapiro-Wilk test for beam 1 mm

Beam 1 mm	**K-Initial**	**K-Slope**	**K-Max**	**J-Initial**	**J-Slope**	**J**	**E**
No. of Data	8	8	8	8	8	8	8
Mean	-2.2837	0.0464	8.109	-0.4917	0.0068	1.0554	73126.2625
Std.Dev	1.3215	0.0224	3.7766	0.27896	0.0033	0.54784	37445.6233
W-statistic	0.9904	0.8944	0.8663	0.9786	0.9022	0.9383	0.9504
p(W)	0.9957	0.2568	0.1386	0.9556	0.3023	0.5942	0.7152

Table A.2: Result Shapiro-Wilk test for beam 1.7 mm

Beam 1.7 mm	**K-Initial**	**K-Slope**	**K-Max**	**J-Initial**	**J-Slope**	**J**	**E**
No. of Data	10	10	10	10	10	10	10
Mean	-1.8403	0.054	13.6932	-0.7756	0.0108	2.1649	103268.9
Std.Dev	1.5417	0.0306	8.1542	0.606	0.0081	1.4824	55584.5138
W-statistic	0.8943	0.9261	0.6529	0.8427	0.9087	0.8561	0.8782
p(W)	0.1893	0.4106	**0.0002**	**0.0476**	0.2722	0.0686	0.1245

Table A.3: Improved Result by removing outliers for beam 1.7 mm

Beam 1.7 mm	**K-Max**	**J-Initial**
No. of Data	9	9
Mean	11.2355	-0.6487
Std.Dev	2.6166	0.4819
W-statistic	0.9317	0.8516
p(W)	0.4978	0.0776

Table A.4: Result Shapiro-Wilk test for beam 3 mm

Beam 3 mm	**K-Initial**	**K-Slope**	**K-Max**	**J-Initial**	**J-Slope**	**J**	**E**
No. of Data	8	8	8	8	8	8	8
Mean	-3.2742	0.0398	16.3767	-1.7642	0.0121	4.1528	61358.75
Std.Dev	3.0064	0.0144	5.3052	1.0575	0.0052	1.693	12357.7368
W-statistic	0.9317	0.9536	0.944	0.8875	0.941	0.9282	0.9296
p(W)	0.5317	0.7477	0.6507	0.2219	0.6208	0.4999	0.5126

Table A.5: Result Bartlett Test K-Initial

K-Initial	**Bartletts K-squared**	**df**	**p-value**
	5.6374	2	0.05968

Table A.6: Result Bartlett Test K-Slope

K- Slope	**Bartletts K-squared**	**df**	**p-value**
	3.7445	2	0.1538

Table A.7: Result Bartlett Test K-Max

K-Max	**Bartletts K-squared**	**df**	**p-value**
	3.411	2	0.1817

Table A.8: Result Bartlett Test J-Initial

J-Initial	Bartletts K-squared	df	p-value
	11.243	2	**0.0036**

Table A.9: Result Bartlett Test J-Slope

J-Slope	Bartlett K-squared	df	p-value
	5.3812	2	0.06784

Table A.10: Result Bartlett Test J

J	Bartlett K-squared	df	p-value
	7.353	2	**0.02531**

Table A.11: Result Bartlett Test E

E(Mpa)	Bartletts K-squared	df	p-value
	11.898	2	**0.002609**

Table A.12: Result ANOVA Test K-Initial

Groups	Count	Sum	Average	Variance		
K-Initial 1 mm	8	-18.26944	-2.28368	1.746346331		
K-Initial 1.7 mm	10	-18.40314	-1.84031378	2.376965077		
K-Initial 3 mm	8	-26.1933	-3.2741625	9.038372394		
ANOVA						
Source of Variation	**SS**	**df**	**MS**	**F**	**P-value**	**F crit**
Between Groups	9.345662	2	4.67283111	1.1092978	0.346801	3.422132
Within Groups	96.88572	23	4.21242247			
Total	106.2314	25				

Table A.13: Result ANOVA Test K-Slope

Groups	**Count**	**Sum**	**Average**	**Variance**		
K-Slope 1 mm	8	0.3711973	0.046399663	0.00050364		
K-Slope 1.7 mm	10	0.539751	0.0539751	0.0009368		
K-Slope 3 mm	8	0.318307	0.039788375	0.00020854		
ANOVA						
Source of Variation	**SS**	**Df**	**MS**	**F**	**P-value**	**F crit**
Between Groups	0.00090344	2	0.00045172	0.77439	0.472635	3.422132
Within Groups	0.01341643	23	0.00058332			
Total	0.01431987	25				

Table A.14: Result ANOVA Test K-Max

Groups	**Count**	**Sum**	**Average**	**Variance**		
K-Max 1 mm	8	64.87221	8.10902625	14.2630298		
K-Max 1.7 mm	9	101.1194	11.235489	6.8463565		
K-Max 3 mm	8	131.0134	16.376675	28.1451412		
ANOVA						
Source of Variation	**SS**	**Df**	**MS**	**F**	**P-value**	**F crit**
Between Groups	279.261189	2	139.630591	8.7361433	**0.0016123**	3.4433568
Within Groups	351.62805	22	15.983094			
Total	630.88924	24				

Table A.15: Result ANOVA Test For J-Slope

Groups	**Count**	**Sum**	**Average**	**Variance**		
J-Slope 1mm	8	0.05439436	0.006799295	1.11e-05		
J-Slope 1.7mm	10	0.1079167	0.01079167	6.58e-05		
J-Slope 3 mm	8	0.0966169	0.0120771	2.65e-05		
ANOVA						
Source of Variation	**SS**	**df**	**MS**	**F**	**P-value**	**F crit**
Between Groups	0.000123	2	6.13e-05	1.649488	0.214079	3.422132
Within Groups	0.000855	23	3.72e-05			
Total	0.000978	25				

Table A.16: Information Tukey HSD test for K-Initial

Group	**Diff**	**Lwr**	**upr**	**p adj**
B-A	0.4433662	-1.994724	2.881457	0.8925005
C-A	-0.9904825	-3.560456	1.579491	0.6056362
C-B	-1.4338487	-3.871939	1.004242	0.3220694

Table A.17: Information Tukey HSD test for K-Slope

Group	**Diff**	**Lwr**	**upr**	**p adj**
B-A	0.007575437	-0.02111508	0.03626596	0.7879328
C-A	-0.006611288	-0.03685375	0.02363118	0.8487752
C-B	-0.014186725	-0.04287725	0.0145038	0.4434026

Table A.18: Information Tukey HSD test for K-Max

Group	**Diff**	**Lwr**	**upr**	**p adj**
B-A	3.126463	-1.7535302	8.006455	0.2628428
C-A	8.267649	3.2461776	13.28912	**0.0012104**
C-B	5.141186	0.2611933	10.021179	**0.0377018**

Table A.19: Information Tukey HSD test for J-Initial

Group	Diff	Lwr	upr	p adj
B-A	-0.1570109	-0.9893922	0.6753704	0.8842314
C-A	-1.2724407	-2.1289541	-0.4159274	**0.0031875**
C-B	-1.1154299	-1.9478112	-0.2830485	**0.0075374**

Table A.20: Information Tukey HSD test for J-Slope

Group	Diff	Lwr	upr	p adj
B-A	0.003992375	-0.0032521	0.01123685	0.3674534
C-A	0.005277817	-0.00235853	0.012914165	0.215458
C-B	0.001285443	-0.005959033	0.008529918	0.8973544

Table A.21: Information Tukey HSD test for J

Group	Diff	Lwr	upr	p adj
B-A	1.109517	-0.4946282	2.713663	0.2150019
C-A	3.097396	1.4064785	4.788314	**0.0003696**
C-B	1.987879	0.3837334	3.592025	**0.0133564**

Table A.22: Information Tukey HSD test for E

Group	Diff	Lwr	upr	p adj
B-A	30142.64	-18579.32	78864.597	0.2873672
C-A	-11767.51	-63124.97	39589.942	0.8352837
C-B	-41910.15	-90632.11	6811.809	0.1009774

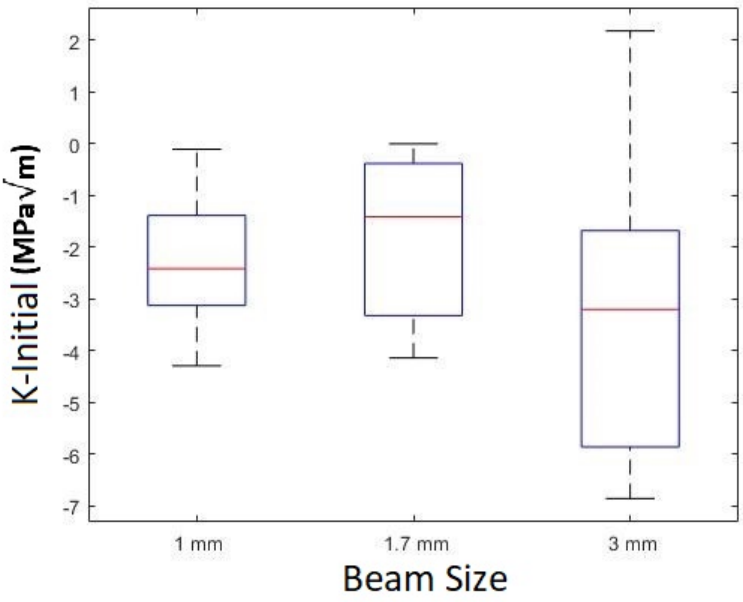

Figure A.1: Boxplot K-Initial

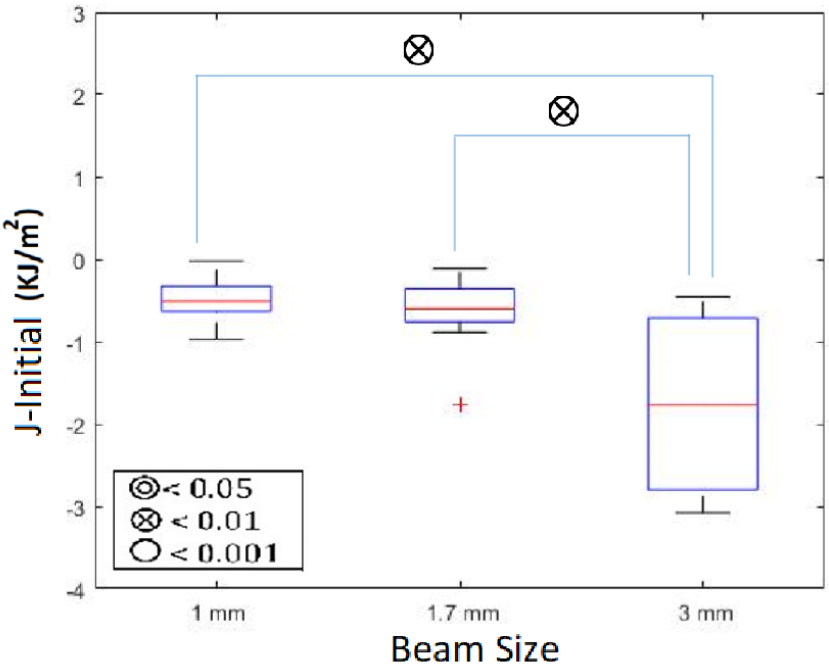

Figure A.2: Boxplot J-Initial after removing outliers and with significant between beam sizes labelled in the legend

Appendix B

Description Equine Femur

B.1 Old Equine Femur

Table B.1: Result Shapiro-Wilk test for 1 mm Anterior Beam

Ant-S1-1mm	**K-Initial**	**K-Slope**	**K-Max**	**J-Initial**	**J-Slope**	**J**	**E**
No. of Data	12	12	12	12	12	12	12
Mean	1.2252	0.0297	4.9287	-0.0361	0.0049	0.5775	47383.2500
Std. Dev	0.6438	0.0201	1.5292	0.1358	0.0031	0.2703	23327.5979
W-statistic	0.8425	0.8809	0.9709	0.7092	0.9361	0.8847	0.6715
P(W)	**0.0297**	0.0900	0.9202	**0.0010**	0.4496	0.1007	**0.0005**

Table B.2: Improved Result Shapiro-Wilk by removing outliers for 1 mm Anterior Beam

Ant-S1-1mm	**K-Initial**	**J-Intial**	**E**
No. of Data	11	11	10
Mean	1.3790	-0.0001	38371.6
Std. Dev	0.3792	0.0567	5457.4220
W-statistic	0.9078	0.9415	0.9898
P(W)	0.2298	0.5379	0.9965

Table B.3: Result Shapiro-Wilk test for 1.7 mm Anterior Beam

Ant-S1-1.7mm	**K-Initial**	**K-Slope**	**K-Max**	**J-Initial**	**J-Slope**	**J**	**E**
No. of Data:	12	12	12	12	12	12	12
Mean	0.7614	0.0229	7.1256	-0.2258	0.0059	1.4174	36937.0000
Std. Dev	0.7216	0.0087	2.3231	0.1604	0.0026	0.6464	13080.7042
W-statistic	0.9665	0.9788	0.9467	0.9679	0.9264	0.9247	0.8894
P(W)	0.8708	0.9782	0.5887	0.8877	0.3437	0.3270	0.1158

Table B.4: Result Shapiro-Wilk test for 3 mm Anterior Beam

Ant-S1-3mm	**K-Initial**	**K-Slope**	**K-Max**	**J-Initial**	**J-Slope**	**J**	**E**
No. of Data:	12	12	12	12	12	12	12
Mean	-0.0737	0.0165	7.2539	-0.6073	0.0057	1.9313	27335.9167
Std. Dev	1.0368	0.0076	1.5419	0.4642	0.0030	0.7500	4760.7537
W-statistic	0.9012	0.8887	0.9604	0.8908	0.9511	0.9095	0.9750
P(W)	0.1643	0.1134	0.7897	0.1206	0.6535	0.2101	0.9553

Table B.5: Result Bartlett test for K-Initial Anterior

ANT-S1-K-Initial	**Bartletts K-squared**	**df**	**p-value**
	8.7165	2	**0.0128**

Table B.6: Result Kruskal-Wallis Test for K-Initial Anterior

ANT-S1-K-Initial	**Kruskal-Wallis chi-squared**	**df**	**p-value**
	14.756	2	**0.0006**

Table B.7: Result Bartlett test for K-Slope Anterior

ANT-S1-K-Slope	**Bartletts K-squared**	**df**	**p-value**
	12.532	2	**0.0019**

Table B.8: Result Kruskal-Wallis Test for K-Slope Anterior

ANT-S1-K-Slope	Kruskal-Wallis chi-squared	df	p-value
	4.4505	2	0.108

Table B.9: Result Bartlett Test for K-Max Anterior

ANT-S1-K-Max	Bartletts K-squared	Df	p-value
	2.5818	2	0.275

Table B.10: Result ANOVA Test for K-Max Anterior

Groups	Count	Sum	Average	Variance		
K-Max 1 mm	12	59.1447	4.928725	2.338306		
K-Max 1.7 mm	12	85.5073	7.125608	5.396622		
K-Max 3 mm	12	87.0464	7.253867	2.377605		
ANOVA						
Source of Variation	**SS**	**df**	**MS**	**F**	**P-value**	**F crit**
Between Groups	40.99612	2	20.49806	6.080987	**0.005646**	3.284918
Within Groups	111.2379	33	3.370844			
Total	152.234	35				

Table B.11: Information Tukey HSD Test for K-Initial Anterior

Group	Diff	Lwr	upr	p adj
B-A	-0.6176124	-1.407836	0.17261087	0.1493012
C-A	-1.4526916	-2.242915	-0.66246829	**0.0002315**
C-B	-0.8350792	-1.607933	-0.06222554	**0.0319715**

Table B.12: Information Tukey HSD test for K-Slope Anterior

Group	Diff	Lwr	upr	p adj
B-A	-0.006770392	-0.020198	0.006657213	0.4402074
C-A	-0.013154292	-0.0265819	0.000273313	0.0558074
C-B	-0.0063839	-0.0198115	0.007043704	0.4810761

Table B.13: Information Tukey HSD test for K-Max Anterior

Group	Diff	Lwr	upr	p adj
B-A	2.1968833	0.3576708	4.036096	**0.0163462**
C-A	2.3251417	0.4859292	4.164354	**0.0106608**
C-B	0.1282583	-1.7109542	1.967471	0.983995

Table B.14: Result Bartlett Test for J-Initial Anterior

ANT-S1-J-Initial	Bartletts K-squared	df	p-value
	33.8305	2	**4.51e-08**

Table B.15: Result Kruskal-Wallis Test for J-Initial Anterior

ANT-S1-J-Initial	Kruskal-Wallis chi-squared	df	p-value
	21.4612	2	**2.19e-05**

Table B.16: Result Bartlett Test for J-Slope Anterior

ANT-S1-J-Slope	Bartletts K-squared	df	p-value
	0.4367	2	0.8039

Table B.17: Result ANOVA Test J-Slope Anterior

Groups	**Count**	**Sum**	**Average**	**Variance**		
J-Slope 1mm	12	0.058331	0.004861	9.63e-06		
J-Slope 1.7mm	12	0.071157	0.00593	6.53e-06		
J-Slope 3mm	12	0.068298	0.005691	8.99e-06		
ANOVA						
Source of Variation	**SS**	**df**	**MS**	**F**	**P-value**	**F crit**
Between Groups	7.56e-06	2	3.78e-06	0.450735	0.641024	3.284918
Within Groups	0.000277	33	8.38e-06			
Total	0.000284	35				

Table B.18: Result Bartlett Test for J Anterior

ANT-S1-J	**Bartletts K-squared**	**df**	**p-value**
	9.7791	2	**0.0075**

Table B.19: Result Kruskal-Wallis Test for J Anterior

ANT-S1-J	**Kruskal-Wallis chi-squared**	**df**	**p-value**
	20.1637	2	**4.18e-05**

Table B.20: Information Tukey HSD Test for J-Initial Anterior

Group	**Diff**	**Lwr**	**upr**	**p adj**
B-A	-0.2256461	-0.522784	0.0714918	0.1650065
C-A	-0.607222	-0.9043599	-0.31008412	**0.0000543**
C-B	-0.3815759	-0.6721825	-0.09096931	**0.007908**

Table B.21: Information Tukey HSD Test for J-Slope Anterior

Group	Diff	Lwr	upr	p adj
B-A	0.001068869	-0.001831453	0.003969191	0.6414411
C-A	0.000830573	-0.002069749	0.003730894	0.7635875
C-B	-0.000238297	-0.003138619	0.002662025	0.9778567

Table B.22: Information Tukey HSD Test for J Anterior

Group	Diff	Lwr	upr	p adj
B-A	0.8398283	0.24623096	1.433426	**0.0040737**
C-A	1.3537208	0.76012346	1.947318	**0.0000093**
C-B	0.5138925	-0.07970487	1.10749	0.1003205

Table B.23: Result Bartlett Test for E Anterior

ANT-S1-E	Bartletts K-squared	df	p-value
	12.8234	2	**0.0016**

Table B.24: Result Kruskal-Wallis Test for E Anterior

ANT-S1-E	Kruskal-Wallis chi-squared	df	p-value
	10.944	2	**0.0042**

Table B.25: Information Tukey HSD test for E Anterior

Group	Diff	Lwr	upr	p adj
B-A	-1434.6	-10706.03	7836.8295	0.9233675
C-A	-11035.683	-20307.11	-1764.2539	**0.016899**
C-B	-9601.083	-18441.04	-761.1222	**0.031019**

Table B.26: Result Shapiro-Wilk test for 1 mm Lateral Beam

Lat-S1-1mm	**K-Initial**	**K-Slope**	**K-Max**	**J-Initial**	**J-Slope**	**J**	**E**
No. of Data	12	12	12	12	12	12	12
Mean	-0.3217	0.1075	10.8848	-0.2597	0.0100	1.2656	1839.333
Std. Dev	5.1018	0.2411	10.7514	0.4850	0.0084	0.8245	4314.697
W-statistic	0.7669	0.4044	0.6471	0.9562	0.8771	0.9295	0.3891
P(W)	**0.0040**	**3.7849e-06**	**2.7285e-04**	0.7288	0.0804	0.3752	**3.001e-06**

Table B.27: Improved Result Shapiro-Wilk by removing outliers for 1 mm Lateral Beam

Lat-S1-1mm	**K-Initial**	**K-Slope**	**K-Max**	**E**
No. of Data	11	11	11	10
Mean	0.9876	0.0381	7.9812	51609.2000
Std. Dev	2.4501	0.0218	3.9825	22105.1003
W-statistic	0.9412	0.8979	0.9197	0.8872
p(W)	0.5345	0.1743	0.3161	0.1578

Table B.28: Result Shapiro-Wilk test for 1.7 mm Lateral Beam

Lat-S1-1.7mm	**K-Initial**	**K-Slope**	**K-Max**	**J-Initial**	**J-Slope**	**J**	**E**
No. of Data	12	12	12	12	12	12	12
Mean	0.5775	0.0370	11.0523	-0.7050	0.0135	3.0644	42557.1667
Std. Dev	2.8221	0.0245	6.4869	1.0563	0.0101	2.2246	17086.2368
W-statistic	0.8545	0.8701	0.9129	0.9285	0.9237	0.9340	0.8578
P(W)	**0.0417**	0.0655	0.2325	0.3643	0.3177	0.4244	**0.0459**

Table B.29: Improved Result Shapiro-Wilk by removing outliers for 1.7 mm Lateral Beam

Lat-S1-1.7 mm	**K-Initial**	**E**
No. of Data	9	11
Mean	0.7382	38907.3636
Std. Dev	0.7667	12053.8549
W-statistic	0.9203	0.9096
p(W)	0.3944	0.2415

Table B.30: Result Shapiro-Wilk test for 1.7 mm Lateral Beam

Lat-S1-3mm	**K-Initial**	**K-Slope**	**K-Max**	**J-Initial**	**J-Slope**	**J**	**E**
No. of Data	12	12	12	12	12	12	12
Mean	0.2822	0.0216	8.4329	-0.5196	0.0069	2.1717	33202.3333
Std. Dev	0.8386	0.0079	1.8349	0.2741	0.0023	0.7977	11633.1800
W-statistic	0.9815	0.8171	0.9185	0.9493	0.9286	0.9649	0.7266
P(W)	0.9889	**0.0148**	0.2734	0.6264	0.3658	0.8504	**0.0015**

Table B.31: Improved Result Shapiro-Wilk by removing outliers for 3 mm Lateral Beam

Lat-S1-3 mm	**K-Slope**	**E**
No. of Data	11	11
Mean	0.0197	30135.0909
Std. Dev	0.0044	4967.7642
W-statistic	0.8831	0.9483
p(W)	0.1140	0.6224

Table B.32: Result Bartlett Test for K-Initial Lateral

LAT-S1-K-Initial	**Bartletts K-squared**	**df**	**p-value**
	16.0092	2	**0.0003**

Table B.33: Result Kruskal-Wallis Test for K-Initial Lateral

LAT-S1-K-Initial	Kruskal-Wallis chi-squared	df	p-value
	2.2548	2	0.3239

Table B.34: Result Bartlett Test for K-Slope Lateral

LAT-S1-K-Slope	Bartletts K-squared	df	p-value
	20.8011	2	**3.04e-05**

Table B.35: Result Kruskal-Wallis Test for K-Slope Lateral

LAT-S1-K-Slope	Kruskal-Wallis chi-squared	df	p-value
	6.5468	2	**0.0379**

Table B.36: Result Bartlett Test for K-Max Lateral

LAT-S1-K-Max	Bartletts K-squared	df	p-value
	14.0618	2	**0.0009**

Table B.37: Result Kruskal-Wallis Test for K-Max Lateral

LAT-S1-K-Max	Kruskal-Wallis chi-squared	df	p-value
	2.2146	2	0.3304

Table B.38: Information Tukey HSD Test for K-Initial Lateral

Group	Diff	Lwr	upr	p adj
B-A	-0.2494095	-2.004134	1.5053146	0.9344876
C-A	-0.7054573	-2.335085	0.9241704	0.5404398
C-B	-0.4560478	-2.177556	1.2654608	0.7914687

Table B.39: Information Tukey HSD test for K-Slope Lateral

Group	Diff	Lwr	upr	p adj
B-A	-0.001124167	-0.02094435	0.018696018	0.9893181
C-A	-0.018436455	-0.03868293	0.00181002	0.0799259
C-B	-0.017312287	-0.03713247	0.002507898	0.0962766

Table B.40: Information Tukey HSD test for K-Max Lateral

Group	Diff	Lwr	upr	p adj
B-A	3.0711455	-1.582113	7.724404	0.2512588
C-A	0.4517621	-4.201496	5.105021	0.9691406
C-B	-2.6193833	-7.17036	1.931593	0.3456466

Table B.41: Result Bartlett Test for J-Initial Lateral

LAT-S1-J-Initial	Bartletts K-squared	df	p-value
	17.9256	2	**0.0001**

Table B.42: Result Kruskal-Wallis Test for J-Initial Lateral

LAT-S1-J-Initial	Kruskal-Wallis chi-squared	df	p-value
	2.5961	2	0.2731

Table B.43: Result Bartlett Test for J-Slope Lateral

LAT-S1-J-Slope	Bartletts K-squared	df	p-value
	17.9701	2	**0.0001**

Table B.44: Result Kruskal-Wallis Test for J-Slope Lateral

LAT-S1-J-Slope	Kruskal-Wallis chi-squared	df	p-value
	2.4339	2	0.2961

Table B.45: Result Bartlett Test for J Lateral

LAT-S1-J	Bartletts K-squared	df	p-value
	15.3085	2	**0.0005**

Table B.46: Result Kruskal-Wallis Test for J Lateral

LAT-S1-J	Kruskal-Wallis chi-squared	df	p-value
	7.0736	2	**0.0291**

Table B.47: Information Tukey HSD test for J-Initial Lateral

Group	Diff	Lwr	upr	p adj
B-A	-0.4452809	-1.1359817	0.2454199	0.2675
C-A	-0.2599019	-0.9506027	0.4307989	0.6296312
C-B	0.185379	-0.5053218	0.8760798	0.7888445

Table B.48: Information Tukey HSD test for J-Slope Lateral

Group	Diff	Lwr	upr	p adj
B-A	0.003487883	-0.004224632	0.011200398	0.5149815
C-A	-0.003169337	-0.010881852	0.004543178	0.5769027
C-B	-0.00665722	-0.014369735	0.001055295	0.1015891

Table B.49: Information Tukey HSD test for J Lateral

Group	Diff	Lwr	upr	p adj
B-A	1.7987683	0.3511129	3.2464237	**0.012191**
C-A	0.906055	-0.5416004	2.3537104	0.2876703
C-B	-0.8927133	-2.3403687	0.5549421	0.2979087

Table B.50: Result Bartlett Test for E Lateral

LAT-S1-E	Bartletts K-squared	df	p-value
	16.7574	2	**0.0002**

Table B.51: Result Kruskal-Wallis Test for E Lateral

LAT-S1-E	Kruskal-Wallis chi-squared	df	p-value
	8.4071	2	**0.0149**

Table B.52: Information Tukey HSD test for E Lateral

Group	Diff	Lwr	upr	p adj
B-A	-12701.836	-28348.57	2944.899	0.1290264
C-A	-21474.109	-37120.84	-5827.373	**0.0056039**
C-B	-8772.273	-24041.92	6497.378	0.3446785

Table B.53: Result Shapiro-Wilk test for 1 mm Medial Beam

Med-S1-1mm	K-Initial	K-Slope	K-Max	J-Initial	J-Slope	J	E
No. of Data	12	12	12	12	12	12	12
Mean	0.7620	0.0352	6.7188	-0.1969	0.0061	0.8662	59103.4167
Std. Dev	1.5572	0.0153	2.6442	0.2478	0.0033	0.5622	23361.6351
W-statistic	0.9301	0.9158	0.9229	0.8912	0.9378	0.9063	0.8907
P(W)	0.3815	0.2527	0.3106	0.1223	0.4704	0.1915	0.1205

Table B.54: Result Shapiro-Wilk test for 1.7 mm Medial Beam

Med-S1-1.7mm	K-Initial	K-Slope	K-Max	J-Initial	J-Slope	J	E
No. of Data	12	12	12	12	12	12	12
Mean	0.3288	0.0300	7.2466	-0.3503	0.0082	1.4483	37506.1667
Std. Dev	1.1747	0.0185	4.0115	0.3884	0.0063	0.8519	22071.5585
W-statistic	0.9477	0.8713	0.8365	0.8365	0.8765	0.9386	0.6376
P(W)	0.6039	0.0678	**0.0251**	**0.0251**	0.0791	0.4804	**0.0002**

Table B.55: Improved Result Shapiro-Wilk by removing outliers for 1.7 mm Medial Beam

Med-S1-1.7 mm	**K-Max**	**J-Initial**	**E**
No. of Data	11	11	11
Mean	6.2882	-0.2658	31461.2727
Std. Dev	2.3615	0.2679	7316.5059
W-statistic	0.9435	0.8687	0.9570
p(W)	0.5620	0.0746	0.7335

Table B.56: Result Shapiro-Wilk test for 3 mm Medial Beam

Med-S1-3mm	**K-Initial**	**K-Slope**	**K-Max**	**J-Initial**	**J-Slope**	**J**	**E**
No. of Data	12	12	12	12	12	12	12
Mean	-0.4790	0.0200	7.0488	-0.5480	0.0057	1.5445	33429.5833
Std. Dev	3.1262	0.0119	2.1633	0.9733	0.0041	0.7878	4389.6935
W-statistic	0.7690	0.8439	0.9247	0.8473	0.8925	0.9419	0.9787
P(W)	**0.0043**	**0.0309**	0.3276	**0.0340**	0.1270	0.5233	0.9779

Table B.57: Improved Result Shapiro-Wilk by removing outliers for 3 mm Medial Beam

Med-S1-3 mm	**K-Initial**	**K-Slope**	**J-Initial**
No. of Data	9	10	9
Mean	-0.0406	0.0156	-0.3632
Std. Dev	0.2323	0.0065	0.1910
W-statistic	0.9106	0.8797	0.9660
p(W)	0.3203	0.1296	0.8587

Table B.58: Result Bartlett Test for K-Initial Medial

MED-S1-K-Initial	**Bartletts K-squared**	**df**	**p-value**
	19.4801	2	**5.89e-05**

Table B.59: Result Kruskal-Wallis Test for K-Initial Medial

MED-S1-K-Initial	Kruskal-Wallis chi-squared	df	p-value
	6.1622	2	**0.0459**

Table B.60: Result Bartlett Test for K-Slope Medial

MED-S1-K-Slope	Bartletts K-squared	df	p-valu
	8.4078	2	**0.0149**

Table B.61: Result Kruskal-Wallis Test for K-Slope Medial

MED-S1-K-Slope	Kruskal-Wallis chi-squared	df	p-value
	8.8582	2	**0.0119**

Table B.62: Result Bartlett Test for K-Max Medial

MED-S1-K-Max	Bartletts K-squared	df	p-value
	0.4294	2	0.8068

Table B.63: Result ANOVA Test for K-Max Medial

Groups	Count	Sum	Average	Variance		
K-Max 1 mm	12	80.6255	6.718792	6.991857		
K-Max 1.7 mm	11	69.1704	6.288218	5.576475		
K-Max 3 mm	12	84.586	7.048833	4.67998		
ANOVA	12	80.6255	6.718792	6.991857		
Source of Variation	**SS**	**df**	**MS**	**F**	**P-value**	**F crit**
Between Groups	3.329262	2	1.664631	0.289257	0.750757	3.294537
Within Groups	184.155	32	5.754842			
Total	187.4842	34				

Table B.64: Information Tukey HSD test for K-Initial Medial

Group	Diff	Lwr	upr	p adj
B-A	-0.4332267	-1.628095	0.7616421	0.6483012
C-A	-0.8025606 -	-2.093166	0.4880451	0.2902139
C-B	-0.3693339	-1.65994	0.9212718	0.7621362

Table B.65: Information Tukey HSD test for K-Slope Medial

Group	Diff	Lwr	upr	p adj
B-A	-0.005174575	-0.01996871	0.00961956	0.6685515
C-A	-0.019539925	-0.03505614	-0.004023706	**0.0111238**
C-B	-0.01436535	-0.02988157	0.001150869	0.0739399

Table B.66: Information Tukey HSD test for K-Max Medial

Group	Diff	Lwr	upr	p adj
B-A	-0.4305735	-2.891307	2.03016	0.9034191
C-A	0.3300417	-2.076603	2.736686	0.9394363
C-B	0.7606152	-1.700118	3.221348	0.7300964

Table B.67: Result Bartlett Test for J-Initial Medial

MED-S1-J-Initial	Bartletts K-squared	df	p-value
	0.9575	2	0.6195

Table B.68: Result ANOVA Test for J-Initial Medial

Groups	Count	Sum	Average	Variance		
J-Initial 1mm	12	-2.36297	-0.19691	0.061392		
J-Initial 1.7mm	11	-2.92407	-0.26582	0.071758		
J-Initial 3mm	9	-3.26922	-0.36325	0.036483		
ANOVA						
Source of Variation	**SS**	**df**	**MS**	**F**	**P-value**	**F crit**
Between Groups	0.142326	2	0.071163	1.224936	0.30853	3.327654
Within Groups	1.684764	29	0.058095			
Total	1.82709	31				

Table B.69: Result Bartlett Test for J-Slope Medial

MED-S1-J-Slope	Bartletts K-squared	df	p-value
	4.6797	2	0.0963

Table B.70: Result ANOVA Test for J-Slope Medial

Groups	Count	Sum	Average	Variance		
J-Slope 1mm	12	0.073442	0.00612	1.09E-05		
J-Slope 1.7mm	12	0.098217	0.008185	3.95E-05		
J-Slope 3mm	12	0.068396	0.0057	1.66E-05		
ANOVA						
Source of Variation	**SS**	**df**	**MS**	**F**	**P-value**	**F crit**
Between Groups	4.25E-05	2	2.12E-05	0.950498	0.396877	3.284918
Within Groups	0.000737	33	2.23E-05			
Total	0.00078	35				

Table B.71: Result Bartlett Test for J Medial

MED-S1-J	Bartletts K-squared	df	p-value
	1.8855	2	0.3895

Table B.72: Result ANOVA Test for J Medial

Groups	Count	Sum	Average	Variance		
J 1 mm	12	10.39491	0.866243	0.316102		
J 1.7 mm	12	17.37931	1.448276	0.725674		
J 3 mm	12	18.53407	1.544506	0.620697		
ANOVA						
Source of Variation	**SS**	**df**	**MS**	**F**	**P-value**	**F crit**
Between Groups	3.232257	2	1.616128	2.916368	0.068189	3.284918
Within Groups	18.28721	33	0.554158			
Total	21.51947	35				

Table B.73: Information Tukey HSD test for J-Initial Medial

Group	Diff	Lwr	upr	p adj
B-A	-0.06891083	-0.3173857	0.17956406	0.7740688
C-A	-0.16633281	-0.4288171	0.09615148	0.2766451
C-B	-0.09742198	-0.3649707	0.17012678	0.6450841

Table B.74: Information Tukey HSD test for J-Slope Medial

Group	Diff	Lwr	upr	p adj
B-A	0.002064608	-0.00266977	0.006798987	0.538998
C-A	-0.000420475	-0.005154854	0.004313904	0.9741784
C-B	-0.002485083	-0.007219462	0.002249295	0.411812

Table B.75: Information Tukey HSD test for J Medial

Group	Diff	Lwr	upr	p adj
B-A	0.5820333	-0.16369279	1.3277595	0.150324
C-A	0.6782633	-0.06746279	1.4239895	0.0805414
C-B	0.09623	-0.64949612	0.8419561	0.9463215

Table B.76: Result Bartlett Test for E Medial

MED-S1-E	Bartletts K-squared	df	p-value
	28.397	2	**6.82e-07**

Table B.77: Result Kruskal-Wallis Test for E Medial

MED-S1-E	Kruskal-Wallis chi-squared	df	p-value
	15.7001	2	**0.0004**

Table B.78: Information Tukey HSD test for E Medial

Group	Diff	Lwr	upr	p adj
B-A	-2.76E+04	-42540.81	-12743.48	**0.0002055**
C-A	-2.57E+04	-40245.01	-11102.65	**0.0003947**
C-B	1.97E+03	-12930.35	16866.97	0.9436591

Table B.79: Result Shapiro-Wilk test for 1 mm Posterior Beam

Pos-S1-1mm	K-Initial	K-Slope	K-Max	J-Initial	J-Slope	J	E
No. of Data	12	12	12	12	12	12	12
Mean	0.3487	0.0287	5.3763	-0.2376	0.0057	0.8808	35033.9167
Std. Dev	0.9621	0.0129	1.3716	0.1931	0.0022	0.2960	14999.4367
W-statistic	0.9700	0.7978	0.8588	0.8772	0.8536	0.9902	0.7405
P(W)	0.9104	**0.0089**	**0.0472**	0.0807	**0.0407**	0.9998	**0.0021**

Table B.80: Improved Result Shapiro-Wilk by removing outliers for 1 mm Posterior Beam

Pos-S1-1 mm	K-Slope	K-Max	J-Slope	E
No. of Data	11	11	9	11
Mean	0.0255	5.0936	0.0046	31151.0000
Std. Dev	0.0069	1.0073	0.0008	6961.6420
W-statistic	0.9438	0.8706	0.9117	0.9393
p(W)	0.5663	0.0789	0.3276	0.5121

Table B.81: Result Shapiro-Wilk test for 1.7 mm Posterior Beam

Pos-S1-1.7mm	**K-Initial**	**K-Slope**	**K-Max**	**J-Initial**	**J-Slope**	**J**	**E**
No. of Data	12	12	12	12	12	12	12
Mean	-0.1314	0.0232	6.2006	-0.3726	0.0055	1.1581	35081.2500
Std. Dev	1.7815	0.0145	3.3321	0.4274	0.0036	0.6720	14926.3365
W-statistic	0.9361	0.8735	0.8330	0.9340	0.9229	0.9210	0.9088
P(W)	0.4492	0.0724	**0.0228**	0.4245	0.3113	0.2943	0.2059

Table B.82: Improved Result Shapiro-Wilk by removing outliers for 1.7 mm Posterior Beam

Pos-S1-1.7 mm	**K-Max**
No. of Data	11
Mean	5.5292
Std. Dev	2.5028
W-statistic	0.8575
p(W)	0.0534

Table B.83: Result Shapiro-Wilk test for 3 mm Posterior Beam

Pos-S1-3mm	**K-Initial**	**K-Slope**	**K-Max**	**J-Initial**	**J-Slope**	**J**	**E**
No. of Data	12	12	12	12	12	12	12
Mean	-1.0892	0.0187	8.0383	-0.6728	0.0047	1.8528	35981.7500
Std. Dev	1.3997	0.0073	2.7308	0.4381	0.0019	1.0044	13595.1368
W-statistic	0.8286	0.9093	0.9274	0.8435	0.9034	0.8229	0.9407
P(W)	**0.0202**	0.2093	0.3536	**0.0306**	0.1757	**0.0173**	0.5067

Table B.84: Improved Result Shapiro-Wilk by removing outliers for 3 mm Posterior Beam

Pos-S1-3 mm	**K-Initial**	**J-Initial**	**J**
No. of Data	9	9	11
Mean	-0.9876	-0.4552	1.6079
Std. Dev	1.2090	0.2093	0.5638
W-statistic	0.8602	0.8559	0.9672
p(W)	0.0964	0.0864	0.8566

Table B.85: Result Bartlett Test for K-Initial Posterior

POS-S1-K-Initial	**Bartletts K-squared**	**df**	**p-value**
	4.0669	2	0.1309

Table B.86: Result ANOVA Test for K-Initial Posterior

Groups	**Count**	**Sum**	**Average**	**Variance**		
K-Initial 1 mm	12	4.184453	0.348704	0.925718		
K-Initial 1.7 mm	12	-1.57712	-0.13143	3.173915		
K-Initial 3 mm	9	-8.8886	-0.98762	1.461669		
ANOVA						
Source of Variation	**SS**	**df**	**MS**	**F**	**P-value**	**F crit**
Between Groups	9.249409	2	4.624705	2.443085	0.103997	3.31583
Within Groups	56.78932	30	1.892977			
Total	66.03873	32				

Table B.87: Result Bartlett Test for K-Slope Posterior

ANT-S1-K-Slope	**Bartletts K-squared**	**df**	**p-value**
	7.6946	2	**0.02134**

Table B.88: Result Kruskal-Wallis Test for K-Slope Posterior

POS-S1-K-Slope	Kruskal-Wallis chi-squared	df	p-value
	3.8804	2	0.1437

Table B.89: Result Bartlett Test for K-Max Posterior

POS-S1-K-Max	Bartletts K-squared	df	p-value
	8.8778	2	**0.0118**

Table B.90: Result Kruskal-Wallis Test for K-Max Posterior

POS-S1-K-Max	Kruskal-Wallis chi-squared	df	p-value
	9.6093	2	**0.00819**

Table B.91: Information Tukey HSD test for K-Initial Posterior

Group	Diff	Lwr	upr	p adj
B-A	-0.4801311	-1.864851	0.9045884	0.6723973
C-A	-1.3363268	-2.831995	0.1593411	0.08703
C-B	-0.8561958	-2.351864	0.6394722	0.348006

Table B.92: Information Tukey HSD test for K-Slope Posterior

Group	Diff	Lwr	upr	p adj
B-A	-0.002305023	-0.01285088	0.008240838	0.8537081
C-A	-0.006875606	-0.01742147	0.003670254	0.2593977
C-B	-0.004570583	-0.01488464	0.005743471	0.5277133

Table B.93: Information Tukey HSD test for K-Max Posterior

Group	Diff	Lwr	upr	p adj
B-A	0.4356182	-1.9096631	2.780899	0.8915986
C-A	2.9446977	0.6487964	5.240599	**0.0096369**
C-B	2.5090795	0.2131782	4.804981	**0.0298505**

Table B.94: Result Bartlett Test for J-Initial Posterior

POS-S1-J-Initial	Bartletts K-squared	df	p-value
	8.0631	2	**0.01775**

Table B.95: Result Kruskal-Wallis Test for J-Initial Posterior

POS-S1-J-Initial	Kruskal-Wallis chi-squared	df	p-value
	3.5713	2	0.1677

Table B.96: Result Bartlett Test for J-Slope Posterior

POS-S1-J-Slope	Bartletts K-squared	df	p-value
	7.5472	2	**0.02297**

Table B.97: Result Kruskal-Wallis Test for J-Slope Posterior

POS-S1-J-Slope	Kruskal-Wallis chi-squared	df	p-value
	0.88613	2	0.6421

Table B.98: Result Bartlett Test for J Posterior

POS -S1-J	Bartletts K-squared	df	p-value
	6.5128	2	**0.03853**

Table B.99: Result Kruskal-Wallis Test for J Posterior

POS-S1-J	Kruskal-Wallis chi-squared	df	p-value
	9.5629	2	**0.008384**

Table B.100: Information Tukey HSD test for J-Initial Posterior

Group	Diff	Lwr	upr	p adj
B-A	-0.13500442	-0.4408244	0.1708156	0.5285607
C-A	-0.21756208	-0.5478855	0.1127613	0.2514726
C-B	-0.08255767	-0.412881	0.2477657	0.8124643

Table B.101: Information Tukey HSD test for J-Slope Posterior

Group	Diff	Lwr	upr	p adj
B-A	0.00025448	-0.002396216	0.002905177	0.9698122
C-A	-0.000598803	-0.003249499	0.002051893	0.8445998
C-B	-0.000853283	-0.003445716	0.001739149	0.7003506

Table B.102: Information Tukey HSD test for J Posterior

Group	Diff	Lwr	upr	p adj
B-A	0.2772783	-0.2579891	0.8125458	0.4204253
C-A	0.7270834	0.17978599	1.2743808	**0.0071723**
C-B	0.4498051	-0.09749234	0.9971025	0.123794

Table B.103: Result Bartlett Test for E Posterior

POS-S1-E	Bartletts K-squared	df	p-value
	5.523	2	0.0632

Table B.104: Result ANOVA Test for E Posterior

Groups	Count	Sum	Average	Variance		
E 1mm	11	342661	31151	48464459		
E 1.7 mm	12	420975	35081.25	2.23E+08		
E 3mm	12	431781	35981.75	1.85E+08		
ANOVA						
Source of Variation	**SS**	**Df**	**MS**	**F**	**P-value**	**F crit**
Between Groups	1.50E+08	2	74801815	0.481767	0.622099	3.294537
Within Groups	4.97E+09	32	1.55E+08			
Total	5.12E+09	34				

Table B.105: Information Tukey HSD test for E Posterior

Group	**Diff**	**Lwr**	**upr**	**p adj**
B-A	3930.25	-8851.357	16711.86	0.7324583
C-A	4830.75	-7950.857	17612.36	0.6263934
C-B	900.5	-11600.159	13401.16	0.9828823

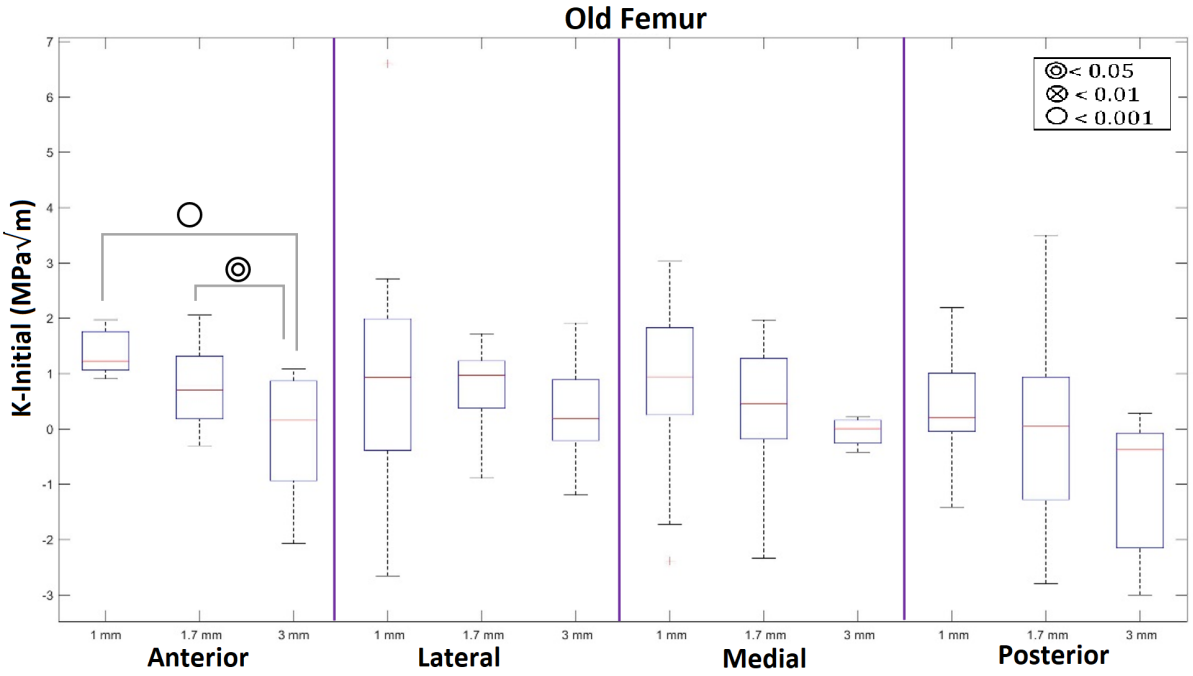

Figure B.1: Boxplot K-Initial for old femur (11-year-old) with significant between beam sizes labelled in the legend

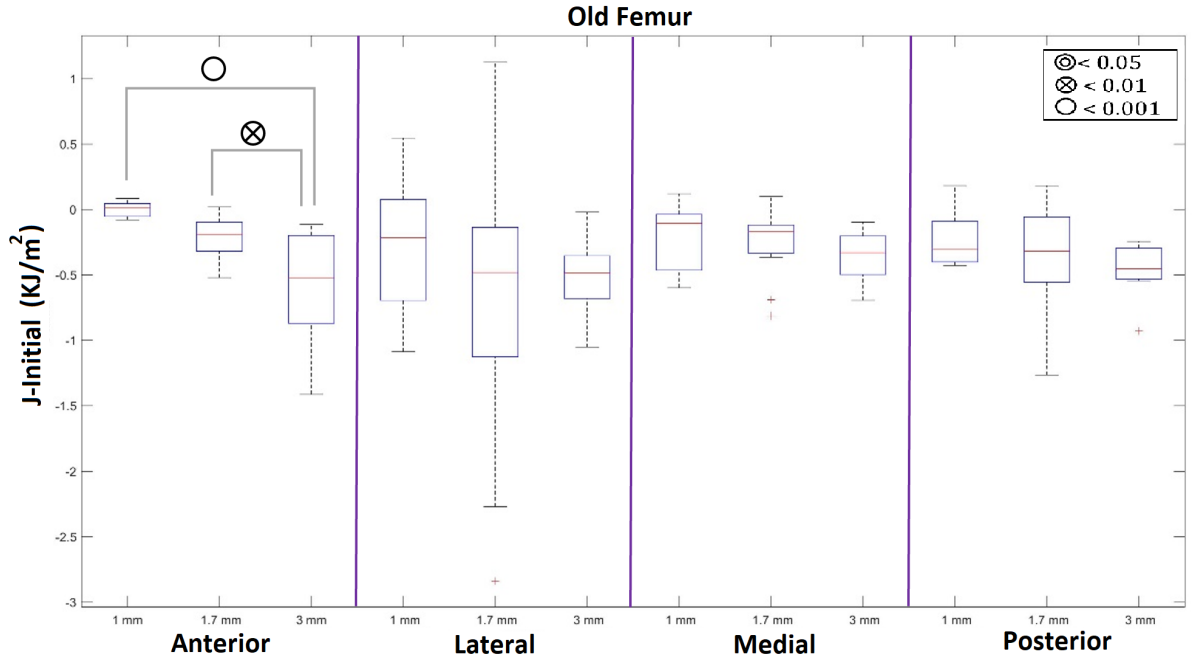

Figure B.2: Boxplot J-Initial for old femur (11-year-old) with significant between beam sizes labelled in the legend

B.2 Young Equine Femur

Table B.106: Result Shapiro-Wilk test for 1 mm Anterior Beam

Ant-S2-1mm	K-Initial	K-Slope	K-Max	J-Initial	J-Slope	J	E
No. of Data	12	12	12	12	12	12	12
Mean	0.3187	0.0526	7.0834	-0.2155	0.0095	1.0448	56632.0833
Std. Dev	3.5063	0.0564	3.1909	0.5381	0.0082	0.7008	3971.0587
W-statistic	0.8208	0.5951	0.9607	0.8888	0.8008	0.9175	0.8207
P(W)	**0.0163**	**9.76254e-05**	0.7936	0.1138	0.0096	0.2657	**0.0163**

Table B.107: Improved Result Shapiro-Wilk by removing outliers for 1 mm Anterior Beam

Ant-S2-1 mm	K-Initial	K-Slope	E
No. of Data	11	11	11
Mean	1.1299	0.0369	50871.3636
Std. Dev	2.1994	0.0161	13929.0722
W-statistic	0.8981	0.9776	0.9394
p(W)	0.1750	0.9515	0.5139

Table B.108: Result Shapiro-Wilk test for 1.7 mm Anterior Beam

Ant-S2-1.7mm	K-Initial	K-Slope	K-Max	J-Initial	J-Slope	J	E
No. of Data	12	12	12	12	12	12	12
Mean	-1.2348	0.0477	13.9960	-1.3285	0.0182	4.5051	42969.9167
Std. Dev	4.7995	0.0221	4.8706	2.5032	0.0116	2.2179	11085.3338
W-statistic	0.7500	0.9822	0.9589	0.8091	0.9674	0.9354	0.9913
P(W)	**0.0027**	0.9910	0.7681	**0.0119**	0.8818	0.4415	0.9999

Table B.109: Improved Result Shapiro-Wilk by removing outliers for 1.7 mm Anterior Beam

Ant-S2-1.7 mm	**K-Initial**	**J-Initial**
No. of Data	11	11
Mean	-2.4604	-1.9482
Std. Dev	2.3474	1.3504
W-statistic	0.8862	0.9028
p(W)	0.1246	0.2000

Table B.110: Result Shapiro-Wilk test for 3 mm Anterior Beam

Ant-S2-3mm	**K-Initial**	**K-Slope**	**K-Max**	**J-Initial**	**J-Slope**	**J**	**E**
No. of Data	12	12	12	12	12	12	12
Mean	-0.1979	0.0322	12.4024	-1.1336	0.0144	4.6304	29332.6667
Std. Dev	1.5355	0.0115	3.6181	0.8597	0.0049	1.5173	7126.7905
W-statistic	0.9252	0.8993	0.9240	0.9662	0.9559	0.9082	0.9810
P(W)	0.3317	0.1555	0.3204	0.8669	0.7237	0.2023	0.9874

Table B.111: Result Bartlett Test for K-Initial Anterior

ANT-S2-K-Initial	**Bartletts K-squared**	**df**	**p-value**
	1.9505	2	0.3771

Table B.112: Result ANOVA Test for K-Initial Anterior

Groups	**Count**	**Sum**	**Average**	**Variance**		
K-Initial 1 mm	11	12.42878	1.129889	4.837563		
K-Initial 1.7 mm	11	-27.0648	-2.46043	5.510251		
K-Initial 3 mm	12	-2.37508	-0.19792	2.357838		
ANOVA						
Source of Variation	**SS**	**df**	**MS**	**F**	**P-value**	**F crit**
Between Groups	72.59322	2	36.29661	8.694514	**0.001006**	3.304817
Within Groups	129.4144	31	4.174656			
Total	202.0076	33				

Table B.113: Result Bartlett Test for K-Slope Anterior

ANT-S2-K-Slope	**Bartletts K-squared**	**Df**	**p-value**
	4.3299	2	0.1148

Table B.114: Result ANOVA Test for K-Slope Anterior

Groups	**Count**	**Sum**	**Average**	**Variance**		
K-Slope 1 mm	11	0.406243	0.036931	0.000259		
K-Slope 1.7 mm	12	0.572	0.047667	0.00049		
K-Slope 3 mm	12	0.386744	0.032229	0.000133		
ANOVA						
Source of Variation	**SS**	**df**	**MS**	**F**	**P-value**	**F crit**
Between Groups	0.001499	2	0.000749	2.542999	0.094415	3.294537
Within Groups	0.009429	32	0.000295			
Total	0.010928	34				

Table B.115: Result Bartlett Test for K-Max Anterior

ANT-S2-K-Max	**Bartletts K-squared**	**df**	**p-value**
	2.0655	2	0.356

Table B.116: Result ANOVA Test for K-Max Anterior

Groups	**Count**	**Sum**	**Average**	**Variance**		
K-Max 1 mm	12	85.0014	7.08345	10.18202		
K-Max 1.7 mm	12	148.8289	12.40241	13.09039		
K-Max 3 mm	12	167.9521	13.99601	23.72287		
ANOVA						
Source of Variation	**SS**	**df**	**MS**	**F**	**P-value**	**F crit**
Between Groups	314.4574	2	157.2287	10.03688	**0.000394**	3.284918
Within Groups	516.948	33	15.66509			
Total	831.4053	35				

Table B.117: Information Tukey HSD test for K-Initial Anterior

Group	**Diff**	**Lwr**	**upr**	**p adj**
B-A	-3.590323	-5.7345656	-1.44608	**0.0007427**
C-A	-1.327813	-3.4269086	0.771283	0.2791964
C-B	2.26251	0.1634141	4.361606	**0.0325044**

Table B.118: Information Tukey HSD test for K-Slope Anterior

Group	**Diff**	**Lwr**	**upr**	**p adj**
B-A	0.010735466	-0.006872381	0.028343312	0.3051798
C-A	-0.004702542	-0.022310389	0.012905304	0.7901745
C-B	-0.015438008	-0.032658822	0.001782805	0.0859551

Table B.119: Information Tukey HSD test for K-Max Anterior

Group	**Diff**	**Lwr**	**upr**	**p adj**
B-A	5.318958	1.354088	9.283829	**0.006546**
C-A	6.912558	2.947688	10.877429	**0.0004358**
C-B	1.5936	-2.371271	5.558471	0.5905728

Table B.120: Result Bartlett Test for J-Initial Anterior

ANT-S2-J-Initail	Bartletts K-squared	df	p-value
	8.0677	2	**0.0177**

Table B.121: Result Kruskal-Wallis Test for J-Initial Anterior

ANT-S2-J-Initial	Kruskal-Wallis chi-squared	df	p-value
	14.3344	2	**0.0008**

Table B.122: Result Bartlett Test for J-Slope Anterior

ANT-S2-J-Slope	Bartletts K-squared	df	p-value
	7.105	2	**0.0286**

Table B.123: Result ANOVA Test for J-Slope Anterior

ANT-S2-J-Slope	ANOVA F-Value	df	p-value
	8.0315	2	**0.018**

Table B.124: Result Bartlett Test for J Anterior

ANT-S2-J	Bartletts K-squared	df	p-value
	11.8078	2	**0.0027**

Table B.125: Result Kruskal-Wallis Test for J Anterior

ANT-S2-J	Kruskal-Wallis chi-squared	df	p-value
	20.7583	2	**3.11e-05**

Table B.126: Information Tukey HSD test for J-Initial Anterior

Group	Diff	Lwr	upr	p adj
B-A	-1.7326971	-2.7184452	-0.74694898	**0.0004065**
C-A	-0.9181012	-1.8821818	0.04597949	0.0644898
C-B	0.8145959	-0.1711522	1.800344	0.1211744

Table B.127: Information Tukey HSD test for J-Slope Anterior

Group	Diff	Lwr	upr	p adj
B-A	0.008705674	1.63e-05	0.01739506	**0.049493**
C-A	0.004961616	-3.73e-03	0.013651	0.3519685
C-B	-0.003744058	-1.24e-02	0.00494533	0.5468078

Table B.128: Information Tukey HSD test for J Anterior

Group	Diff	Lwr	upr	p adj
B-A	3.4602354	1.854026	5.066445	**0.0000232**
C-A	3.5855938	1.979384	5.191804	**0.0000132**
C-B	0.1253583	-1.480851	1.731568	0.9799965

Table B.129: Result Bartlett Test for E Anterior

ANT-S2-E	Bartletts K-squared	df	p-value
	4.3003	2	0.1165

Table B.130: Result ANOVA Test for E Anterior

ANT-S2-E	ANOVA F-value	df	p-value
	11.4277	2	**0.0002**

Table B.131: Information Tukey HSD test for E Anterior

Group	Diff	Lwr	upr	p adj
B-A	-7901.447	-19153.67	3350.777	0.2113753
C-A	-21538.697	-32790.92	-10286.473	**0.0001358**
C-B	-13637.25	-24642.14	-2632.358	**0.0125106**

Table B.132: Result Shapiro-Wilk test for 1 mm Lateral Beam

Lat-S2-1mm	K-Initial	K-Slope	K-Max	J-Initial	J-Slope	J	E
No. of Data	12	12	12	12	12	12	12
Mean	0.8336	0.0354	5.4569	-0.1522	0.0069	0.7917	45155.0833
Std. Dev	1.0159	0.0221	1.9347	0.2371	0.0055	0.5393	11413.8967
W-statistic	0.9704	0.8924	0.9147	0.8352	0.8226	0.9022	0.9383
P(W)	0.9149	0.1265	0.2450	**0.0242**	**0.0171**	0.1693	0.4757

Table B.133: Improved Result Shapiro-Wilk by removing outliers for 1 mm Lateral Beam

Lat-S2-1 mm	J-Initial	J-Slope
No. of Data	10	11
Mean	-0.0706	0.0057
Std. Dev	0.1422	0.0038
W-statistic	0.8461	0.8677
p(W)	0.0522	0.0723

Table B.134: Result Shapiro-Wilk test for 1.7 mm Lateral Beam

Lat-S2-1.7mm	K-Initial	K-Slope	K-Max	J-Initial	J-Slope	J	E
No. of Data	12	12	12	12	12	12	12
Mean	-0.2905	0.0414	12.9726	-0.7640	0.0120	3.1891	54410.0833
Std. Dev	3.1984	0.0238	4.1506	0.8048	0.0056	1.5116	25987.5891
W-statistic	0.8802	0.7748	0.8835	0.8589	0.8977	0.726 1	0.8096
P(W)	0.0881	**0.0049**	0.0973	**0.0474**	0.1483	**0.0015**	**0.0121**

Table B.135: Improved Result Shapiro-Wilk by removing outliers for 1.7 mm Lateral Beam

Lat-S2-1.7 mm	**K-Slope**	**J-Initial**	**J**	**E**
No. of Data	11	11	6	11
Mean	0.0354	-0.9543	2.1900	47992.8182
Std. Dev	0.0120	0.4839	0.1186	14117.2664
W-statistic	0.9654	0.9692	0.9713	0.9611
p(W)	0.8365	0.8782	0.9010	0.7859

Table B.136: Result Shapiro-Wilk test for 3 mm Lateral Beam

Lat-S2-3mm	**K-Initial**	**K-Slope**	**K-Max**	**J-Initial**	**J-Slope**	**J**	**E**
No. of Data	12	12	12	12	12	12	12
Mean	-2584.7654	18.4557	6736.2676	-0.7036	0.0079	2.6867	112.67e+7
Std. Dev	8954.7767	63.8574	23303.2424	0.5693	0.0029	1.3251	387.104e+7
W-statistic	0.3271	0.3270	0.3270	0.9271	0.9312	0.8937	0.3269
P(W)	**1.21e-06**	**1.209e-06**	**1.209e-06**	0.3501	0.3925	0.1316	**1.207e-06**

Table B.137: Improved Result Shapiro-Wilk by removing outliers for 3 mm Lateral Beam

Lat-S2-3 mm	**K-Initial**	**K-Slope**	**K-Max**	**E**
No. of Data	11	11	11	11
Mean	0.2559	0.0216	9.2011	31045.0909
Std. Dev	1.6155	0.0067	3.0246	3620.4806
W-statistic	0.9690	0.9353	0.8881	0.9354
p(W)	0.8760	0.4672	0.1315	0.4678

Table B.138: Result Bartlett Test for K-Initial Lateral

LAT-S2-K-Initial	**Bartletts K-squared**	**df**	**p-value**
	13.3556	2	**0.0013**

Table B.139: Result Kruskal-Wallis Test for K-Initial Lateral

LAT-S2-K-Initial	Kruskal-Wallis chi-squared	df	p-value
	3.9885	2	0.1361

Table B.140: Result Bartlett Test for K-Slope Lateral

LAT-S2-K-Slope	Bartletts K-squared	df	p-value
	12.8493	2	**0.0016**

Table B.141: Result Kruskal-Wallis Test for K-Slope Lateral

LAT-S2-K-Slope	Kruskal-Wallis chi-squared	df	p-value
	8.2868	2	**0.0159**

Table B.142: Result Bartlett Test for K-Max Lateral

LAT-S2-K-Max	Bartletts K-squared	df	p-value
	5.6939	2	0.058

Table B.143: Result ANOVA Test for K-Max Lateral

Groups	Count	Sum	Average	Variance		
K-Max 1 mm	12	65.4824	5.456867	3.743064		
K-Max 1.7 mm	12	155.6718	12.97265	17.22743		
K-Max 3 mm	11	101.2118	9.201073	9.147905		
ANOVA						
Source of Variation	**SS**	**df**	**MS**	**F**	**P-value**	**F crit**
Between Groups	338.9234	2	169.4617	16.83284	**1.01e-05**	3.294537
Within Groups	322.1544	32	10.06733			
Total	661.0779	34				

Table B.144: Information Tukey HSD Test for K-Initial Lateral

Group	Diff	Lwr	upr	p adj
B-A	-1.1240533	-3.295916	1.047809	0.421061
C-A	-0.5776279	-2.798303	1.643047	0.7997257
C-B	0.5464255	-1.674249	2.7671	0.8186008

Table B.145: Information Tukey HSD Test for K-Slope Lateral

Group	Diff	Lwr	upr	p adj
B-A	-2.22e-05	-0.01573148	0.015687135	0.9999933
C-A	-1.38e-02	-0.02948621	0.001932408	0.0946136
C-B	-1.38e-02	-0.02980191	0.002292454	0.1043069

Table B.146: Information Tukey HSD Test for K-Max Lateral

Group	Diff	Lwr	upr	p adj
B-A	7.515783	4.3326686	10.698898	**0.0000057**
C-A	3.744206	0.4895518	6.99886	**0.0213318**
C-B	-3.771577	-7.0262316	-0.516923	**0.0202987**

Table B.147: Result Bartlett Test for J-Initial Lateral

LAT-S2-J-Initial	Bartletts K-squared	df	p-value
	13.5676	2	**0.0011**

Table B.148: Result Kruskal-Wallis Test for J-Initial Lateral

LAT-S2-J-Initial	Kruskal-Wallis chi-squared	df	p-value
	15.8347	2	**0.0004**

Table B.149: Result Bartlett Test for J-Slope Lateral

LAT-S2-J-Slope	Bartletts K-squared	df	p-value
	4.6083	2	0.0998

Table B.150: Result ANOVA Test for J-Slope Lateral

Groups	Count	Sum	Average	Variance		
J-Slope 1 mm	11	0.062728	0.005703	1.42e-05		
J-Slope 1.7 mm	12	0.144179	0.012015	3.13e-05		
J-Slope 3 mm	12	0.095004	0.007917	8.44e-06		
ANOVA						
Source of Variation	**SS**	**df**	**MS**	**F**	**P-value**	**F crit**
Between Groups	0.000238	2	0.000119	6.569278	**0.00407**	3.294537
Within Groups	0.000579	32	1.81e-05			
Total	0.000817	34				

Table B.151: Result Bartlett Test for J Lateral

LAT-S2-J	Bartletts K-squared	df	p-value
	22.5948	2	**1.24e-05**

Table B.152: Result Kruskal-Wallis Test for J Lateral

LAT-S2-J	Kruskal-Wallis chi-squared	df	p-value
	17.2118	2	**0.0002**

Table B.153: Information Tukey HSD Test for J-Initial Lateral

Group	Diff	Lwr	upr	p adj
B-A	-0.8837861	-1.3690917	-0.3984805	**0.0002817**
C-A	-0.6330359	-1.108615	-0.1574569	**0.0071854**
C-B	0.2507502	-0.2128878	0.7143881	0.388284

Table B.154: Information Tukey HSD Test for J-Slope Lateral

Group	Diff	Lwr	upr	p adj
B-A	0.006312352	0.001947851	0.010676853	**0.0033558**
C-A	0.002214469	-0.002150032	0.00657897	0.4350588
C-B	-0.004097883	-0.008366449	0.000170683	0.0619258

Table B.155: Information Tukey HSD Test for J Lateral

Group	Diff	Lwr	upr	p adj
B-A	1.3982867	0.2645085	2.532065	**0.0133739**
C-A	1.8949842	0.9692582	2.82071	**0.0000719**
C-B	0.4966975	-0.6370807	1.630476	0.5306036

Table B.156: Result Bartlett Test for E Lateral

LAT-S2-E	Bartletts K-squared	df	p-value
	14.167	2	**0.0008**

Table B.157: Result Kruskal-Wallis Test for E Lateral

LAT-S2-E	Kruskal-Wallis chi-squared	df	p-value
	12.9242	2	**0.0016**

Table B.158: Information Tukey HSD Test for E Lateral

Group	Diff	Lwr	upr	p adj
B-A	2837.735	-8167.238	13842.708	0.8022878
C-A	-14109.992	-25114.965	-3105.019	**0.0096633**
C-B	-16947.727	-28189.393	-5706.061	**0.0022762**

Table B.159: Result Shapiro-Wilk test for 1 mm Medial Beam

Med-S2-1mm	K-Initial	K-Slope	K-Max	J-Initial	J-Slope	J	E
No. of Data	12	12	12	12	12	12	12
Mean	0.9587	0.0418	5.7069	-0.1269	0.0086	0.8558	48570.7500
Std. Dev	2.6781	0.0307	2.9194	0.4821	0.0077	0.8469	16554.3930
W-statistic	0.7701	0.9114	0.8877	0.7227	0.8733	0.7571	0.9615
P(W)	**0.0044**	0.2225	0.1100	**0.0014**	0.0720	**0.0032**	0.8044

Table B.160: Improved Result Shapiro-Wilk by removing outliers for 1 mm Medial Beam

Med-S2-1 mm	K-Initial	J-Initial	J
No. of Data	8	10	8
Mean	1.5875	0.0695	0.6261
Std. Dev	0.3857	0.1322	0.3703
W-statistic	0.9374	0.9479	0.8302
p(W)	0.5856	0.6443	0.0597

Table B.161: Result Shapiro-Wilk test for 1.7 mm Medial Beam

Med-S2-1.7mm	K-Initial	K-Slope	K-Max	J-Initial	J-Slope	J	E
No. of Data	12	12	12	12	12	12	12
Mean	0.9377	0.0287	8.8517	-0.3701	0.0100	2.2735	36335.4167
Std. Dev	1.1998	0.0170	3.2836	0.4620	0.0079	1.2450	12809.1032
W-statistic	0.8724	0.8803	0.9086	0.7405	0.8378	0.9615	0.9613
P(W)	0.0701	0.0885	0.2050	**0.0021**	**0.0260**	0.8055	0.8029

Table B.162: Improved Result Shapiro-Wilk by removing outliers for 1.7 mm Medial Beam

Med-S2-1.7 mm	**J-Initial**	**J-Slope**
No. of Data	10	11
Mean	-0.1814	0.0081
Std. Dev	0.1518	0.0046
W-statistic	0.9376	0.9332
p(W)	0.5268	0.4438

Table B.163: Result Shapiro-Wilk test for 3 mm Medial Beam

Med-S2-3mm	**K-Initial**	**K-Slope**	**K-Max**	**J-Initial**	**J-Slope**	**J**	**E**
No. of Data	12	12	12	12	12	12	12
Mean	0.1909	0.0236	9.0035	-0.6692	0.0099	2.8271	28498.8333
Std. Dev	2.5035	0.0173	3.5901	0.8064	0.0091	1.6533	8145.9250
W-statistic	0.9125	0.7864	0.8969	0.9723	0.7434	0.9161	0.9340
P(W)	0.2294	**0.0066**	0.1448	0.9334	**0.0023**	0.2556	0.4240

Table B.164: Improved Result Shapiro-Wilk by removing outliers for 3 mm Medial Beam

Med-S2-3 mm	**K-Slope**	**J-Slope**
No. of Data	10	11
Mean	0.0168	0.0076
Std. Dev	0.0066	0.0048
W-statistic	0.9331	0.8563
p(W)	0.4790	0.0516

Table B.165: Result Bartlett Test for K-Initial Medial

MED-S2-K-Initial	**Bartletts K-squared**	**df**	**p-value**
	19.655	2	**5.40e-05**

Table B.166: Result Kruskal-Wallis Test for K-Initial Medial

MED-S2-K-Initial	Kruskal-Wallis chi-squared	df	p-value
	7.1894	2	**0.0275**

Table B.167: Result Bartlett Test for K-Slope Medial

MED-S2-K-Slope	Bartletts K-squared	df	p-value
	16.9369	2	**0.00021**

Table B.168: Result Kruskal-Wallis Test for K-Slope Medial

MED-S2-K-Slope	Kruskal-Wallis chi-squared	df	p-value
	5.9771	2	0.0504

Table B.169: Result Bartlett Test for K-Max Medial

MED-S2-K-Max	Bartletts K-squared	df	p-value
	0.4492	2	0.7989

Table B.170: Result ANOVA Test for K-Max Medial

Groups	Count	Sum	Average	Variance		
K-Max 1 mm	12	68.4823	5.706858	8.522818		
K-Max 1.7 mm	12	106.2204	8.8517	10.78209		
K-Max 3 mm	12	108.0421	9.003508	12.88869		
ANOVA						
Source of Variation	**SS**	**df**	**MS**	**F**	**P-value**	**F crit**
Between Groups	83.1239	2	41.56195	3.873002	**0.030837**	3.284918
Within Groups	354.1295	33	10.7312			
Total	437.2534	35				

Table B.171: Information Tukey HSD test for K-Initial Medial

Group	Diff	Lwr	Upr	p adj
B-A	-0.6497783	-2.588888	1.2893317	0.6892194
C-A	-1.3965679	-3.335678	0.5425422	0.1944679
C-B	-0.7467896	-2.481182	0.9876032	0.5439212

Table B.172: Information Tukey HSD test for K-Slope Medial

Group	Diff	Lwr	Upr	p adj
B-A	-0.01310563	-0.03440596	0.008194696	0.2982115
C-A	-0.02496348	-0.04730345	-0.002623506	**0.0259243**
C-B	-0.01185785	-0.03419782	0.010482127	0.402397

Table B.173: Information Tukey HSD test for K-Max Medial

Group	Diff	Lwr	upr	p adj
B-A	3.1448417	-0.13676598	6.426449	0.0625155
C-A	3.29665	0.01504235	6.578258	**0.0487681**
C-B	0.1518083	-3.12979932	3.433416	0.9929229

Table B.174: Result Bartlett Test for J-Initial Medial

MED-S2-J-Initial	Bartletts K-squared	df	p-value
	34.3446	2	**3.49e-08**

Table B.175: Result Kruskal-Wallis Test for J-Initial Medial

MED-S2-J-Initial	Kruskal-Wallis chi-squared	df	p-value
	11.7142	2	**0.0029**

Table B.176: Result Bartlett Test for J-Slope Medial

MED-S2-J-Slope	Bartletts K-squared	df	p-value
	3.6377	2	0.1622

Table B.177: Result ANOVA Test for J-Slope Medial

Groups	Count	Sum	Average	Variance		
J-Slope 1 mm	12	0.102949	0.008579	5.98e-05		
J-Slope 1.7 mm	11	0.089491	0.008136	2.08e-05		
J-Slope 3 mm	11	0.083393	0.007581	2.31e-05		
ANOVA						
Source of Variation	SS	**df**	**MS**	**F**	**P-value**	**F crit**
Between Groups	5.72e-06	2	2.86e-06	0.080822	0.922551	3.304817
Within Groups	0.001098	31	3.54e-05			
Total	0.001103	33				

Table B.178: Result Bartlett Test for J Medial

MED-S2-J	Bartletts K-squared	df	p-value
	12.1021	2	**0.0024**

Table B.179: Result Kruskal-Wallis Test for J Medial

MED-S2-J	Kruskal-Wallis chi-squared	df	p-value
	13.2562	2	**0.0013**

Table B.180: Information Tukey HSD test for J-Initial Medial

Group	Diff	Lwr	upr	p adj
B-A	-0.2508597	-0.8131921	0.3114726	0.5207067
C-A	-0.7387013	-1.2770936	-0.20030911	**0.0056174**
C-B	-0.4878416	-1.0262338	0.05055063	0.0815549

Table B.181: Information Tukey HSD test for J-Slope Medial

Group	Diff	Lwr	upr	p adj
B-A	-0.000443518	-0.00655683	0.005669794	0.9825866
C-A	-0.000997909	-0.007111221	0.005115403	0.9151189
C-B	-0.000554391	-0.006799187	0.005690405	0.9740472

Table B.182: Information Tukey HSD test for J Medial

Group	Diff	Lwr	upr	p adj
B-A	1.6474046	0.1960316	3.098778	**0.0235432**
C-A	2.2009888	0.7496158	3.652362	**0.0022281**
C-B	0.5535842	-0.7445633	1.851732	0.5501456

Table B.183: Result Bartlett Test for E Medial

MED-S2-E	Bartletts K-squared	df	p-value
	4.9278	2	0.0851

Table B.184: Result ANOVA Test for E Medial

Groups	Count	Sum	Average	Variance		
E 1 mm	12	582849	48570.75	2.74e+08		
E 1.7 mm	12	436025	36335.42	1.64e+08		
E 3 mm	12	341986	28498.83	66356093		
ANOVA						
Source of Variation	**SS**	**df**	**MS**	**F**	**P-value**	**F crit**
Between Groups	2.46e+09	2	1.23E+09	7.302578	**0.002367**	3.284918
Within Groups	5.55e+09	33	1.68E+08			
Total	8.01e+09	35				

Table B.185: Information Tukey HSD test for E Medial

Group	Diff	Lwr	upr	p adj
B-A	-12235.333	-25225.74	755.0716	0.0681585
C-A	-20071.917	-33062.32	-7081.5117	**0.0017103**
C-B	-7836.583	-20826.99	5153.8216	0.3132061

Table B.186: Result Shapiro-Wilk test for 1 mm Posterior Beam

Pos-S2-1mm	K-Initial	K-Slope	K-Max	J-Initial	J-Slope	J	E
No. of Data	12	12	12	12	12	12	12
Mean	-0.4168	0.0738	9.0664	-0.5953	0.0178	1.6589	54132.7500
Std. Dev	2.2743	0.0626	4.7160	0.7472	0.0172	1.1357	26287.3651
W-statistic	0.9042	0.8696	0.9155	0.9038	0.8270	0.8959	0.9661
P(W)	0.1795	0.0647	0.2511	0.1774	**0.0193**	0.1404	0.8662

Table B.187: Improved Result Shapiro-Wilk by removing outliers for 1 mm Posterior Beam

Pos-S2-1 mm	J-Slope
No. of Data	10
Mean	0.0113
Std. Dev	0.0088
W-statistic	0.9061
p(W)	0.2555

Table B.188: Result Shapiro-Wilk test for 1.7 mm Posterior Beam

Pos-S2-1.7mm	K-Initial	K-Slope	K-Max	J-Initial	J-Slope	J	E
No. of Data	12	12	12	12	12	12	12
Mean	-2.9433	0.0438	10.9239	-1.9728	0.0183	3.3757	38955.5000
Std. Dev	3.8396	0.0301	4.3786	1.8211	0.0192	2.1565	14436.9014
W-statistic	0.6947	0.8416	0.8983	0.6965	0.6814	0.8672	0.8482
P(W)	**0.0007**	**0.0290**	0.1506	**0.0008**	**0.0006**	0.0602	**0.0349**

Table B.189: Improved Result Shapiro-Wilk by removing outliers for 1.7 mm Posterior Beam

Pos-S2-1.7 mm	K-Initial	K-Slope	J-Initial	J-Slope	E
No. of Data	8	11	11	11	11
Mean	-0.8069	0.0369	-1.4864	0.0132	36061.6364
Std. Dev	0.3192	0.0191	0.7237	0.0083	10896.0468
W-statistic	0.9097	0.9245	0.9791	0.8902	0.8597
p(W)	0.3519	0.3581	0.9609	0.1400	0.0571

Table B.190: Result Shapiro-Wilk test for 3 mm Posterior Beam

Pos-S2-3mm	K-Initial	K-Slope	K-Max	J-Initial	J-Slope	J	E
No. of Data	12	12	12	12	12	12	12
Mean	-1.6073	0.0171	8.8589	-1.5440	0.0076	3.1841	26649.1667
Std. Dev	1.5315	0.0058	2.7898	1.0793	0.0034	1.6718	7276.1927
W-statistic	0.9881	0.9497	0.9689	0.9016	0.9382	0.9258	0.9606
P(W)	0.9992	0.6321	0.8984	0.1666	0.4755	0.3381	0.7924

Table B.191: Result Bartlett Test for K-Initial Posterior

POS-S2-K-Initial	Bartletts K-squared	df	p-value
	1.7116	2	0.4249

Table B.192: Result ANOVA Test for K-Initial Posterior

Groups	**Count**	**Sum**	**Average**	**Variance**		
K-Initial 1 mm	12	-5.00127	-0.41677	5.172425		
K-Initial 1.7 mm	11	-22.0012	-2.00011	4.472612		
K-Initial 3 mm	12	-19.2874	-1.60728	2.345408		
ANOVA						
Source of Variation	**SS**	**df**	**MS**	**F**	**P-value**	**F crit**
Between Groups	15.868	2	7.934	1.992493	0.152918	3.294537
Within Groups	127.4223	32	3.981946			
Total	143.2903	34				

Table B.193: Result Bartlett Test for K-Slope Posterior

POS-S2-K-Slope	**Bartletts K-squared**	**df**	**p-value**
	43.1546	2	**4.26e-10**

Table B.194: Result Kruskal-Wallis Test for K-Slope Posterior

POS-S2-K-Slope	**Kruskal-Wallis chi-squared**	**df**	**p-value**
	14.046	2	**0.0009**

Table B.195: Result Bartlett Test for K-Max Posterior

POS-S2-K-Max	**Bartletts K-squared**	**df**	**p-value**
	3.0055	2	0.2225

Table B.196: Result ANOVA Test for K-Max Posterior

Groups	**Count**	**Sum**	**Average**	**Variance**		
K-Max 1 mm	12	108.7965	9.066375	22.24064		
K-Max 1.7 mm	12	131.0874	10.92395	19.17238		
K-Max 3 mm	12	106.3072	8.858933	7.783049		
ANOVA						
Source of Variation	**SS**	**df**	**MS**	**F**	**P-value**	**F crit**
Between Groups	31.03164	2	15.51582	0.946162	0.398508	3.284918
Within Groups	541.1567	33	16.39869			
Total	572.1884	35				

Table B.197: Information Tukey HSD test for K-Initial Posterior

Group	**Diff**	**Lwr**	**upr**	**p adj**
B-A	-1.5833348	-3.630229	0.4635599	0.1548535
C-A	-1.1905117	-3.192414	0.8113908	0.3225958
C-B	0.3928231	-1.654072	2.4397178	0.885068

Table B.198: Information Tukey HSD test for K-Slope Posterior

Group	**Diff**	**Lwr**	**upr**	**p adj**
B-A	-0.03695569	-0.07630803	0.002396648	0.0690991
C-A	-0.05670338	-0.09519073	-0.018216037	**0.0028094**
C-B	-0.01974769	-0.05910003	0.019604646	0.4428048

Table B.199: Information Tukey HSD test for K-Max Posterior

Group	**Diff**	**Lwr**	**upr**	**p adj**
B-A	-2.0650167	-6.121663	5.914221	0.5066201
C-A	-0.2074417	-4.264088	3.849204	0.9913596
C-B	1.857575	-2.199071	1.991629	0.4334985

Table B.200: Result Bartlett Test for J-Initial Posterior

POS-S2-J-Initial	Bartletts K-squared	df	p-value
	2.1597	2	0.3396

Table B.201: Result ANOVA Test for J-Initial Posterior

Groups	Count	Sum	Average	Variance		
J-Initial 1 mm	12	-7.14379	-0.59532	0.55832		
J-Initial 1.7 mm	11	-16.3499	-1.48635	0.52373		
J-Initial 3 mm	12	-18.5276	-1.54396	1.164883		
ANOVA						
Source of Variation	**SS**	**df**	**MS**	**F**	**P-value**	**F crit**
Between Groups	6.709395	2	3.354697	4.437333	**0.019913**	3.294537
Within Groups	24.19253	32	0.756017			
Total	30.90192	34				

Table B.202: Result Bartlett Test for J-Slope Posterior

POS-S2-J-Slope	Bartletts K-squared	df	p-value
	8.7157	2	**0.0128**

Table B.203: Result Kruskal-Wallis Test for J-Slope Posterior

POS-S2-J-Slope	Kruskal-Wallis chi-squared	df	p-value
	4.0783	2	0.1301

Table B.204: Result Bartlett Test for J Posterior

POS-S2-J	Bartletts K-squared	df	p-value
	4.0914	2	0.1293

Table B.205: Result ANOVA Test for J Posterior

Groups	**Count**	**Sum**	**Average**	**Variance**		
J 1 mm	12	19.90727	1.658939	1.2898		
J 1.7 mm	12	40.50799	3.375666	4.650422		
J 3 mm	12	38.20884	3.18407	2.794992		
ANOVA						
Source of Variation	**SS**	**df**	**MS**	**F**	**P-value**	**F crit**
Between Groups	21.23953	2	10.61977	3.647226	**0.037062**	3.284918
Within Groups	96.08736	33	2.911738			
Total	117.3269	35				

Table B.206: Information Tukey HSD test for J-Initial Posterior

Group	**Diff**	**Lwr**	**upr**	**p adj**
B-A	-0.89103491	-1.7829293	0.000859492	0.0502617
C-A	-0.94864733	-1.8209373	-0.076357401	**0.0307182**
C-B	-0.05761242	-0.9495068	0.834281977	0.986211

Table B.207: Information Tukey HSD test for J-Slope Posterior

Group	**Diff**	**Lwr**	**upr**	**p adj**
B-A	0.001916767	-0.005707045	0.00954058	0.8104664
C-A	-0.003706602	-0.011177617	0.003764413	0.4491295
C-B	-0.005623369	-0.012906797	0.001660059	0.1552061

Table B.208: Information Tukey HSD test for J Posterior

Group	**Diff**	**Lwr**	**upr**	**p adj**
B-A	1.7167267	0.007346273	3.426107	**0.0488442**
C-A	1.5251308	-0.18424956	3.234511	0.0879276
C-B	-0.1915958	-0.18424956	1.517785	0.9592105

Table B.209: Result Bartlett Test for E Posterior

POS-S2-E	Bartletts K-squared	df	p-value
	17.6612	2	**0.0001**

Table B.210: Result Kruskal-Wallis Test for E Posterior

POS-S2-E	Kruskal-Wallis chi-squared	df	p-value
	12.4542	2	**0.002**

Table B.211: Information Tukey HSD test for E Posterior

Group	Diff	Lwr	upr	p adj
B-A	-18071.11	-35624.6	-517.6318	**0.0425516**
C-A	-27483.58	-44651.23	-10315.9394	**0.001195**
C-B	-9412.47	-26965.95	8141.0122	0.3959462

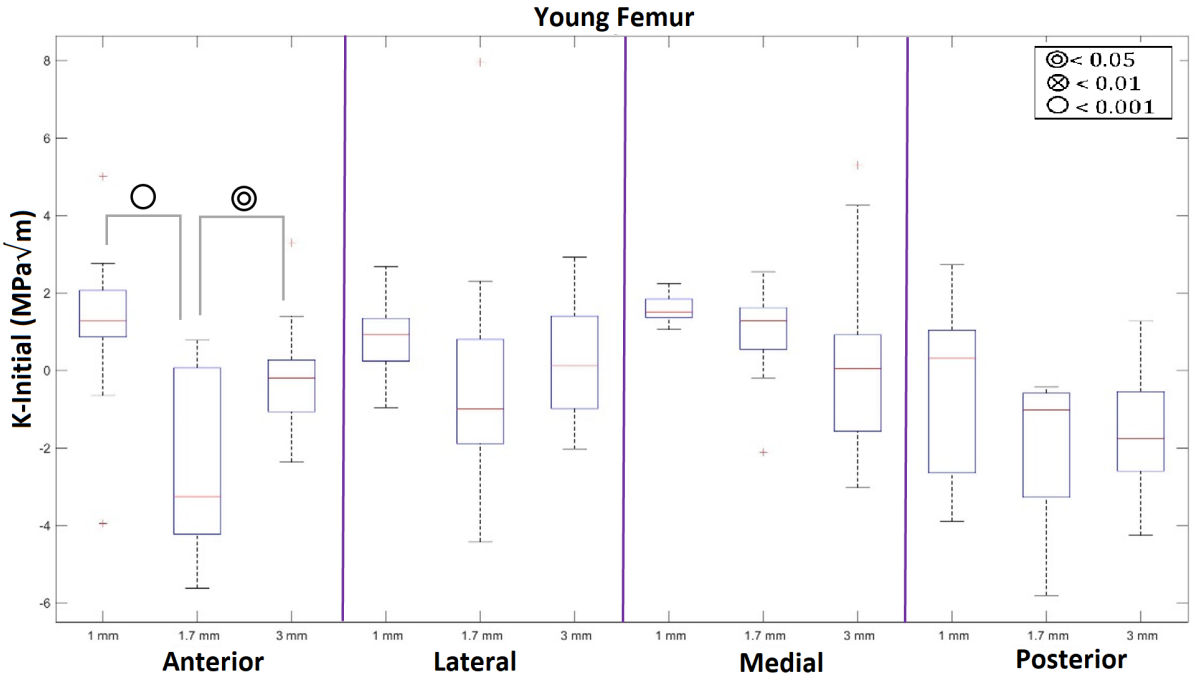

Figure B.3: Boxplot K-Initial for young femur (5-year-old) with significant between beam sizes labelled in the legend

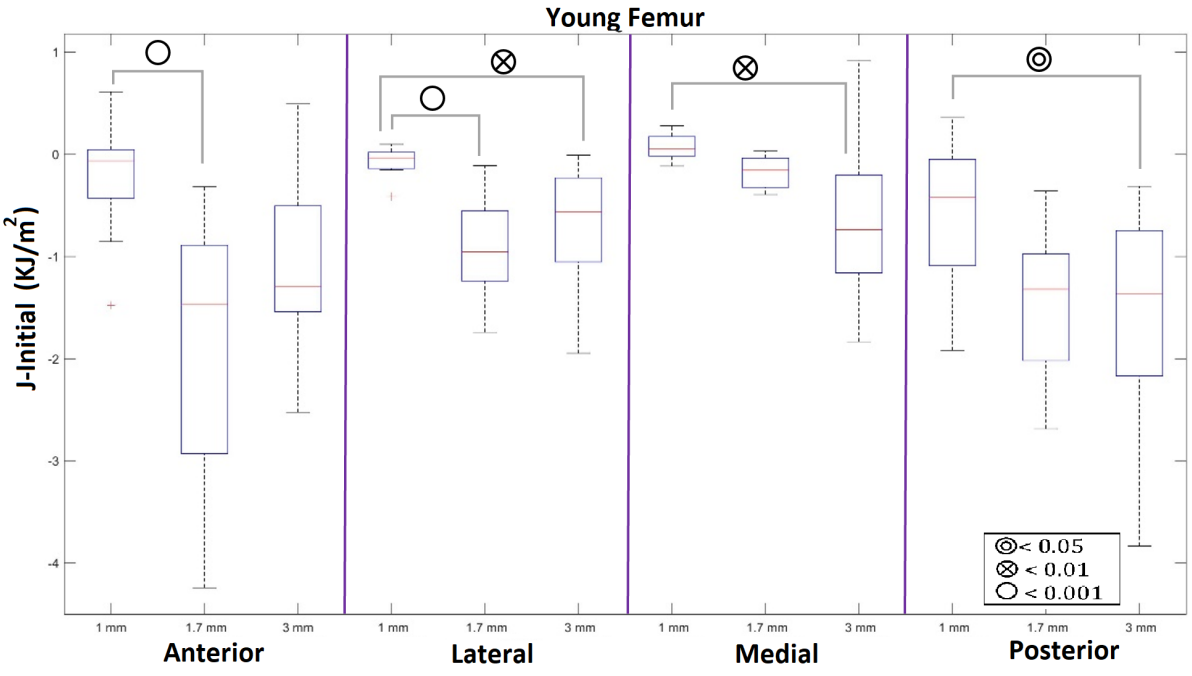

Figure B.4: Boxplot J-Initial for young femur (5-year-old) with significant between beam sizes labelled in the legend

B.3 Age and Anatomical Location Comparison

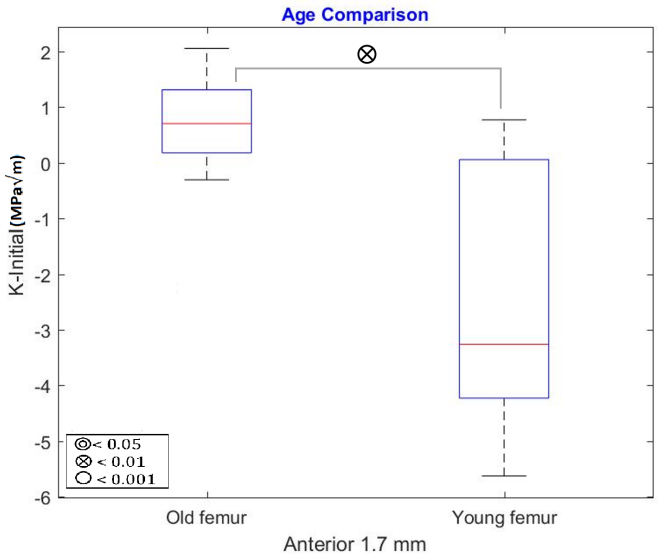

Figure B.5: Age comparison of K-Initial in the anterior of beam size 1.7 mm

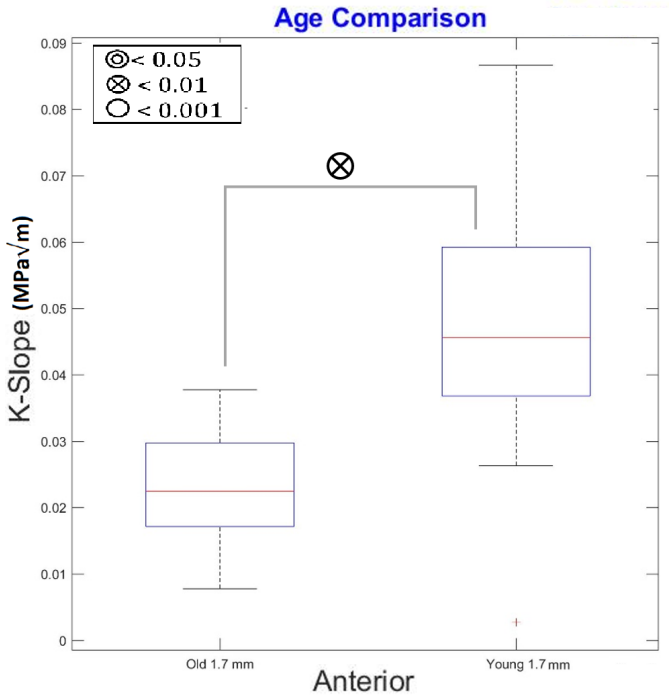

Figure B.6: Age comparison of K-Slope in the anterior of beam size 1.7 mm

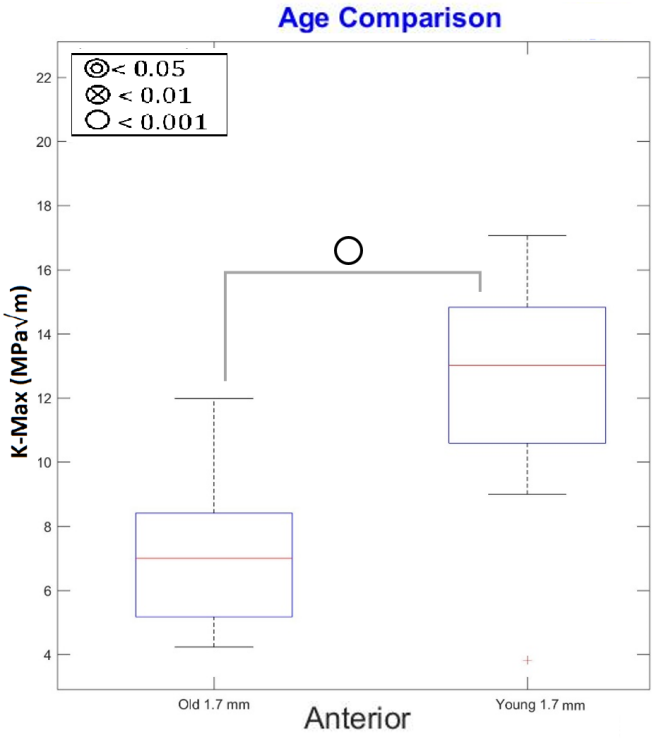

Figure B.7: Age comparison of K-Max in the anterior of beam size 1.7 mm

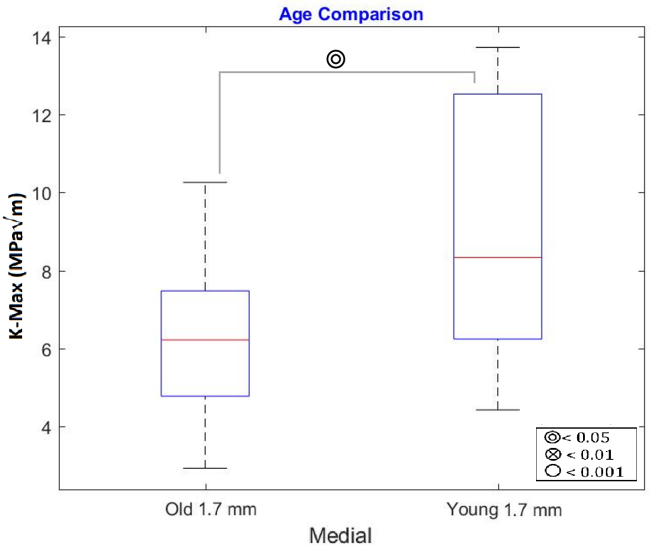

Figure B.8: Age comparison of K-Max in the Medial of beam size 1.7 mm

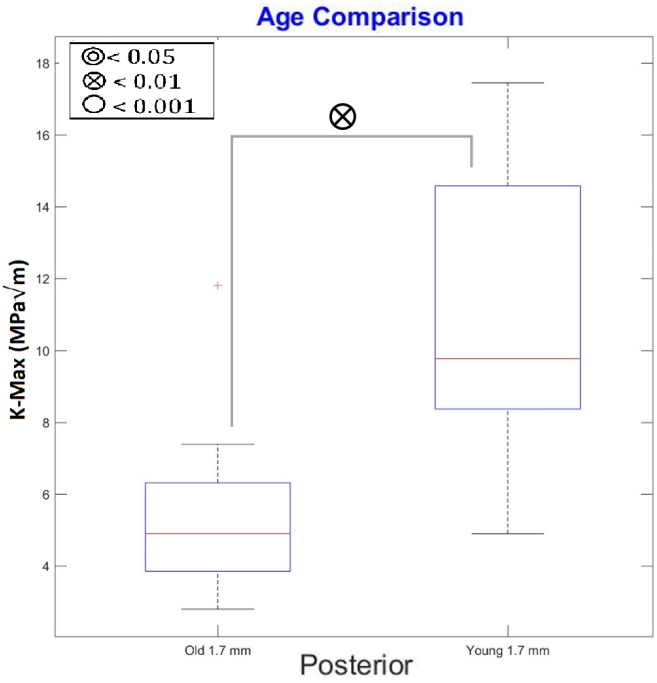

Figure B.9: Age comparison of K-Max in the posterior of beam size 1.7 mm

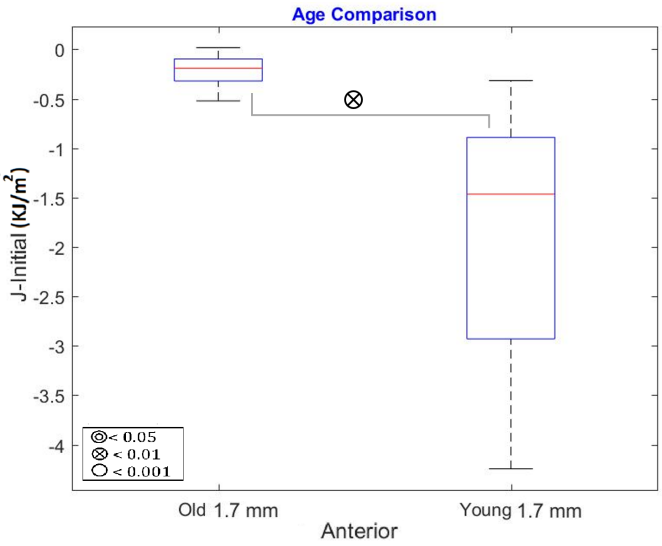

Figure B.10: Age comparison of J-Initial in the anterior of beam size 1.7 mm

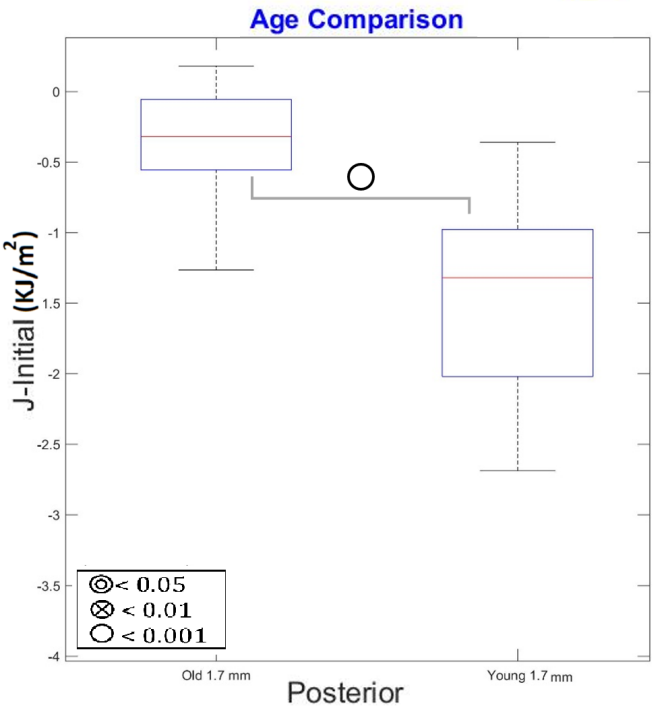

Figure B.11: Age comparison of J-Initial in the posterior of beam size 1.7 mm

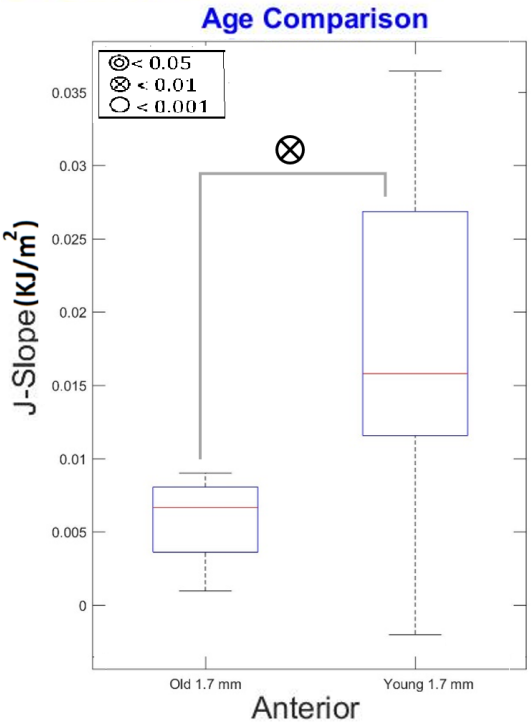

Figure B.12: Age comparison of J-Slope in the anterior of beam size 1.7 mm

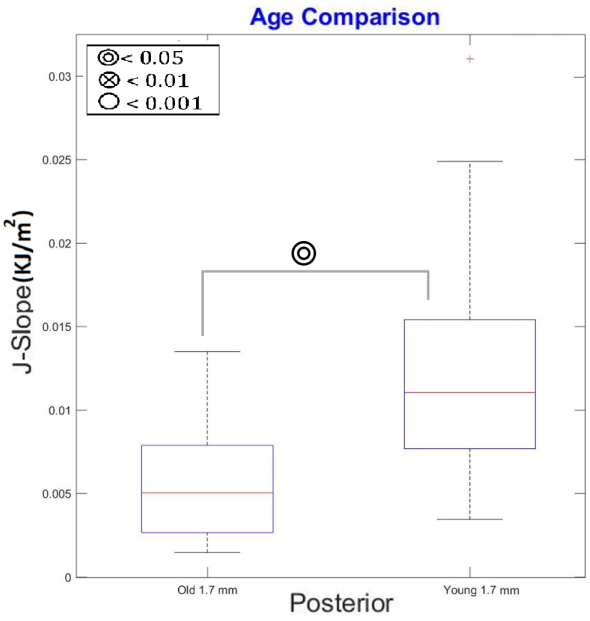

Figure B.13: Age comparison of J-Slope in the posterior of beam size 1.7 mm

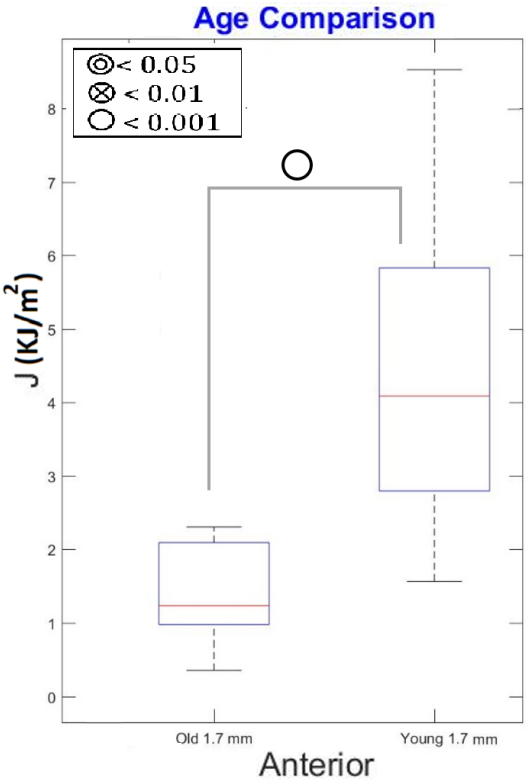

Figure B.14: Age comparison of J in the anterior of beam size 1.7 mm

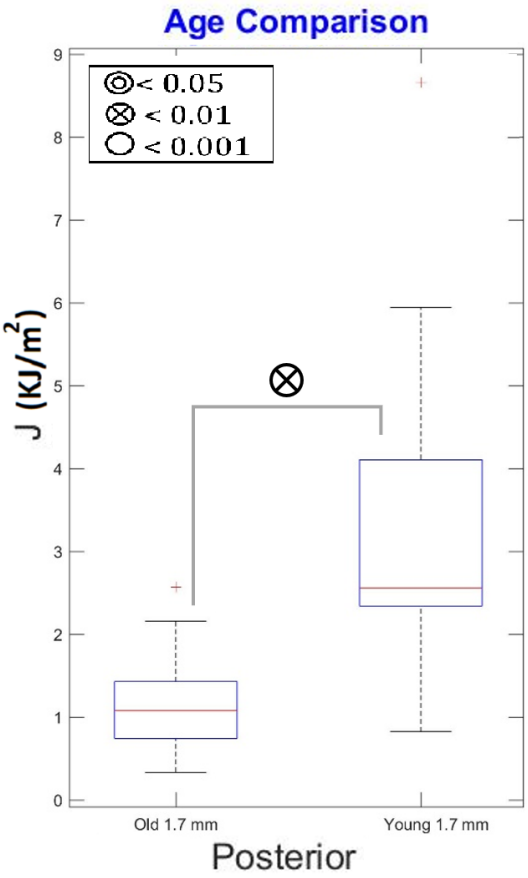

Figure B.15: Age comparison of J in the posterior of beam size 1.7 mm

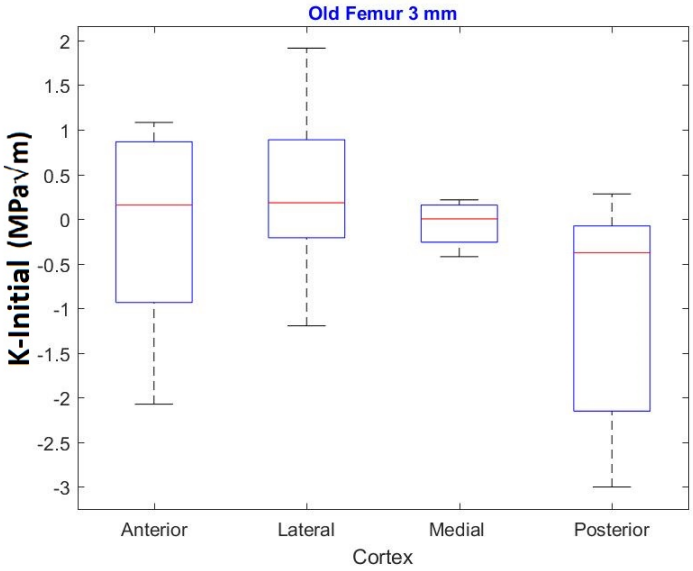

Figure B.16: Comparison of anatomical locations of K-Initial in the old equine femur for beam size 3 mm

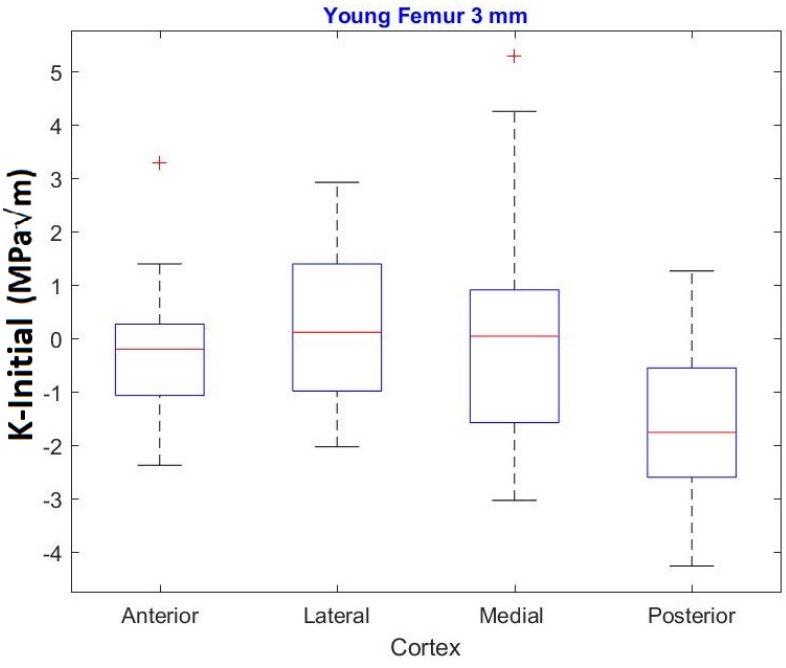

Figure B.17: Comparison of anatomical locations of K-Initial in the young equine femur for beam size 3 mm

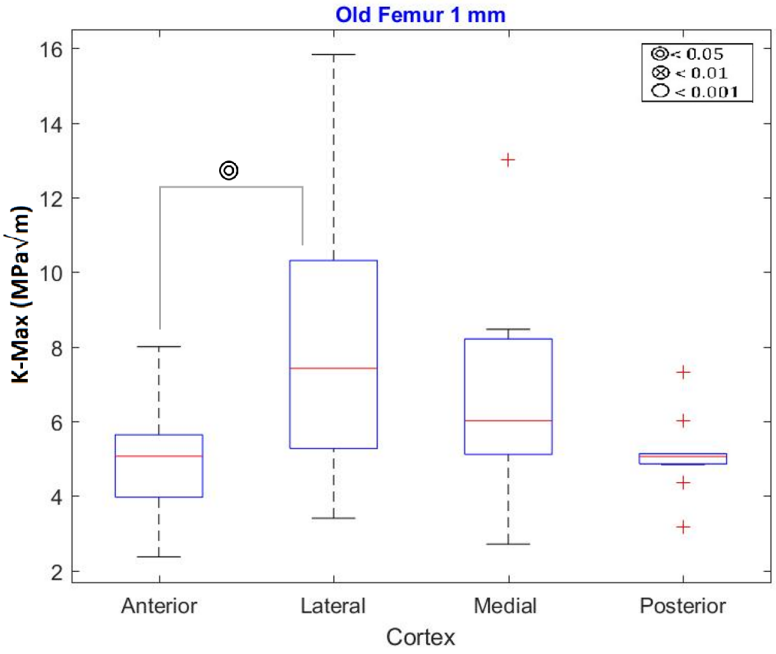

Figure B.18: Comparison of anatomical locations of K-Max in the old equine femur for beam size 1 mm

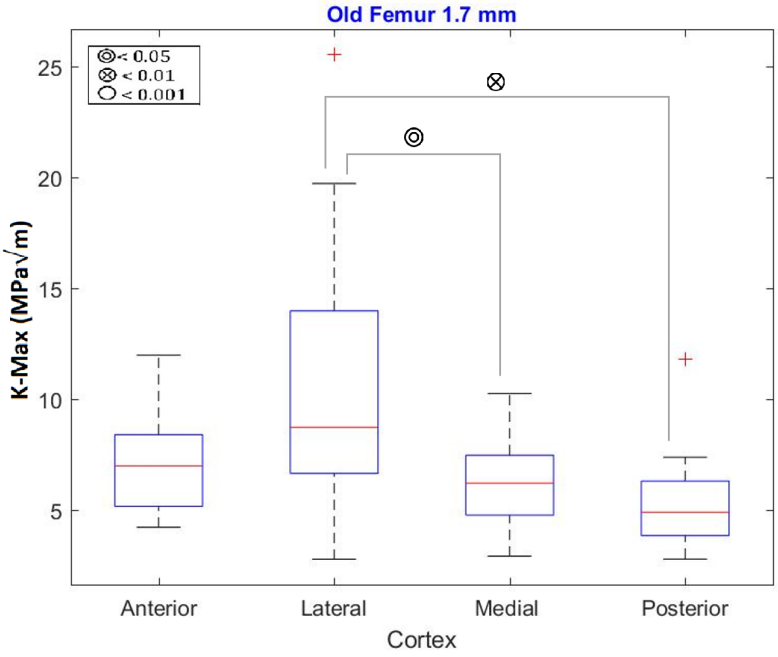

Figure B.19: Comparison of anatomical locations of K-Max in the old equine femur for beam size 1.7 mm

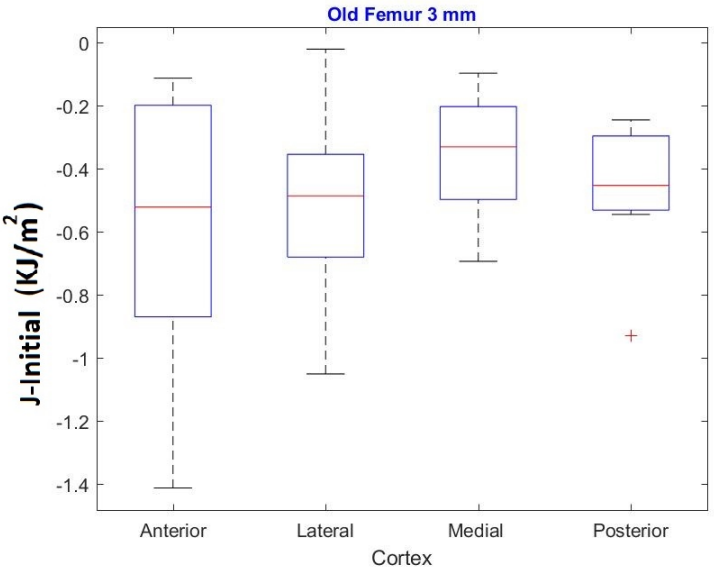

Figure B.20: Comparison of anatomical locations of J-Initial in the old equine femur for beam size 3 mm

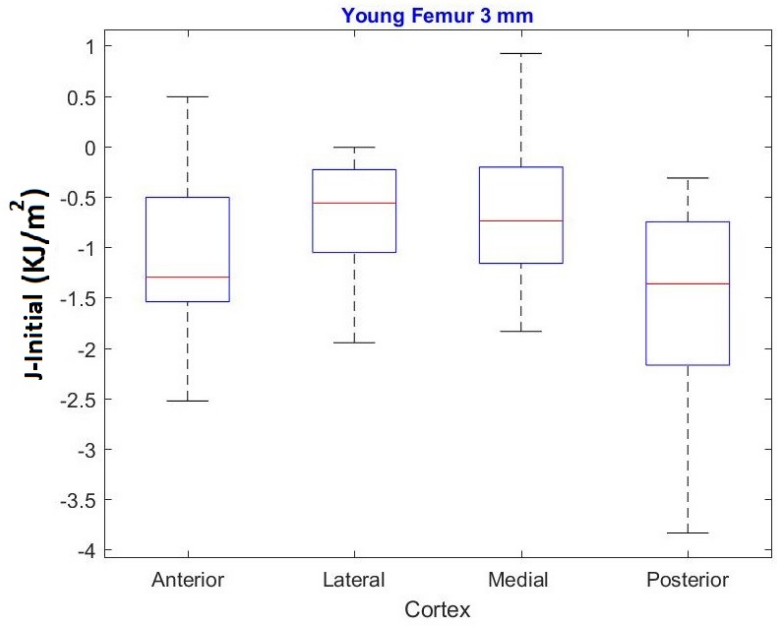

Figure B.21: Comparison of anatomical locations of J-Initial in the young equine femur for beam size 3 mm

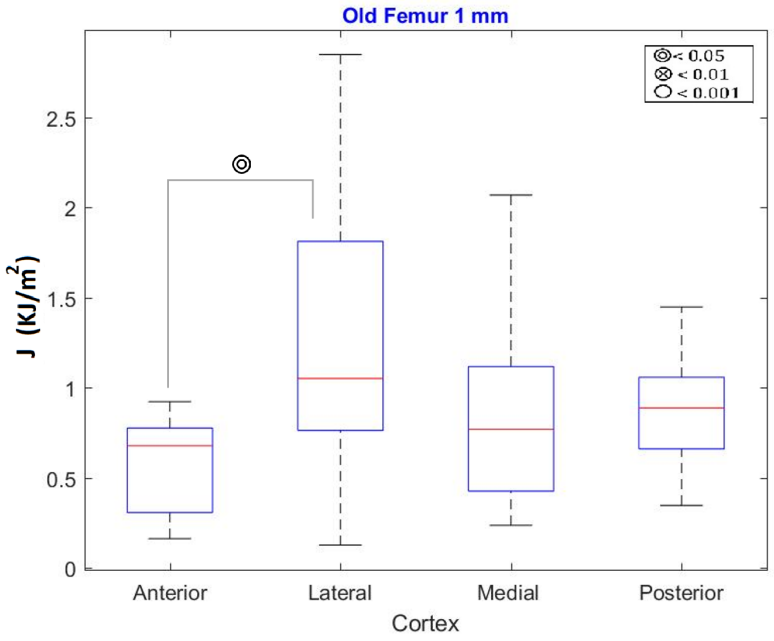

Figure B.22: Comparison of anatomical locations of J in the old equine femur for beam size 1 mm

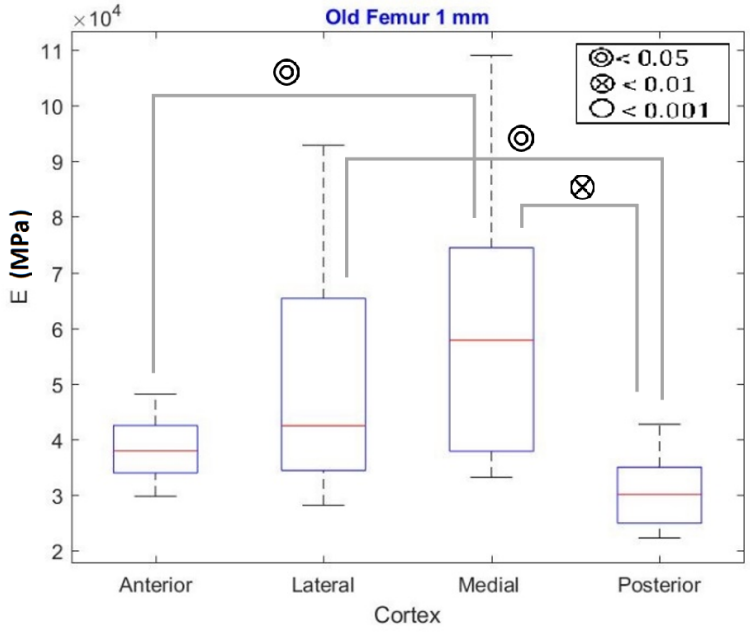

Figure B.23: Comparison of anatomical locations of E in the old equine femur for beam size 1 mm

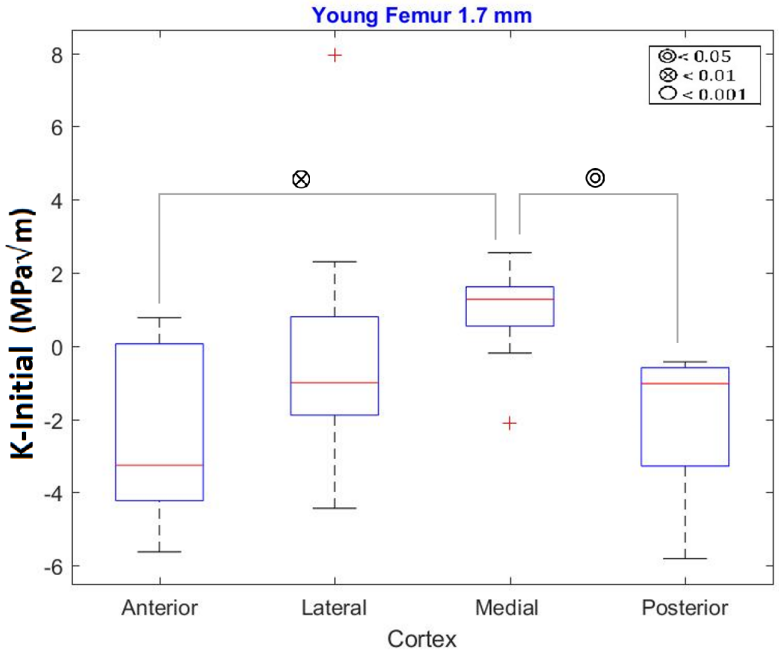

Figure B.24: Comparison of anatomical locations of K-Initial in the young equine femur for beam size 1.7 mm

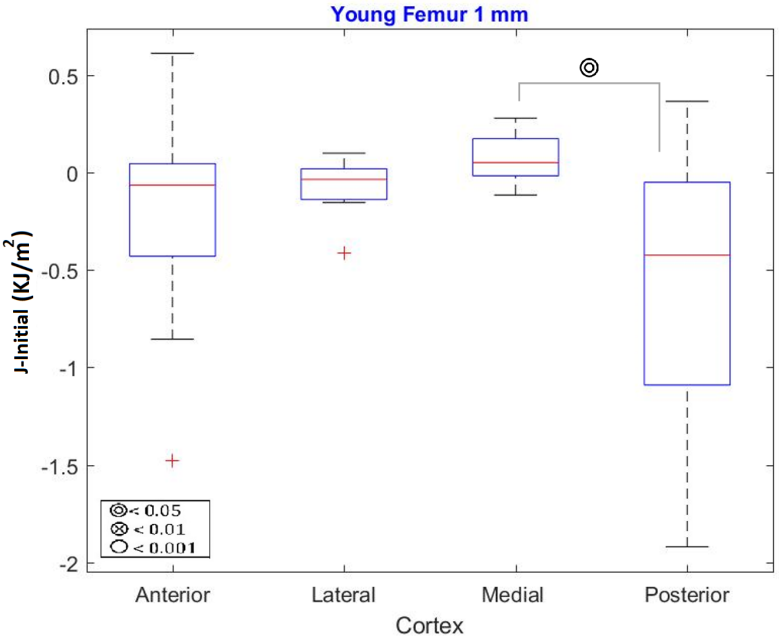

Figure B.25: Comparison of anatomical locations of J-Initial in the young equine femur for beam size 1 mm

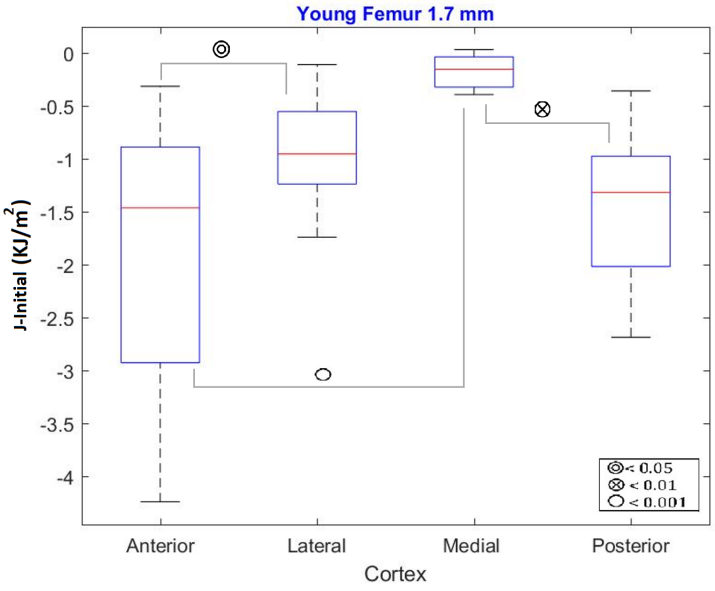

Figure B.26: Comparison of anatomical locations of J-Initial in the young equine femur for beam size 1.7 mm

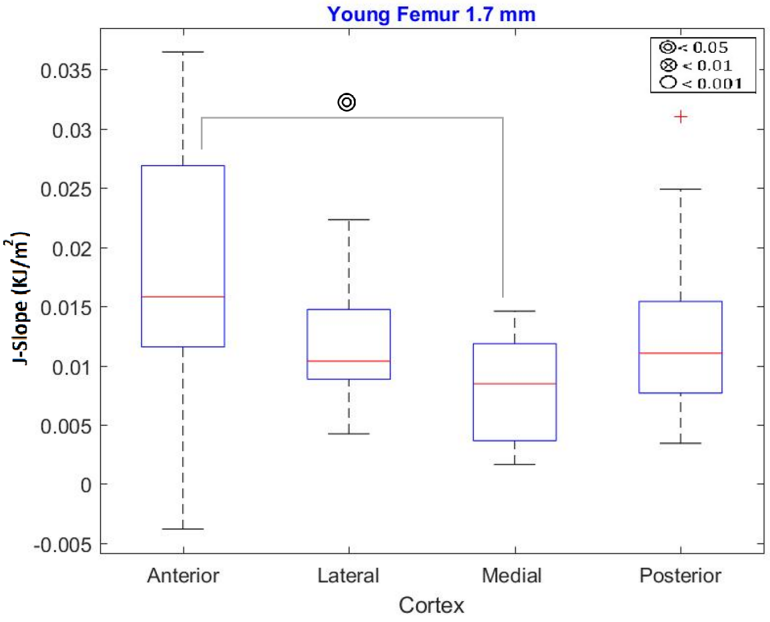

Figure B.27: Comparison of anatomical locations of J-Slope in the young equine femur for beam size 1.7 mm

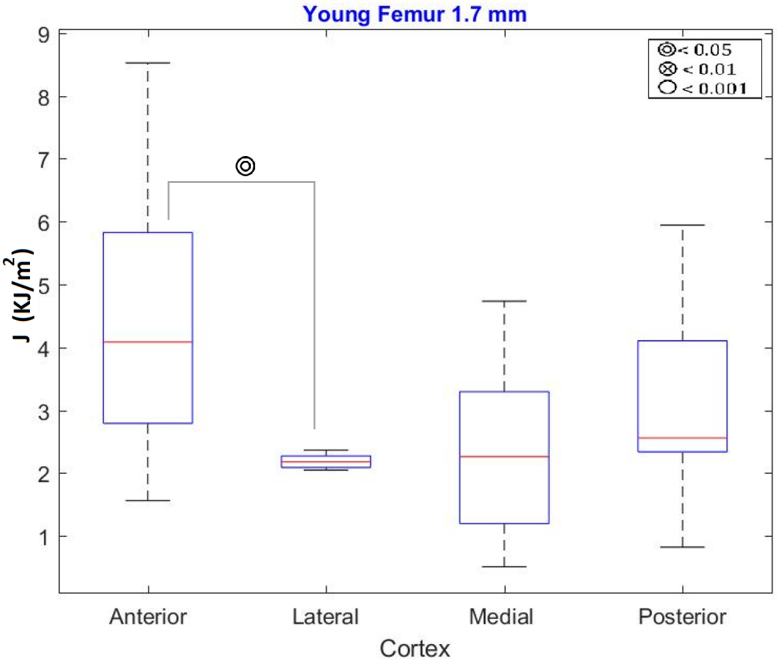

Figure B.28: Comparison of anatomical locations of J in the young equine femur for beam size 1.7 mm

Bibliography

[1] Barlett, R. "Reducing injury and improving Performance." Spon, London (1999).

[2] Cowin, Stephen C., and Stephen B. Doty. Tissue mechanics. Springer Science & Business Media, 2007.

[3] Nalla, R. K., et al. "Fracture in human cortical bone: local fracture criteria and toughening mechanisms." Journal of biomechanics 38.7 (2005): 1517-1525.

[4] Bronzino, Joseph D., and Daniel J. Schneck. Biomechanics: principles and applications. CRC press, 2002.

[5] Van Staa, T. P., et al. "Epidemiology of fractures in England and Wales." Bone 29.6 (2001): 517-522.

[6] Aspray, Terence J., et al. "Low bone mineral content is common but osteoporotic fractures are rare in elderly rural Gambian women." Journal of Bone and Mineral Research 11.7 (1996): 1019-1025.

[7] Hui, Siu L., Charles W. Slemenda, and C. Conrad Johnston. "Age and bone mass as predictors of fracture in a prospective study." The Journal of clinical investigation 81.6 (1988): 1804-1809.

[8] Heaney, Robert P. "Is the paradigm shifting?." Bone 33.4 (2003): 457-465.

[9] Vashishth, D., J. C. Behiri, and W. Bonfield. "Crack growth resistance in cortical bone: concept of microcrack toughening." Journal of biomechanics 30.8 (1997): 763-769.

[10] Zioupos, P., J. D. Currey, and A. J. Hamer. "The role of collagen in the declining mechanical properties of ageing human cortical bone." Journal of Biomedical Materials Research: An

Official Journal of The Society for Biomaterials, The Japanese Society for Biomaterials, and The Australian Society for Biomaterials 45.2 (1999): 108-116.

[11] Ritchie, Robert O., et al. How Tough is Human Cortical Bone? In-Situ Measurements on Realistically Short Cracks. No. LBNL-839E. Lawrence Berkeley National Lab.(LBNL), Berkeley, CA (United States), 2008.

[12] Grimal, Quentin, et al. "A determination of the minimum sizes of representative volume elements for the prediction of cortical bone elastic properties." Biomechanics and modeling in mechanobiology 10.6 (2011): 925-937.

[13] Yeni, Y.N., Norman, T.L., 2000. Fracture toughness of human femoral neck: effect of microstructure, composition, and age. Bone 26, 499.

[14] Nalla, R. Kinney, John H. Kinney, and Robert O. Ritchie. "Mechanistic fracture criteria for the failure of human cortical bone." Nature materials 2.3 (2003): 164.

[15] Willett, Thomas L., et al. "-Irradiation sterilized bone strengthened and toughened by ribose pre-treatment." journal of the mechanical behavior of biomedical materials 44 (2015): 147-155.

[16] Woodside, Mitchell, and Thomas L. Willett. "Elasticplastic fracture toughness and rising JR-curve behavior of cortical bone is partially protected from irradiationsterilization-induced degradation by ribose protectant." Journal of the mechanical behavior of biomedical materials 64 (2016): 53-64.

[17] Yan, Jiahau, John J. Mecholsky Jr, and Kari B. Clifton. "How tough is bone? Application of elasticplastic fracture mechanics to bone." Bone 40.2 (2007): 479-484.

[18] Zimmermann, Elizabeth Ann. The deformation and fracture of human cortical bone across multiple length-scales. Diss. UC Berkeley, 2011.

[19] Hillier, Maria L., and Lynne S. Bell. "Differentiating human bone from animal bone: a review of histological methods." Journal of forensic sciences 52.2 (2007): 249-263.

[20] Marieb, Elaine Nicpon, and Katja Hoehn. Human anatomy & physiology. Pearson Education, 2007.

[21] Chapter 6. Bone Classification and Structure, Anatomy and Physiolog, Authored by: OpenStax College. Provided by: Rice University. [ONLINE]

[22] Weiner, Stephan, and Wolfie Traub. "Bone structure: from angstroms to microns." The FASEB journal 6.3 (1992): 879-885.

[23] Landis, W. J. "The strength of a calcified tissue depends in part on the molecular structure and organization of its constituent mineral crystals in their organic matrix." Bone 16.5 (1995): 533-544.

[24] Rho, Jae-Young, Liisa Kuhn-Spearing, and Peter Zioupos. "Mechanical properties and the hierarchical structure of bone." Medical engineering & physics 20.2 (1998): 92-102.

[25] Arsenault, A. Larry. "Image analysis of collagen-associated mineral distribution in cryogenically prepared turkey leg tendons." Calcified tissue international 48.1 (1991): 56-62.

[26] McNally, Elizabeth A., et al. "A model for the ultrastructure of bone based on electron microscopy of ion-milled sections." PLOS one 7.1 (2012)

[27] Su, X., et al. "Organization of apatite crystals in human woven bone." Bone 32.2 (2003): 150-162.

[28] Ascenzi, Antonio, and Ermanno Bonucci. "The tensile properties of single osteons." The Anatomical Record 158.4 (1967): 375-386.

[29] Ascenzi, Antonio, and Ermanno Bonucci. "The compressive properties of single osteons as a problem of molecular biology." Calcified Tissue International 2 (1968): 44-44.

[30] Bromage, Timothy G., et al. "Circularly polarized light standards for investigations of collagen fiber orientation in bone." The Anatomical Record Part B: The New Anatomist: An Official Publication of the American Association of Anatomists 274.1 (2003): 157-168.

[31] Giraud-Guille, Marie-Madeleine. "Twisted plywood architecture of collagen fibrils in human compact bone osteons." Calcified tissue international 42.3 (1988): 167-180.

[32] Bullough, Peter G. Bullough and Vigorita's Slide Atlas of Orthopedic Pathology with Clinical and Radiologic Correlations. Gower Medical Pub., 1992.

[33] Skedros, John G., et al. "Cement lines of secondary osteons in human bone are not mineraldeficient: New data in a historical perspective." The Anatomical Record Part A: Discoveries in Molecular, Cellular, and Evolutionary Biology 286.1 (2005): 781-803.

[34] Cowin, Stephen C. Bone mechanics handbook. CRC press, 2001.

[35] Currey, John D. Bones: structure and mechanics. Princeton university press, 2013.

[36] Bone structure - Servier Medical Art - 3000 free medical images. [ONLINE]

[37] Martin, R. Bruce, and David B. Burr. Structure, function, and adaptation of compact bone. Raven Pr, 1989.

[38] Gong, J. K., J. S. Arnold, and S. H. Cohn. "Composition of trabecular and cortical bone." The Anatomical Record 149.3 (1964): 325-331.

[39] Kokubo, Tadashi, Hyun-Min Kim, and Masakazu Kawashita. "Novel bioactive materials with different mechanical properties." Biomaterials 24.13 (2003): 2161-2175.

[40] Socratic.org. 2018. What are the two types of bone tissue? How do they differ in structure and function? — Socratic. [ONLINE]

[41] Stevens, Alan, and James Lowe. Histologie humaine. De Boeck Suprieur, 1997.

[42] Noble, Brendon S., and Jonathan Reeve. "Osteocyte function, osteocyte death and bone fracture resistance." Molecular and cellular endocrinology 159.1-2 (2000): 7-13

[43] Jee, W. S. "Integrated bone tissue physiology: anatomy and physiology." Bone mechanics handbook (2001)

[44] Carter, Dennis R., and Dan M. Spengler. "Mechanical properties and composition of cortical bone." Clinical Orthopaedics and Related Research 135 (1978): 192-217.

[45] Lanyon, L. E. "Osteocytes, strain detection, bone modeling and remodeling." Calcified tissue international 53.1 (1993): S102-S107.

[46] Introduction to Bone Biology: All About our Bones — International Osteoporosis Foundation. [ONLINE]

[47] Seeman, Ego. "Bone modeling and remodeling." Critical Reviews in Eukaryotic Gene Expression 19.3 (2009)

[48] Robling, Alexander G., and Charles H. Turner. "Mechanical signaling for bone modeling and remodeling." Critical reviews in eukaryotic gene expression 19.4 (2009): 319.

[49] Feng, Xu, and Jay M. McDonald. "Disorders of bone remodeling." Annual Review of Pathology: Mechanisms of Disease 6 (2011): 121-145.

[50] Encyclopedia Britannica. 2018. Bone remodeling — physiology — Britannica.com. [ONLINE]

[51] Weiner, Steve, and H. Daniel Wagner. "The material bone: structure-mechanical function relations." Annual Review of Materials Science 28.1 (1998): 271-298.

[52] Gilmore, R. S., and J. L. Katz. "Elastic properties of apatites." Journal of Materials Science 17.4 (1982): 1131-1141.

[53] Olszta, Matthew J., et al. "Bone structure and formation: a new perspective." Materials Science and Engineering: R: Reports 58.3-5 (2007): 77-116.

[54] Morgan, Stacyann, Atharva A. Poundarik, and Deepak Vashishth. "Do non-collagenous proteins affect skeletal mechanical properties?." Calcified tissue international 97.3 (2015): 281-291.

[55] Hamed, Elham, Yikhan Lee, and Iwona Jasiuk. "Multiscale modeling of elastic properties of cortical bone." Acta mechanica 213.1-2 (2010): 131-154.

[56] Yamashita, Junro, et al. "Collagen and bone viscoelasticity: a dynamic mechanical analysis." Journal of Biomedical Materials Research: An Official Journal of The Society for Biomaterials, The Japanese Society for Biomaterials, and The Australian Society for Biomaterials and the Korean Society for Biomaterials 63.1 (2002): 31-36.

[57] Wolff, Julius. "Das gesetz der transformation der knochen." A Hirshwald 1 (1892): 1-152

[58] Holtrop, MARIJKE E. "The ultrastructure of bone." Annals of Clinical & Laboratory Science 5.4 (1975): 264-271.

[59] Turner, Charles H., and David B. Burr. "Basic biomechanical measurements of bone: a tutorial." Bone 14.4 (1993): 595-608.

[60] Frankel, Victor Hirsch, and Margareta Nordin. Basic biomechanics of the skeletal system. Lea & Febiger, 1980.

[61] Bankoff, Antonia Dalla Pria. "Biomechanical characteristics of the bone." Human Musculoskeletal Biomechanics. InTech, 2012.

[62] Hench, Larry L., and June Wilson. "Introduction." An introduction to bioceramics. 1993. 1-24.

[63] Hernandez, C. J., and T. M. Keaveny. "A biomechanical perspective on bone quality." Bone 39.6 (2006): 1173-1181.

[64] Ritchie, Robert O. "The conflicts between strength and toughness." Nature materials 10.11 (2011): 817.

[65] Ritchie, Robert O., Markus J. Buehler, and Paul Hansma. "Plasticity and toughness in bone." (2009).

[66] Launey, Maximilien E., Markus J. Buehler, and Robert O. Ritchie. "On the mechanistic origins of toughness in bone." Annual review of materials research 40 (2010): 25-53.

[67] Sabet, Fereshteh A., et al. "Modelling of bone fracture and strength at different length scales: a review." Interface focus 6.1 (2016).

[68] Ritchie, Robert O., et al. "A fracture mechanics and mechanistic approach to the failure of cortical bone." Fatigue & Fracture of Engineering Materials & Structures 28.4 (2005): 345-371.

[69] C.E. Inglis, Stresses in a plate due to the presence of cracks and sharp corners, Trans. Inst. Nav. Archit. London 55, (1913).

[70] A.A. Griffith, Phenomena of rupture and flow in solids, Philos. Trans. R. Soc. London Ser. A221, (1920), pp. 163198.

[71] Irwin, George R. "Analysis of stresses and strains near the end of a crack traversing a plate." J. appl. Mech. (1957).

[72] Knott, John Frederick. Fundamentals of fracture mechanics. Gruppo Italiano Frattura, (1973).

[73] Koester, Kurt J., J. W. Ager Iii, and R. O. Ritchie. "The true toughness of human cortical bone measured with realistically short cracks." Nature materials 7.8 (2008): 672.

[74] Peterlik, Herwig, et al. "From brittle to ductile fracture of bone." Nature materials 5.1 (2006): 52.

[75] Ritchie RO. Mechanisms of fatigue-crack propagation in ductile and brittle solids. Int J Fract 1999;100(1):55-83.

[76] Katsamenis, Orestis L., Thomas Jenkins, and Philipp J. Thurner. "Toughness and damage susceptibility in human cortical bone is proportional to mechanical inhomogeneity at the osteonal-level." Bone 76 (2015): 158-168.

[77] Nalla, Ravi K., Jamie J. Kruzic, and Robert O. Ritchie. "On the origin of the toughness of mineralized tissue: microcracking or crack bridging?." Bone 34.5 (2004): 790-798.

[78] Zimmermann, Elizabeth A., Bjrn Busse, and Robert O. Ritchie. "The fracture mechanics of human bone: influence of disease and treatment." BoneKEy reports 4 (2015).

[79] OBrien, Fergal J., David Taylor, and T. Clive Lee. "The effect of bone microstructure on the initiation and growth of microcracks." Journal of Orthopaedic Research 23.2 (2005): 475-480.

[80] Pal, Subrata. "Mechanical properties of biological materials." Design of Artificial Human Joints & Organs. Springer, Boston, MA, 2014. 23-40.

[81] X. Wang, X. Shen, X. Li, and C. M. Agrawal, Age-related changes in the collagen network and toughness of bone. Bone 2002;31(1):17.

[82] Kulin, Robb M., Fengchun Jiang, and Kenneth S. Vecchio. "Aging and loading rate effects on the mechanical behavior of equine bone." Jom 60.6 (2008): 39-44.

[83] Melvin, J. W., and F. G. Evans. "ASME biomaterials symposium." Detroit, MI (1973).

[84] ASTM Committee E08 on Fatigue and Fracture. Standard test method for measurement of fracture toughness. ASTM International, 2011.

[85] Begley, J. A., and J. D. Landes. "The J integral as a fracture criterion." Fracture Toughness: Part II. ASTM International, (1972).

[86] Rice, J., P. Paris, and J. Merkle. "Some further results of J-integral analysis and estimates." Progress in flaw growth and fracture toughness testing. ASTM International, (1973).

[87] Sumpter, J. D. G., and C. E. Turner. "Method for laboratory determination of J c." Cracks and fracture. ASTM International, (1976).

[88] Egermann, Marcus, Jrg Goldhahn, and E. Schneider. "Animal models for fracture treatment in osteoporosis." Osteoporosis international 16.2 (2005): S129-S138.

[89] Liebschner, Michael AK. "Biomechanical considerations of animal models used in tissue engineering of bone." Biomaterials 25.9 (2004): 1697-1714.

[90] Schimandle, Jeffrey H., and Scott D. Boden. "Spine update. The use of animal models to study spinal fusion." Spine 19.17 (1994): 1998-2006.

[91] Olsen, Stanley John. An osteology of some Maya mammals. Vol. 73. Peabody Museum of Archaeology &, (1982).

[92] Arizona State Museum. 2016. About — News & Features Archive — Distinguishing Human From Animal Bone, by James Watson and John McClelland — Arizona State Museum. [ONLINE]

[93] Crowder, Christian, and Sam Stout, eds. Bone histology: an anthropological perspective. CRC Press, (2011).

[94] Foote, James Stephen. A contribution to the comparative histology of the femur. Vol. 35. No. 3. Smithsonian institution, 1916.

[95] Harsnyi, Laszlo. "Differential diagnosis of human and animal bone." Histology of ancient human bone: methods and diagnosis. Springer, Berlin, Heidelberg, 1993. 79-94.

[96] Mulhern, Dawn M., and Douglas H. Ubelaker. "Differences in osteon banding between human and nonhuman bone." Journal of Forensic Science 46.2 (2001): 220-222.

[97] Whitman, Elizabeth J. "Differentiating between human and non-human secondary osteons in human, canine, and bovine rib tissue." (2002): 1113-1113

[98] Enlow, Donald H. "A comparative histological study of fossil and recent bone tissues, part III." Texas J. Sci. 10 (1958): 187-230.

[99] Zedda, Marco, et al. "Comparative bone histology of adult horses (Equus caballus) and cows (Bos taurus)." Anatomia, histologia, embryologia 37.6 (2008): 442-445.

[100] Stover, SUSAN M., et al. "Histological features of the dorsal cortex of the third metacarpal bone mid-diaphysis during postnatal growth in thoroughbred horses." Journal of anatomy 181.Pt 3 (1992): 455.

[101] Mori, Ryoichi, et al. "Comparative histology of the laminar bone between young calves and foals." Cells Tissues Organs 175.1 (2003): 43-50.

[102] Rajtova, V. "Lamellar bone structure in small ruminants." Folia Vet. 39 (1995): 59-64.

[103] Currey, J. D. "The many adaptations of bone." Journal of biomechanics 36.10 (2003): 1487-1495.

[104] De Kleer, V. "Development of bone." Bone in Clinical Orthopaedics,(Sumner-Smith G, ed) WB Saunders Co, Philadelphia, PA (2006): 1-80.

[105] Eitel, F., et al. "Bone regeneration in animals and in man." Archives of orthopaedic and traumatic surgery 99.1 (1981): 59-64.

[106] URBANOV, PETRA, and VLADIMR NOVOTN. "Distinguishing between human and non-human bones: histometric method for forensic anthropology." Anthropologie (1962-) 43.1 (2005): 77-86.

[107] Martiniakov, Monika, et al. "Differences among species in compact bone tissue microstructure of mammalian skeleton: use of a discriminant function analysis for species identification." Journal of forensic sciences 51.6 (2006): 1235-1239.

[108] Erickson, Gregory M., Joseph Catanese III, and Tony M. Keaveny. "Evolution of the biomechanical material properties of the femur." The Anatomical Record: An Official Publication of the American Association of Anatomists 268.2 (2002): 115-124.

[109] Analysis of bone by micro-CT General information (2013).

[110] Parfitt, A. Michael, et al. "Bone histomorphometry: standardization of nomenclature, symbols, and units: report of the ASBMR Histomorphometry Nomenclature Committee." Journal of bone and mineral research 2.6 (1987): 595-610.

[111] Recker, Robert R. "Bone histomorphometry." Techniques and interpretation (1983).

[112] Abdel-Wahab, Adel, Norhaziqah Nordin, and Vadim Silberschmidt. "Variability and anisotropy of fracture toughness of cortical bone tissue." Journal of Physics: Conference Series. Vol. 382. No. 1. IOP Publishing, (2012).

[113] Katsamenis, O.L., Jenkins, T., Quinci, F., Michopoulou, S., Sinclair, I., Thurner, P.J., (2013). A Novel Videography Method for Generating Crack-Extension Resistance Curves in Small Bone Samples. PLoS One 8, 113.

[114] Doube M, Kosowski MM, Arganda-Carreras I, Cordelires F, Dougherty RP, Jackson J, Schmid B, Hutchinson JR, Shefelbine SJ. (2010) BoneJ: free and extensible bone image analysis in ImageJ. Bone 47:1076-9. doi: 10.1016/j.bone.2010.08.023

[115] Yeni, Yener N., et al. "The relationships between femoral cortex geometry and tissue mechanical properties." journal of the mechanical behavior of biomedical materials 21 (2013): 9-16.

[116] Augat, Peter, and Sandra Schorlemmer. "The role of cortical bone and its microstructure in bone strength." Age and ageing 35(2006).

[117] Brown, Christopher U., Yener N. Yeni, and Timothy L. Norman. "Fracture toughness is dependent on bone locationa study of the femoral neck, femoral shaft, and the tibial shaft." Journal of Biomedical Materials Research: An Official Journal of The Society for Biomaterials and The Japanese Society for Biomaterials 49.3 (2000): 380-389.

List of Figures

List of Tables